The Hong Kong Polytechnic University

Department of Applied Physics

Ferromagnetic Metal-Polymer Nanocomposites for Magnetic Sensing Applications

KWONG Ho Yin, Anthony

A thesis submitted in partial fulfillment of the requirements for the

Degree of Master of Philosophy

August 2007

CERTIFICATE OF ORIGINALITY

I hereby declare that this thesis is my own work and that, to the best of my knowledge and belief, it reproduces no material previously published or written nor material which has been accepted for the award of any other degree or diploma, except where due acknowledgement has been made in the text.

________________________________(Signed)

____KWONG Ho Yin, Anthony______(Name of student)

Abstract

In this project, cobalt and polytetrafluoroethylene (PTFE) composite films were fabricated by Pulsed Laser Deposition technique (PLD) with the use of split target. The composition of the films was changed by varying the pulse irradiation ratio of the metal and polymer targets. The deposited samples consist of cobalt particles of sizes about 5 nm and irregular shaped PTFE particles of size larger than 200 nm in a well connected PTFE polymer matrix. The cobalt-PTFE composite films exhibit a room temperature magnetoresistance (MR) change of about 5% at 10 kOe. A significant enhancement of MR value to 6% was achieved at 20 K at 8 kOe. The blocking temperature of the sample was obtained to be about 90 K. Possible explanations of the observed experimental results are suggested. Cost-effective and simple magnetic sensor applicable in device industries prepared by this method is anticipated. Fabrication of cobalt nanoparticles has been successfully demonstrated by PLAL technique in 3 kinds of solvent with detailed discussions. Superhydrophobic PTFE thin films for fabricating self-cleaning surfaces were successfully fabricated by PLD technique. A large contact angle of about 170° and low sliding angle was achieved. Detailed discussions and explanations were presented. Fabrication of cobalt hydroxide nanoplatelets at room temperature by an innovative method, simply using sodium hydroxide (NaOH) solution to react with a PLD prepared pure cobalt thin film, was presented. The morphology of the nanoplatelets and the crystal structure were characterized. This method provides a simple, relatively fast and clean method to produce nano-sized cobalt hydroxide for using in real applications.

List of Publications

H. Y. Kwong, M. H. Wong, Y. W. Wong, and K. H. Wong
"Magnetoresistivity of cobalt-polytetrafluoroethylene granular composites"
Applied Physics Letters, **89** (2006) 173109

H. Y. Kwong, M. H. Wong, Y. W. Wong, and K. H. Wong
"Superhydrophobicity of polytetrafluoroethylene thin film fabricated by pulsed laser deposition"
Applied Surface Science, **253** (2007) 8841-8845

H. Y. Kwong, M. H. Wong, Y. W. Wong, and K. H. Wong
"Magnetoresistivity of cobalt-PTFE granular composite film produced by pulsed laser deposition technique"
Reviews on Advanced Materials Science, **15** (2007) 215-219

H. Y. Kwong, Y. W. Wong, and K. H. Wong
"Temperature Dependence of Magnetoresistivity of Cobalt-Polytetrafluoroethylene Granular Composite Films"
Journal of Applied Physics, **102** (2007) 114303

ACKNOWLEDGEMENTS

I would like to offer my heartfelt thanks to Dr. Y. W. Wong, for his close supervision, suggestions, and unlimited support throughout the study period. I would also like to acknowledge Dr. K. H. Wong and Prof. F. G. Shin for their fruitful suggestions and discussions. Special thanks are given to M. H. Wong, W. F. Cheng, W. L. Sin, Y. M. Tang, C. H. Lau, C. Y. Lam, K. S. Wong, S. W. Cheung, W. C. Liu, Y. K. Chan and M. Y. Pang, for giving me a hand when I ever needed support throughout the research period, and providing me a lot of warm, unforgettable and fruitful memories. I would like to acknowledge Ms Y. Yeung, C. S. Lo, M. N. Yeung and T. L. Chan for their helpful technical supports.

Finally, special thanks are given to my loved and beloved one, Kitty, for her understanding, tolerating and never-ending support during the harsh period.

The financial support of the project from the Hong Kong Research Grants Council (A/C: PolyU 5293/05E) is gratefully acknowledged.

TABLE OF CONTENTS

ABSTRACT i

LIST OF PUBLICATIONS ii

ACKNOWLEDGEMENTS iii

TABLE OF CONTENTS iv

LIST OF FIGURES ix

LIST OF TABLES xiii

CHAPTER 1 1

Introduction

1.1 Background 1

1.2 Literature Review

1.2.1 Pulsed Laser Deposition (PLD) **5**

1.2.2 PLD of Polymer **8**

1.2.3 Giant Magnetoresistance (GMR) **11**

1.2.4 Tunneling Magnetoresistance (TMR) **12**

1.2.5 TMR in Granular Film **18**

1.2.6 Pulsed Laser Ablation in Liquid (PLAL) **23**

1.3 Outline of thesis 25

CHAPTER 2 **28**

Sample Preparations and Characterizations

2.1 Cobalt-Polytetrafluoroethylene Granular Composite Film on Glass Substrate 28

2.2 Cobalt Nanoparticles Fabricated by Laser Ablation in Liquid 34

2.3 Superhydrophobic Polytetrafluoroethylene Thin Film Fabricated by Pulsed Laser Deposition 37

2.4 Preparation of nano-sized cobalt hydroxide by laser deposition process 39

CHAPTER 3 **42**

Cobalt-Polytetrafluoroethylene Granular Composite Film on Glass Substrate

3.1 Introduction 42

3.2 Infrared Spectroscopy 45

3.3 Microstructure of the composite films 48

3.4 Microstructure Characterization by TEM 54

3.5 Temperature Dependence of Resistance of Co-PTFE Composite Films 55

3.6 Magnetic Properties of Co-PTFE Composite Films 58

3.7 Room Temperature Magnetoresistance of Co-PTFE Composite Films 68

3.8 Temperature Dependence of Magnetoresistance of Co-PTFE Composite Films 75

3.9 Reproducibility of Resistance and Magnetoresistance 88

CHAPTER 4 89

Cobalt Nanoparticles produced by Laser Ablation of Cobalt Target in Liquid

4.1 Introduction 89

4.2 Laser ablation in Hexane 91

4.2.1 SEM Analysis **91**

4.2.2 TEM Analysis **93**

4.3 Laser ablation in Ethanol 95

4.4 Laser ablation in Toluene 98

4.4.1 SEM Analysis **98**

4.4.2 TEM Analysis **100**

CHAPTER 5 103

Superhydrophobicity of Polytetrafluoroethylene Thin Film Fabricated by Pulsed Laser Deposition

5.1 Introduction 103
5.2 Infrared Spectroscopy 110
5.3 Surface Morphology 112
5.4 Contact Angle Measurement 117

CHAPTER 6 123

Fabrication of nano-sized cobalt hydroxide through laser deposition process

6.1 Introduction 123
6.2 Surface Morphology 126
6.3 XRD analysis 134
6.4 Infrared Spectroscopy 136

CHAPTER 7 **140**

Conclusions

REFERENCES **143**

List of Figures

Figure 1.1: **Schematic diagram showing the basic elements of a PLD deposition system.** 7

Figure 1.2: **Density of states diagram describing spin-dependent tunneling (SDT) in MTJ. Magnetization orientations of the ferromagnetic layers (FM) are (a) parallel (b) antiparallel.** 13

Figure 1.3: **(a) Schematic diagram of granular structure and a higher-order tunneling process where a charge carrier is transferred from the charged large granule, through the two small ones, to the neutral large one; (b) Model structure used for the calculation of conductivity [Mitani (1998)].** 21

Figure 1.4: **Schematic diagram of the formation of nanoparticles in the solid-liquid interface during PLAL. (a) The generation of the laser-induced plasma due to the laser irradiation on the target. (b) The expansion of the plasma plume in liquid due to the absorbing the later laser pulse and the plasma-induced pressure created by the shock wave. (c) Formation of nanoparticles and surface coating on target surface due to the condensation of the plasma plume in liquid.** 24

Figure 2.1: **Splitting target holder for PLD.** 30

Figure 2.2: **Schematic diagram of the (a) top-view and (b) cross-section of a cobalt-PTFE composite film on glass substrate with gold electrodes.** 31

Figure 2.3: **Schematic diagram of the setup used in the process of pulsed laser ablation in liquid (PLAL).** 35

Figure 3.1 **FTIR spectra of (a) bulk PTFE and (b) PTFE film produced by PLD (IR-PLD samples).** 45

Figure 3.2 **FTIR spectra of Co-PTFE composite film (IR-PLD samples).** 46

Figure 3.3 **FTIR spectra of Co-PTFE composite film (UV-PLD samples).** 47

Figure 3.4 **SEM image of Co-PTFE composite film (IR-PLD samples).** 49

Figure 3.5 **A higher magnification image of Co-PTFE composite film (IR-PLD samples).** 49

Figure 3.6 **SEM image of Co-PTFE composite film (UV-PLD samples).** 50

Figure 3.7 **A higher magnification image of Co-PTFE composite film (UV-PLD samples).** 50

Figure 3.8 **SEM image of Co-PTFE composite film after etching with 0.1M HCl (IR-PLD samples).** 52

Figure 3.9 **SEM image of Co-PTFE composite film at the etched boundary (IR-PLD samples).** 52

Figure 3.10 **SEM image of Co-PTFE composite film after etching with 0.1M HCl (UV-PLD samples).** 53

Figure 3.11 **SEM image of Co-PTFE composite film at the etched boundary (UV-PLD samples).** 53

Figure 3.12 **(a) TEM image of Co-PTFE composite film deposited on carbon-coated copper grid for 7 min (UV-PLD samples) (b) High Resolution TEM image.** 54

Figure 3.13 **Temperature dependence of the resistance of Cobalt-PTFE composite film. The inset is a plot of ln$R$ against $T^{-1/2}$ (IR-PLD samples).** 56

Figure 3.14 **Temperature dependence of the resistance of Cobalt-PTFE composite film. The inset is a plot of ln$R$ against $T^{-1/2}$ (UV-PLD sample A).** 57

Figure 3.15 **Magnetization curves of Cobalt-PTFE composite film (IR-PLD samples) measured at (a) 300K and (b) 10K** 59

Figure 3.16 **Magnetization curves of Cobalt-PTFE composite film (UV-PLD sample A) measured at (a) 300K and (b) 20K, both with in-plane measurement.** 61

Figure 3.17 **Magnetization curve of Cobalt-PTFE composite film (UV-PLD sample A) with Langevin fitting at 300K, with in-plane measurement.** 63

Figure 3.18 **(a) FC and (b) ZFC magnetization as a function of temperature of Cobalt-PTFE composite film (UV-PLD sample A), with in-plane measurement.** 67

Figure 3.19 **Magnetic field dependence of the magnetoresistance of the Cobalt-PTFE composite film (IR-PLD samples), with out-of-plane measurement.** 69

Figure 3.20 **Magnetic field dependence of the magnetoresistance of the Cobalt-PTFE composite film (IR-PLD samples) with (a) out-of-plane measurement and (b) in-plane measurement.** 71

Figure 3.21 **Magnetic field dependence of the magnetoresistance of the Cobalt-PTFE composite film (UV-PLD sample A) with (a) out-of-plane measurement and (b) in-plane measurement.** 71

Figure 3.22 **Magnetic field dependence of the magnetoresistance of the Cobalt-PTFE composite film (UV-PLD sample A) with in-plane measurement. The solid line is the fit to equation: $P^2m^2/(1 + P^2m^2)$.** 74

Figure 3.23 **Magnetic field dependence of the magnetoresistance of the Cobalt-PTFE composite film (IR-PLD samples) measured at (a) 300 K and (b) 30 K, both are with in-plane measurement.** 76

Figure 3.24 **Magnetic field dependence of the magnetoresistance of the Cobalt-PTFE composite film (UV-PLD sample A) measured at (a) 300 K and (b) 20 K,**
both are with in-plane measurement. 79

Figure 3.25 **Temperature dependence of the separations of the MR peaks at a temperature range from 20 K to 300 K (UV-PLD sample A).** 81

Figure 3.26 **Temperature dependence of MR of two Cobalt-PTFE composite films (UV-PLD samples) fabricated by different laser pulse ratio of cobalt and PTFE, measured at the applied magnetic field of 8 kOe, with in-plane measurement.** 82

Figure 3.27 **Temperature dependence of MR of Cobalt-PTFE composite films (UV-PLD sample A) measured at the applied magnetic field of 8 kOe, with in-plane measurement. Dashed line represents the theoretical MR value given by the equation as shown, with P = 0.216. Solid line represents the calculated MR value in considering the temperature dependence of P, as shown in the inset.** 84

Figure 3.28 **Temperature dependence of MR of Cobalt-PTFE composite films (UV-PLD sample A) measured at the applied magnetic field of 8 kOe, with in-plane measurement. Solid line represents the calculated MR value using the higher-order tunneling model in considering the temperature dependence of P, as shown in the inset.** 87

Figure 4.1: **(a) SEM images of cobalt nanoparticles prepared in hexane; (b) and (c) SEM images of cobalt nanoparticles same as (a) but displayed on carbon coated copper grid.** 92

Figure 4.2: **(a) and (b) TEM images of a drop of cobalt nanoparticles in hexane on carbon coated copper grid; (c) SAED of images (b).** 94

Figure 4.3: **(a) SEM images of a drop of cobalt nanoparticles in ethanol on silicon wafer (black particles can be seen by naked eyes in the droplet); (b) Higher magnification images of (a).** 97

Figure 4.4: **(a) and (b) Two different morphologies of the cobalt nanoparticle displayed on silicon wafer for SEM inspection. (c) After ultrasound dispersion, the agglomeration is less serious.** 99

Figure 4.5: **(a) and (b) TEM images of a drop of cobalt nanoparticles in toluene on carbon coated copper grid; (c) SAED of images (b).** 102

Figure 5.1: **Schematic diagram of a droplet of liquid in contact with a solid surface (a) smooth surface with contact angle θ_0 and (b) rough surface with contact angle θ.** 107

Figure 5.2: **Schematic diagram of a composite solid-liquid-air interface for a rough surface.** 108

Figure 5.3: **Schematic diagram of (a) a liquid droplet in contact with a rough surface, with advancing (θ_{adv}) and receding contact angle (θ_{rec}); (b) a liquid droplet sliding down on a tilted surface, with a sliding angle α.** 109

Figure 5.4: **FTIR spectra of PTFE film deposited by PLD.** 111

Figure 5.5: **SEM images of the PLD deposited PTFE film fabricated with (a) 200, (b) 500 and (c) 1800 number of pulses. The contact angles on the corresponding surface are (a) 103°, (b) 144° and (c) 168° respectively.** 113

Figure 5.6: **AFM images of the PLD deposited PTFE film fabricated with (a) 200, (b) 500 and (c) 1800 number of pulses. The corresponding surface roughness (rms) are (a) 33.6 nm, (b) 40.4 nm (c) 77.6 nm respectively.** 115

Figure 5.7: **Number of pulses dependence of roughness (rms) of the PLD deposited PTFE film.** 116

Figure 5.8: **Roughness (rms) dependence of contact angle of the PLD deposited PTFE films. Water droplet with volume of 5 μL was used in the measurement.** 117

Figure 5.9: **Images of 5 μL water droplets on the PLD deposited PTFE films fabricated with (a) 200, (b) 500 and (c) 1800 number of pulses. The corresponding contact angles are (a) 103°, (b) 144° and (c) 168° respectively.** 119

Figure 5.10: **Water droplet volume dependence of contact angle of the PLD deposited PTFE films.** 120

Figure 6.1: **SEM images of the Co-PTFE composite film fabricated with Co:PTFE laser pulse ratio of 22:4 (a) without any treatment; (b) reacted with NaOH (0.5M) for 90 min.** 127

Figure 6.2: **SEM images of the Co-PTFE composite film fabricated with Co:PTFE laser pulse ratio of 14:2 (a) without any treatment; (b) reacted with NaOH (0.5M) for 90 min.** 128

Figure 6.3: **SEM images of the PLD deposited PTFE film (a) without any treatment; (b) reacted with NaOH (0.5M) for 90 min.** 129

Figure 6.4: **SEM images of the PLD deposited Co film (a) without any treatment; (b) and (c) reacted with NaOH (0.5M) for 90 min. Images (a) and (b) was tilted 30˚ from horizontal. Image (c) is the top view of the sample surface.** 131

Figure 6.5: **(a) – (d) SEM images of the PLD deposited Co film reacted with NaOH (0.5M) for 90 min. (e) Higher magnification of (d). (f) Schematic diagram (top view) of a substrate surface with the reacted Co film, representing the locations for the observation of (a) – (d). The color is for easy differentiation only.** 133

Figure 6.6: **XRD profiles of (a) PLD deposited Co film and (b) PLD deposited Co film reacted with NaOH (0.5M) for 90 min.** 135

Figure 6.7: **FTIR spectra of PLD deposited Co film reacted with NaOH (0.5M) for 90 min.** 137

Figure 6.8: **Schematic diagram of a PLD-deposited Co film.** 138

Figure 6.9: **SEM images of micron-sized Co particles (a) without any treatment; (b) reacted with NaOH (0.5M) for 90 min.** 139

List of Tables

Table 1.1: **Measured spin polarization values for various magnetic materials.** 16

Table 2.1: **Some important parameters in PLD process for fabrication of cobalt-PTFE composite films and dimensions of the deposited films.** 31

Table 2.2: **Some important parameters in PLD process for fabrication of superhydrophobic PTFE films.** 37

Table 2.3: **Some important parameters in PLD process for fabrication of cobalt thin films.** 39

Table 3.1 **Resistance and Magnetoresistance of 4 different Cobalt-PTFE composite films (UV-PLD sample) prepared at same experimental conditions.** 88

Table 4.1: **d-spacings of cobalt of HCP structure and its corresponding miller index.** 94

Table 4.2: **d-spacings of cobalt of HCP structure and its corresponding miller index.** 102

CHAPTER 1

Introduction

1.1 Background

Over the years of the rapid growth of nanotechnology, nano-sized and nano-structured materials have been found numerous applications owing to their fascinating properties. Especially, nanotechnology leads to the development of spintronics, which utilizes the spin of the electron rather than its charge in electronic devices. One of the interesting phenomena being involved to spintronics is the magnetoresistance effect; it has already been employed in magnetic storage industry for a number of years. Among the various magnetoresistance effects of different origins, tunneling magnetoresistance effect (TMR) has showed its feasibility for the magnetic storage industry. Granular nanocomposites exhibiting TMR incorporated with the Coulomb Blockade effect in particular, have attracted much attention due to its simple structure which are more flexible to fabricate than multilayer systems,. TMR type granular nanocomposites normally consist of an insulating material acting as a matrix, with ferromagnetic nanoparticles embedded inside. Most of the reported insulating granular systems are fabricated with oxide materials acting as the matrix and the insulating barrier for the tunneling process. However, according to the spin-dependent transport mechanism, there are no reasons to exclude polymeric material to be utilized as the insulating matrix. Moreover, polymer as a light and pliable material has been used in various areas ranging from daily live to advanced engineering applications for over half of a century. It is obvious that polymer is playing an indispensable role, in particular for electronic device and sensor applications.

The studies in this thesis are mainly focused on the preparation of ferromagnetic metal-polymer composites and the investigations on the magnetoresistivity of the composites. Among the various fabrication techniques, pulsed laser deposition (PLD) is one of the versatile methods. Its versatility has been well-demonstrated by the success of depositing either single layer or multilayer thin films with epitaxy quality of ceramic and metallic materials. Apart from this, various kinds of polymer thin film fabricated by PLD have been confirmed to be successfully deposited on substrate. At present, most of the PLD work on polymers has been focused only on single polymeric material, but not much work are found on fabrication of composite film with two or more components. As a matter of fact, split-targeted PLD with two different components, which are metal and polymer in our case, are utilized.

Among various kinds of ferromagnetic elements like iron, cobalt and nickel, cobalt is chosen since it is not easily oxidized as iron and has a higher spin polarization then nickel. For the choice of polymeric materials, polytetrafluoethylene (PTFE) has been chosen owing to its several fascinating properties like excellent chemical stability and relatively high working temperature. Moreover, successfully deposited PTFE thin films fabricated by PLD have been reported. All of these have revealed the feasibility of the preparation of cobalt-PTFE granular composites with TMR effect. This study should open up a wide range of investigation in search of TMR type ferromagnetic metal-polymer nanocomposites with a compliant substrate which is relatively easy to fabricate. A kind of cost-effective and simple magnetic sensor prepared by the method presented in this study, which is applicable for magnetic data retrieving used in the magnetic hard-disks or in data storage as magnetic random access memories (MRAM), is anticipated.

In view of the fabrication of ferromagnetic metal-polymer composites, one important aspect is to fabricate nanoparticles. Apart from the above mentioned PLD technique, laser ablation can also be used to prepare nanoparticles in liquid under a normal atmospheric condition. It has been demonstrated that nanosized metal particles can be produced by pulsed laser ablation in liquid (PLAL), with metal targets placed in water or organic solvents. This technique can be further extended to fabricate nanocomposites if the fabricated nanoparticles are directly mixed with a polymer solution and evaporate the solvent later on. A study of the fabrication of cobalt nanoparticles in different kinds of solvent by PLAL technique will be presented in this thesis, providing ready-to-use fundamental experimental results for further investigation.

As a side track of the main study in this thesis, superhydrophobic PTFE film was successfully fabricated by PLD technique with a concern of some properties of PLD PTFE thin film. Unlike many reported techniques, which involve many complicated wet chemical processes, the fabrication process reported here is a dry method and relatively simple. A detail study of the surface morphology and structure correlated with the observed superhydrophobicity will be presented. The interesting behaviors obtained in these PLD PTFE films indicate the possibility of fabricating good self-cleaning surfaces for real applications, such as non-wetting protective layers on magnetic sensors and electronic components.

Owing to the unexpected experimental results obtained during the study of the cobalt-PTFE composites, the fabrication of cobalt hydroxide nanoplatelets was also studied. The morphology and crystal structure of the samples will be discussed in the thesis. Further investigations like the growth mechanisms and other physical properties of the prepared cobalt hydroxide platelets are needed in order to get a more clear conclusions and utilize this method to fabricate devices.

1.2 Literature Review

1.2.1 Pulsed Laser Deposition (PLD)

The first commercial high power ruby laser was made available and demonstrated in 1960 by Maiman [Maiman 1960]. Afterwards, intense laser beam interacted with solid surfaces has been studied theoretically and experimentally. The fact that intense laser beam is able to vaporize almost any material. It suggests that it could be used to deposit thin films. The first PLD, for growing thin films of various inorganic and organic materials by using a ruby laser, has been demonstrated in 1965 by Smith and Turner [Smith 1965]. However, this technique had not attracted much attention due to the limitation of the types of laser and too low repetition rate. Until almost 20 years later, in 1987, the successful growth by PLD of high-quality high-temperature T_c superconductor films was reported [Dijkkamp 1987]. Since then the PLD technique has experienced explosive growth.

PLD is a relatively simple technique which requires only some basic elements in the operation system as shown in Fig. 1.1. A pulsed laser beam being focused by a lens is directed toward a vacuum chamber through a laser transparent window. The laser beam is then focused on the target surface (rotating target), producing an energy density of up to several J/cm^2 and is absorbed by the target material. Only the surface layer of the ablated target is heated up due to the short pulse duration (it may vary according to the different types of laser) of each laser pulse. Consequently, all the absorbed laser energy is confined within the surface layer at which a few thousand degree can be achieved. Above a threshold of laser energy density, a tiny amount of material will be removed in the form of forward-directed plasma normal to the target surface. This threshold energy density is dependent on the target material, laser wavelength and laser pulse duration. The ejected species in the plasma plume, which contain neutral atoms, positive and negative ions, electrons, molecules, molecular ions and free radicals of the target material in their ground and excited states, are then deposited on the substrate to form a thin film. The film surface morphology will depend on the different processing conditions such as substrate temperature and vacuum pressure etc. Laser-solid interaction is a complex phenomenon which may involve different mechanisms such as evaporation, ionization, decomposition of the materials and the photo- and/or thermal-induced reactions. Chrisey and Hubler have given a more detailed discussion of the PLD process [Chrisey and Hubler 1994].

There are many advantages to utilize PLD for growing thin film. Since the laser is located outside the vacuum chamber, which in contrast to vacuum-installed devices like magnetron sputtering and electron-beam or ion-beam sputtering, provides a greater degree of flexibility in equipment arrangements. Almost any material in solid or liquid form can be ablated and the target material can be changed in situ during the deposition with suitable arrangement of the setup. Film thickness can be controlled to a high degree of precision, which can be down to atomic level. In fact, the minimum deposition is governed by a single laser pulse ablation, which often yields less than an atomic layer. Film growth rates can be easily controlled by altering the laser repetition rate. The use of small size target is also an advantage in contrast to the large size target required in sputtering process. Moreover, composite thin film can also be fabricated simply by using a composite target or multiple targets. Comparing with some other film deposition techniques, the requirement of vacuum condition of PLD is also less stringent and can be achieved with an economical double stage rotary pumping system. Film growth can also be carried out in a reactive ambient containing the reactive gases.

On the other hand, there are certain drawbacks in PLD. The presence of undesirable particulate in diameter of 1-10 μm generated by splashing effect, is an intrinsic problem in the PLD process. These particulates are hindrance in the formation of atomic flat film surface and will also influence the physical properties of the films. Besides, PLD is unfavorable to produce large area thin film of uniform thickness; this gives the PLD a great limitation to be operated in industries fabricating devices for microelectronic applications.

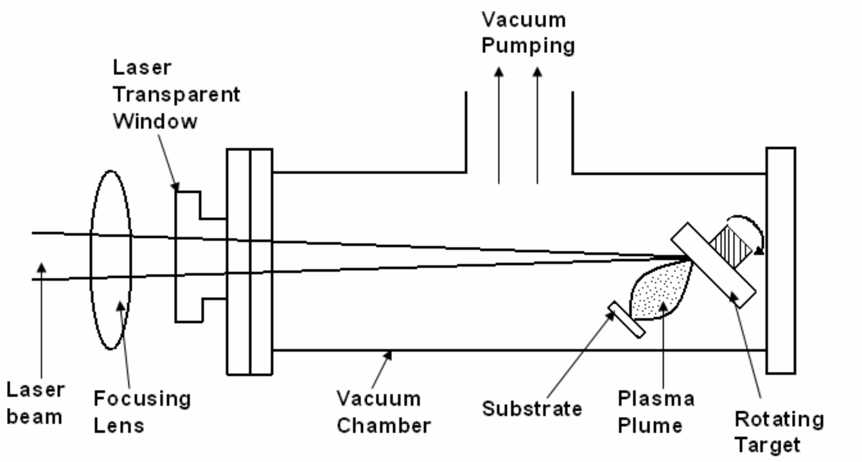

Figure 1.1: **Schematic diagram showing the basic elements of a PLD deposition system.**

1.2.2 PLD of Polymer

The first report of deposition of thin organic and polymeric films by PLD was made by Smith and Turner [Smith 1965] in 1965, who showed the growth of thin films of fuchsine (an organic dye) and Ni-dimethylglyoxime (a pigment used in paints and cosmetics). In the next 20 year, not much work was done in PLD of organic materials and polymers. Until 1988, Hansen and Robitaille demonstrated a significant amount of work on the deposition of films of several polymers by PLD, including polyethylene, polycarbonate, polyimide and polymethylmethacrylate (PMMA) [Hansen 1988]. In their experiments, laser wavelengths ranging from 193 nm to 1064 nm and laser energy densities of 0.01 - 2 J/cm^2 were used. Their results showed that the use of long wavelengths (1064 nm) led to a formation of numerous large particles of size larger than 5 μm on the deposited film surface. On the other hand, the use of ultraviolet (UV) which is strongly absorbed by polymers can produce smooth, pin-hole free surface with very little surface debris. They have also shown that film quality was enhanced by working at laser energies near the ablation threshold of the polymers. However, they also noted a decrease in the molecular weight of all the deposited films. An increasing size of particulates was found when the laser energy was raised significantly above (>2 times) the evaporation threshold. Typical growth rates of the polymer film obtained were 0.2 - 0.8 **Å** per laser pulse on a substrate located 3 cm from the target.

Recently, polymer and polymer-based material, especially in thin film form, attracted much attention both in science and industries due to their unique properties like chemical stability, flexibility, light-weighed, insulating properties (or on the contrary some with conducting properties) etc. However, not all polymeric materials can be dissolved and processed in common organic solvents. For these polymers, solution-based deposition techniques are not applicable, and alternative techniques are needed. PLD is one of the applicable methods for depositing polymeric thin film. The advantages of PLD technique as mentioned in the last section are also applied to depositing polymeric material. The drawbacks are the decomposition of polymers, decrease in the molecular weight and the existence of large particulates in the deposited films.

Nevertheless, a lot of research work has been conducted to prepare polymer thin films by PLD techniques. Among the many polymers had been used for this technique, polytetrafluoethylene (PTFE) with a trade name Teflon attracts much attention in using PLD. PTFE is well known for its chemical resistance and is also difficult to process. Various techniques have been investigated to deposit PTFE thin films such as vacuum evaporation, sputtering and plasma polymerization of fluorocarbon monomer gases etc. However, none of these techniques have a satisfactory result in forming PTFE thin films. Successful deposition of PTFE thin films by PLD was performed by Blanchet and co-workers [Blanchet 1993]. They showed that the formation of film is mainly occurred by laser-induced pyrolytic decomposition, followed by repolymerization. The unzipping and subsequent reconstruction of the polymer chains is also observed for addition polymers deposited by thermal evaporation processes. The UV laser pulses absorbed by the polymer can provide an efficient thermal source. The decrease on molecular weight of the polymer chains can be attributed to the partial repolymerization of the thermally unzipped monomers. However, it was found that during UV laser ablation, the fragmentation of the polymer chains can also occur due to the high photon energies, named as photolytic process, when the photon energies exceed the binding energies of most bonds in the polymer chains. Similar results were also obtained by Norton and co-workers, who demonstrated the growth of crystalline PTFE films as a function of substrate temperature [Jiang 1995, Norton 1996]. They have shown that the axis of the PTFE polymer chains on the crystalline films was aligned parallel to the substrate plane, as investigated by Transmission Electron Microscopy (TEM).

Besides, deposition of smooth crystalline PTFE films using an F_2 excimer laser in Ar background pressure of 200 mTorr with a substrate temperature of 97 °C has been demonstrated by Ueno and co-workers [Ueno 1994]. Deposition of PTFE but with fluorine deficient by using a XeCl excimer laser (308 nm) was also reported. Furthermore, crystalline PTFE films fabricated by PLD at laser wavelength of 248 nm, under an Ar back-ground pressure of 75-750 mTorr and at a substrate temperature of 300 °C, have been reported by Li and co-workers [Li 1998]. They have reported a high deposition rate of PTFE with PLD (up to 16 nm/sec) which are much higher than those obtained by other techniques.

The PTFE films generated by PLD can have many potential applications. For instance, aligning liquid crystals for display devices, charge retention stability for charge storage purpose incorporate with the low dielectric constant and excellent chemical stability make the PLD PTFE films useful for miniature electronic devices.

1.2.3 Giant Magnetoresistance (GMR)

Magnetoresistance (MR) is a phenomenon of which the resistance of a material will change when a magnetic field is applied to it; however for most of the materials the change is very small that cannot find any applications. In 1988, Baibich et al. [Baibich 1988] and Binash et al. [Binash 1989] independently discovered material systems of significantly large MR, they called it the Giant Magnetoresistance (GMR) effect. In their system, Fe/Cr (001) multilayers were grown by Molecular Beam Epitaxy (MBE). A large resistance drop was observed in an external magnetic field when the direction of the magnetizations in the neighboring Fe layers was changed from antiparallel to parallel alignment. A MR ratio of 20% at room temperature and 80% at 4.2K had been reported.

In the above material system configuration, a saturation field, H_s, was required to overcome the antiferromagnetic interlayer coupling between the Fe layers in order to align their magnetizations. It was found that the value of H_s was very large (in the order of 1 Tesla) in Fe/Cr multilayers at the early observations, which was not favorable for real applications. In 1994, a MR ratio of 220% at 1.5K has been reported again on the Fe/Cr multilayers, which was a result of the decrease in Fe layer thickness [Schad 1994]. The mechanism of GMR is mainly attributed to the spin dependent scattering by the defects and impurities of the magnetic layers and by the roughness of their interfaces. The different conduction behavior of the majority and minority spin electrons in a ferromagnetic metal, which was suggested by Mott [Mott 1936] also makes a significant contribution.

1.2.4 Tunneling Magnetoresistance (TMR)

The discovery of GMR effect triggered an extensive research effort on electron spin transport in magnetic nanostructures and their relating effects. One of the most important results is the tunneling magnetoresistance (TMR) effect of the magnetic tunnel junctions (MTJ). The first TMR experiment actually can be dated back to 1975, reported by Julliere [Julliere 1975]. However, huge amount of research work was started only when the first two observations of large and reproducible TMR effect were reported by Moodera and Miyazaki in 1995 [Miyazaki 1995]. Respectively CoFe/Al_2O_3/Co and Fe/Al_2O_3/Fe MTJs were used in their experiments, the amorphous alumina served as the tunneling barriers. The success of these work were attributed to the growth of ultra thin tunneling barriers without pinholes to short-circuit the two metallic layers.

A MTJ is composed of two ferromagnetic conducting layers separated by an ultrathin insulating layer. The insulating layer is very thin (a few nanometres or less) such that electrons can tunnel through the barrier if a bias voltage is applied between the two metal electrodes. In Julliere's earlier experiment, Co and Fe ferromagnetic layers of different coercive fields and an oxidized Ge barrier layer were used in the TMR device. A significant TMR value of about 14% was observed at 4.2 K at zero bias, but decreased very rapidly with increasing bias voltage. The large decrease in the TMR value with bias was attributed to the spin scattering at ferromagnetic-insulator interfaces.

Julliere proposed a model, which is the “spin dependent tunneling (SDT) model”, suggesting a difference in conductance between the parallel and anti-parallel magnetizations in the two ferromagnetic (FM) electrodes. In the model, he assumed that spin of electrons is conserved in the tunneling process and tunneling of up- and down-spin electrons are two independent processes, and so the conductance can be considered as two independent spin channels. Under a bias voltage, the current of the tunnel junction is proportional to the density of states at the Fermi level of both electrodes, which is illustrated by the density of states diagram as shown in Fig. 1.2.

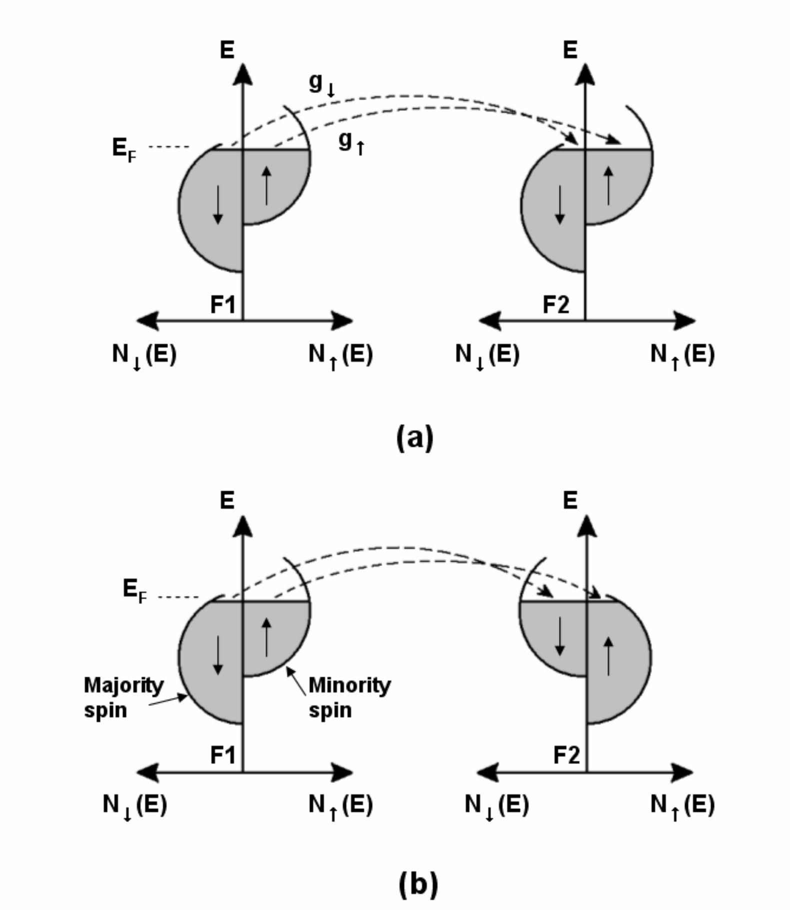

Figure 1.2: Density of states diagram describing spin-dependent tunneling (SDT) in MTJ. Magnetization orientations of the ferromagnetic layers (FM) are (a) parallel (b) antiparallel.

The conductance (g) of a metal is proportional to the density of states of electrons at the Fermi level, $N(E_F)$. The Pauli exclusion principle requires that up- and down-spin electrons be counted separately, and so separate spin subbands can be used. As shown in Fig. 1.1, for ferromagnetic metal, the up- and down-spin subbands shifted out of symmetry due to exchange splitting. In Fig. 1.2, the down-spin subband is called the majority spin subband because it has more electrons, and the up-spin subband is called minority spin subband consequently. The choice of up- (down-) spin for the minority (majority) spin subband is arbitrary, in which the direction refers to the orientation of the magnetic moment. Since the up- and down-spin subbands are different, therefore, the spin subband conductances are different:

$$N_{\uparrow}(E_F) \neq N_{\downarrow}(E_F), \quad g_{\uparrow}(E_F) \neq g_{\downarrow}(E_F)$$

According to Julliere's assumptions, the tunneling conductance for the parallel and antiparallel alignment, g_P and g_{AP}, can be written as follows:

$$g_P = g_P^{\uparrow} + g_P^{\downarrow} \propto N_{\uparrow 1}(E_F)\, N_{\uparrow 2}(E_F) + N_{\downarrow 1}(E_F)\, N_{\downarrow 2}(E_F),$$

$$g_{AP} = g_{AP}^{\uparrow} + g_{AP}^{\downarrow} \propto N_{\uparrow 1}(E_F)\, N_{\downarrow 2}(E_F) + N_{\downarrow 1}(E_F)\, N_{\uparrow 2}(E_F),$$

where $N_{\uparrow i}(E_F)$ and $N_{\downarrow i}(E_F)$ are the tunneling DOS of the ferromagnetic electrodes (i = 1, 2 represents the first and second ferromagnetic layer, respectively) for the up- and down-spin electrons.

When the magnetization orientations of the two ferromagnetic metal layers are parallel, as shown in Fig. 1.2 (a), the minority spin subband conductance ($g_P^{\uparrow}$) is large because the density of states at E_F is large for both ferromagnetic layers, which dominates the transport in the junction and produces a large total tunneling conductance. When the magnetization orientations are antiparallel, the up- and down-spin partial conductance are the same, the total conductance, $g_{AP} = g_{AP}{}^{\uparrow} + g_{AP}{}^{\downarrow}$, is smaller than that of the parallel configuration, $g_{AP} < g_P$, and so the antiparallel configuration will have a higher resistance than the configuration with magnetizations in parallel. This spin-dependent tunneling phenomenon is the origin of the MR observed in the MTJ.

The spin polarization (P) of the ith ferromagnetic layer is defined by:

$$P_i = (N_{\uparrow \mathrm{i}}(E_F) - N_{\downarrow \mathrm{i}}(E_F)) / (N_{\uparrow \mathrm{i}}(E_F) + N_{\downarrow \mathrm{i}}(E_F)),$$

The TMR value (following the definition of most researchers) can be expressed as:

$$\begin{aligned} \mathrm{TMR} &= (g_P - g_{AP}) / g_{AP} \\ &= 2P_1P_2 / (1 - P_1P_2) \end{aligned}$$

Julliere’s model provides a fairly good prediction of the TMR value in many MTJ structures with clean junction, by using the P values of different materials. Indeed, spin polarization (P) of various metals have been discovered and measured by Meservey and Tedrow [Meservey 1994]. The P values of different magnetic metals and compounds were measured by using the Zeeman-split quasi-particle density of states in a superconductor as the spin detector. Tunneling from a ferromagnetic film with unequal spin distribution at the Fermi level (E_F), into the superconducting Al film reflects the spin polarization of the tunneling electrons coming from the ferromagnetic film. The recent measured P values are higher which can be contributed to the improved junction preparation techniques such as Molecular Beam Epitaxy (MBE). The *P* values for various ferromagnetic materials measured by the above method were shown in Table 1.1.

Material	Ni	Co	Fe	$Ni_{80}Fe_{20}$	$Co_{50}Fe_{50}$	$Co_{84}Fe_{16}$
P (Old values)	23%	35%	40%	32%		
P (New values)	33%	45%	44%	48%	51%	49%

Table 1.1: Measured spin polarization values for various magnetic materials. [Moodera 1999]

After Julliere's experiment, the first accurate theoretical consideration of TMR was made by Slonczewski [Slonczewski 1989]. His results were the first important indications that spin polarization *P* may not be the characteristic of the electron structure of the ferromagnetic electrode alone and was allowed to have different sign or value in different tunneling junction. In most MTJ, the magnitude of the TMR decreases strongly with increasing bias voltage. The voltage dependence of TMR was studied by many researchers. It was found that the presence of defects like interface roughness, inter-diffused interfaces, impurities or vacancies, would provide a channel of impurity-assisted tunneling, which could decrease the spin dependent transport and the spin polarization of the tunneling [Tsymbal 2000, Tsymbal 2003]. Besides, it has also been reported that resonant tunneling mechanism originated from a distribution of impurity energy levels would result complex variations of the TMR with bias voltage and even an inverse TMR [Wunnicke 2002].

Temperature dependence of TMR has been studied and explained by Shang [Shang 1998]. In most tunnel junctions, TMR decreases with increasing temperature. Shang explained these results by assuming that the tunneling spin polarization *P* and the surface magnetization decreases with increasing temperature due to spin-wave excitations. Another possible explanation is the spin-flip scattering by magnetic impurities in the barrier proposed by Vedyayev et al [Vedyayev 2001]. The number of electrons contributing to this the spin-flip scattering increases with increasing temperature, and therefore resulting in the drop of TMR. Moreover, inelastic scattering with no flipping of electron spin, such as electron–phonon scattering, can also cause the reduction of TMR in the presence of localized states in the barrier, as demonstrated by Tsymbal et al [Tsymbal 2002].

Till now, various MTJs with different combinations of amorphous insulating material and magnetic materials including Ni, Co, Fe and alloys of these metals have been tested. It has been shown that an annealing of the multilayers under certain conditions almost doubles the TMR, attributed to a quality improvement of the amorphous barrier [Sousa 1998]. Large enhancement of TMR value has also been shown by the use of polycrystalline CoFe [Han 2000] and amorphous CoFeB [Wang 2004] electrodes, giving a TMR value of 50% and 70% respectively. Monocrystalline MgO has been used as the barrier materials recently [Djayaprawira 2005]. High TMR ratio have also been reported by utilizing different barrier materials like AlO_xN_y [Sharma 2000, Wang 2001], Ga_2O_3 [Li 2000], TaO_x [Rottlander 2001] and $ZrAlO_x$ [Wang 2001].

1.2.5 TMR in Granular Film

Recently, much research work, both experimentally and theoretically, have focused on the interplay between SDT and Coulomb blockade in ferromagnetic/insulator granular composite films. Consider a simple MTJ with a small grain of a ferromagnetic material located in the insulating barrier. The electrostatic energy will be increased by $e^2/2C$ when an electron tunnels into the grain, where C is the capacitance of the grain. Current will not flow at small bias voltages if the electrostatic energy of a single excess electron on the island is much larger than the thermal energy $\mathrm{k_B}T$. The suppression of current at small bias voltages is called "Coulomb blockade". If a few junctions (with large difference of resistance with respect to each other) are located in the insulating barrier, current will increase stepwise with bias voltage depending on the number of electrons accumulated on the island. Stepwise profile, named the "Coulomb staircase", can be observed. Coulomb blockade or staircase phenomenon has been reported by several groups in granular films with a nano-scale constriction [Mitani 2001, Yakushiji 2006]. The Coulomb blockade was not observed in normal granular films since a wide distribution of cluster sizes (hence, charging energies) in the structure tend to smear out the effect. It was also shown that the interplay of SDT and Coulomb blockade can lead to both an enhancement and an oscillatory bias dependence of the TMR in granular film. TMR ratio, in insulating granular systems, is normally defined as:

$$\mathrm{MR} = [\mathrm{R}(H) - \mathrm{R}(H_0)] / \mathrm{R}(H_0),$$

with H and H_0 being the applied magnetic field and zero magnetic field, respectively.

The first observation of TMR in insulating granular films was reported by Gittleman [Gittleman 1972] and by Helman and Abeles [Helman 1976], in which Ni-SiO_2 films were used. The electron conduction mechanism in insulating granular system was first studied by Sheng [Sheng 1973]. He proposed a model assuming that the ratio d/s (d is diameter of metal grain and s is the insulating barrier thickness) have same value for different region in the system, although the values of d and s have a wide distribution. It then follows that the product, sE_c, is a constant for a given composition, with E_c being the charging energy of the metallic granule. This model produces a temperature dependence of resistance R, which can be expressed in a functional form:

$$\ln R = 2(C/k_B T)^{1/2} + \text{constant},$$

where $C = (2\pi/h)(2m\phi)^{1/2}\, s\, E_c$, which was named the tunnel activation energy, ϕ is the effective barrier height, s is the separation between metallic granules (tunnel-barrier thickness), and E_c is the charging energy of the metallic granule. The linear relationship of ln$R$ against $T^{-1/2}$ is a common characteristic observed in most insulating granular films.

Recently, insulating granular films can be easily prepared by different methods such as sputtering, evaporation and PLD techniques. Different combination of materials have been investigated, including Co-SiO_2 [Milner 1996], Fe-MgF_2 [Furubayashi 1996], Fe-SiO_2 [Honda 1997], Fe-Al_2O_3 [Zhu 1999], (Fe-Co)-(Mg-F) [Kobayashi 2001], Co-ZrO_2 [Hattink 2006]. Insulating granular films with large TMR effect have been firstly reported by Fujimori, observed by using a Co-Al-O granular film [Fujimori 1995]. A linear relationship of ln$R$ against $T^{-1/2}$ was observed in the temperature dependence of conductivity of their system, which indicated that the conduction mechanism was contributed to the electrons tunneling through the insulating barrier between Co grains. The model used to explain the TMR observed in granular system was firstly proposed by Inoue and Maekawa [Inoue 1996]. Their model had utilized the SDT mechanism in MTJ by considering the spin polarization (P) of the magnetic material, and incorporated the relative magnetization of a granular system, $m = M/M_s$, with M_s being the saturation magnetization. TMR ratio is then given by:

$$\mathrm{TMR} = P^2m^2 / (1 + P^2m^2).$$

From the equation, it can be seen that magnetization of a granular system is an essential parameter to predict the TMR value. A wide particle size distribution is an intrinsic property in insulating granular systems. If the particle size in a granular system is small enough to reach the superparamagnetic state, and assuming the particles have a spherical body with same diameter d with negligible anisotropy energy, magnetization of the system can be described by the Langevin function:

$$M = M_o \,[\, \coth (\mu H/\mathrm{k_B}T) - (\mathrm{k_B}T/\mu H) \,],$$

which is equivalent to:

$$\mu = \mu_\mathrm{s} \,[\, \coth (\mu_\mathrm{p}H/\mathrm{k_B}T) - (\mathrm{k_B}T/\mu_\mathrm{p}H) \,],$$

where μ is the measured total magnetic moment of the system at an applied magnetic field, μ_s is the measured total magnetic moment of the system at saturation and μ_p is the magnetic moment of one nanoparticle. A log-normal distribution function is always used to describe the distribution of d value in the real system. The Langevin fitting incorporated with the log-normal distribution function gives good result in many nanogranular systems [Batllle 2002].

The model proposed by Inoue and Maekawa gives good prediction for the TMR value observed in insulating granular system at room temperature. Since the TMR value depends on m^2, weak temperature dependence of MR should be expected. However, many insulating granular systems show large enhancement of TMR value at low temperature. The observed phenomenon was explained by Mitani with a model considering the higher order process of spin-dependent tunneling (cotunneling) of electrons [Mitani 1998]. As shown in Fig. 1.3, due to the broad particle size distribution appearing in most insulating granular systems, large particles are mostly well separated from each other in between smaller particles due to their low number density (i.e. the larger the granule size, the more separated the granules).

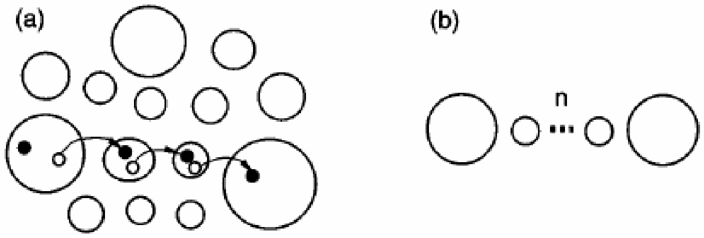

Figure 1.3: **(a) Schematic diagram of granular structure and a higher-order tunneling process where a charge carrier is transferred from the charged large granule, through the two small ones, to the neutral large one; (b) Model structure used for the calculation of conductivity [Mitani 1998].**

In this structure, co-tunneling process will become important. In co-tunneling process, an electron tunnels into an island while the second electron simultaneously leaves the island through the other junction, such that the island is only virtually charged during the process but with no increase in charging energy in the overall tunneling process. They have shown that at low enough temperature, the dominant conduction process is coming from the cotunneling, where the charge carrier is transferred from the charged large particle to the neighboring neutral large particle through an array of small particles. The temperature dependence of MR can be simplified as:

$$\mathrm{MR} = 1 - (1 + P^2m^2)^{-(n^*+1)},$$

where $n^* = (E_c/8ks\mathrm{k_B}T)^{1/2}$ with $\mathrm{k_B} = 1$. This model gives reasonable prediction of the MR enhancement in different insulating granular system as reported. In fact, the suppression of spin-flip scattering processes due to magnetic impurities contained in the tunneling barrier, may contribute to the large enhancement of MR at low temperature as reported by Zhu and Wang [Zhu 1999]. Decay of spin polarization and intergrain correlation may also be the crucial factors for the temperature dependence of MR observed in the insulating granular system [Slonczewski 1989, Sheng 2002].

1.2.6 Pulsed Laser Ablation in Liquid (PLAL)

The pioneer work of PLAL was reported in 1987, in which a metastable phase of iron oxides was fabricated by ablating an iron target in water [Patil 1987]. After that, the fabrications of different nano-sized metal particles and metal compounds have been studied by different researchers [Simakin 2001, Dolgaev 2002, Chen 2004, Tsuji 2005]. The first physical and chemical study of PLAL process was reported by Fabbro and co-workers [Fabbro 1990]. They reported that PLAL can create high-density shock wave by laser-induced plasma due to the liquid-confinement effect. A detailed discussion of the process was also reported by Yang [Yang 2007]. The process can be described by the three stages schematically illustrated in Fig. 1.4.

Firstly, as shown in Fig. 1.4 (a), the laser-induced plasma is formed due to the laser irradiation, and creating a shock wave under the confinement of liquid.

Later on, as shown in Fig. 1.4 (b), when more vaporizing species are produced due to the further absorption of the later coming laser pulses, the shock wave will induce an extra pressure (plasma-induced pressure) in the laser-induced plasma causing the plasma to expand, and subsequently lead to an additional temperature increase of the laser-induced plasma. It has been reported that the temperature can be raised to 4000 ~ 5000 K, and the pressure can be about 10 GPa in the laser-induced plasma [Yang 1998]. During this process, several chemical reactions can take place inside the laser-induced plasma and at the interface between the liquid and the laser-induced plasma due to the generated high temperature and pressure. Chemical reactions can occur in between the vaporized target species inside the laser-induced plasma. Reactions can also take place in between the species generated from the target and the liquid at the plasma-liquid interface due to the high temperature and pressure. Moreover, the high pressure in front of the laser-induced plasma can impinge the ablation species from the plasma-liquid interface into the liquid, and thus, the chemical reactions between the target species and the liquid species can also occur inside the liquid.

The last stage is the cooling down and condensation of the plasma plume in the confining liquid, as shown in Fig. 1.4 (c). It is possible that a part of the plasma plume would condense and deposit back on the surface of the solid target and lead to the formation of a surface coating, due to the plasma quenching and the confined pressure from the liquid. But mostly, the plasma plume will condense and be dispersed into the liquid during the plasma quenching, due to the cooling down of the confining liquid. Nanoparticles are then fabricated during the condensation of the plasma. These nanoparticles will normally float on the surface of the liquid due to their large surface tension.

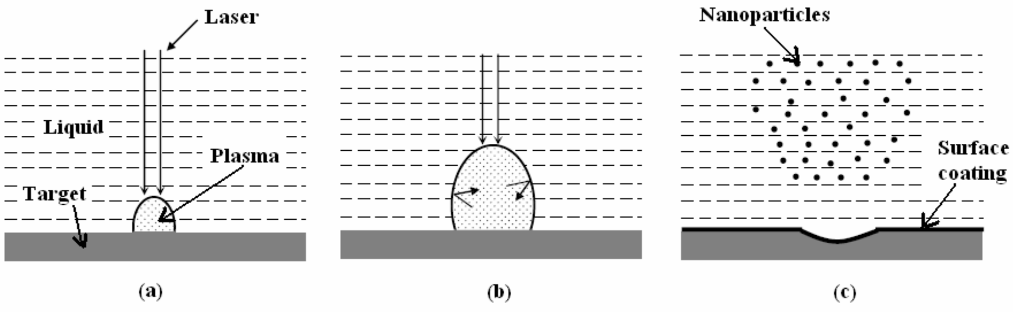

Figure 1.4: **Schematic diagram of the formation of nanoparticles in the solid-liquid interface during PLAL. (a) The generation of the laser-induced plasma due to the laser irradiation on the target. (b) The expansion of the plasma plume in liquid due to the absorbing the later laser pulse and the plasma-induced pressure created by the shock wave. (c) Formation of nanoparticles and surface coating on target surface due to the condensation of the plasma plume in liquid.**

1.3 Outline of thesis

The studies reported in this thesis can be divided into three parts. (1) The fabrication of ferromagnetic metal - polymer granular composite films and the magnetoresistivity of such composite films will be investigated. The focus of the composite system will be a combination of cobalt and PTFE. Cobalt is one of the elemental metals, which is ferromagnetic. Its magnetic moment is slightly lower than iron but it is not easily oxidized as iron. PTFE is one of the best plastics for engineering applications. This is the first that such composite films will be fabricated by PLD method and attention will be focused on its magnetoresistivity. As GMR effect was discovered for almost 20 years, subsequently the debut of TMR makes the magnetoresistivity a useful effect for application in magnetic storage devices industry. Cobalt ablated by the pulsed laser in liquid will also be investigated. The properties of the nanosized cobalt particles prepared by this method are studied. The results show that this is one of the simplest methods to prepare nanosized particles without the use of any sophisticated equipment. (2) Fabrication of superhydrophobic polytetrafluoroethylene thin film by pulsed laser deposition technique. The result infers that this technique can be utilized for producing good self-cleaning surface in real applications. (3) Fabrication of cobalt hydroxide hexagonal platelets on glass substrates by laser deposition incorporated with simple chemical reaction is studied. Further studies of these cobalt hydroxides on the growth mechanism and in real applications are of potential interests.

This thesis contains seven chapters. Chapter 1 will give the background of the study and a comprehensive literature review of the topics concerned.

In Chapter 2, different experimental process and parameters used in the present studies is presented. Different sample characterization techniques are also described.

In Chapter 3, cobalt-polytetrafluoroethylene granular composite film fabricated on glass substrate by using pulsed laser deposition technique is reported. An emphasis is placed on the magnetoresistivity both at room temperature and low temperature. The surface morphology, microstructures, electrical and magnetic properties of the cobalt-polytetrafluoroethylene granular composite film is also discussed.

Fabrication of cobalt nanoparticles produced by pulsed laser ablation in liquid is reported in Chapter 4. Microstructures and size distribution of the nanoparticles fabricated in different solvent is discussed. This chapter collected some fundamental experimental results for future use such as fabricating metal-polymer nanocomposites.

In Chapter 5, fabrication of superhydrophobic polytetrafluoroethylene thin film by pulsed laser deposition technique is reported. The measured contact angle is correlated with the surface morphology and roughness.

Chapter 6 reports the formation of cobalt hydroxide hexagonal platelets on glass substrates by laser deposition incorporated with simple chemical reaction. The surface morphology and structural properties of the hexagonal nano-sized cobalt hydroxide are characterized.

Conclusions of this thesis with a summary of important results and achievements obtained in the present studies are given in Chapter 7.

CHAPTER 2

Sample Preparations and Characterizations

2.1 Cobalt-Polytetrafluoroethylene Granular Composite Film on Glass Substrate

Sample Preparations

Cobalt-PTFE granular composite thin film was prepared on glass substrates by using Pulsed Laser Deposition (PLD) technique at room temperature. An Nd:YAG laser (Spectra-Physics GCR 16) at a repetition rate of 10 Hz was used in the samples fabrication. In order to deposit different materials to form composite film in-situ in a vacuum chamber, a splitting target method is developed for this purpose. As shown in Figure 2.1, the semi-circular cobalt metal target is placed in a position coplanar with the semi-circular PTFE target in the holder. The target holder is driven by a computer controlled stepping motor. The composition of the deposited film can be easily adjusted by controlling the duration of the targets exposed to the pulsed laser. As the film was deposited on the glass substrates, they were first cut into small pieces by a glass cutter. All of them were cleaned with acetone, ethanol and deionized water subsequently and then dried up in air at room temperature. Two gold electrodes, with a gap in between, were sputtered on each glass substrate with the use of a mask. The thickness of the gold electrode was estimated to be about 100 nm. The gold electrodes were used for electrical measurements of the composite films.

Two semi-circular cobalt and PTFE plates were used as the target material in the PLD process. Both of them were cut into semi-circular shape from a circular target and the surfaces were polished by silicon carbide paper before use.

For the PLD process, the glass substrate with gold electrodes on top was put on a substrate holder in a vacuum chamber. The semi-circular Cobalt and PTFE plates forming a split target was used in the PLD. The split target was mounted on a holder physically which was swung through a computer controlled stepping motor. The composition of the film was changed by varying the swing ratio between the metal and polymer targets, i.e. varying the laser pulse ratio of the metal to polymer. The vacuum chamber was then evacuated by a rotary pump for about 90 min. The vacuum pressure was checked by a Pirani Gauge. Finally, the laser beam was focused by a lens, passing through a laser transparent window, onto the target surface. The composite film was then deposited on to the glass substrate with a pair of gold electrodes. Two kinds of composite films were fabricated, by using the fundamental wavelength (λ = 1064 nm) and the third harmonic (λ = 355 nm) of the Nd:YAG laser, respectively. Some of the important parameters used in the PLD process and dimensions of the deposited films were shown in Table 2.1. A schematic diagram of the top-view and cross-section of a cobalt-PTFE composite film on glass substrate with gold electrodes was illustrated in Fig. 2.2 (a) and (b) respectively.

For investigation of the polymer matrix structures, the prepared cobalt-PTFE composite films were etched by hydrochloric acid (HCl) to remove the deposited cobalt particles located in the polymer matrix. Drops of concentrate HCl were added into deionized water in order to obtain diluted HCl solution with a concentration of

~0.1 M. Half of the composite film was then put into the 0.1 M HCl solution for about 20 second (the reaction time is not an absolute value). Significant color change of the film, from brownish-grey to nearly colorless, can be observed which indicating most of the cobalt particles were etched away. The film was then dried up in air at room temperature without any further treatment for further investigation.

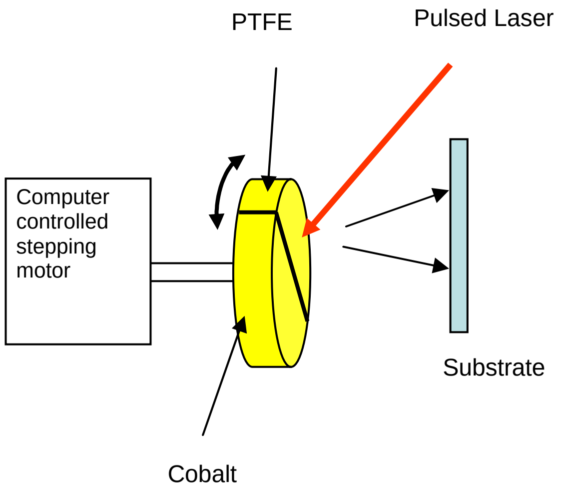

Figure 2.1: **Splitting target holder for PLD.**

	IR-PLD samples	***UV-PLD samples***
Laser wavelength	1064 nm	355 nm
Laser spot size (Diameter)	~ 1 - 1.2 mm	~ 1 - 1.2 mm
Laser fluence	~ 30 J/cm^2	~ 2 J/cm^2
Substrate-to-Target distance	3 cm	3 cm
Deposition time	15 min	15 min
Vacuum condition	~ 10 mTorr	~ 10 mTorr
Film Area (in between the gap of the gold electrodes)	2 mm x 5 mm	1 mm x 5 mm
Film thickness	~ 100 - 200 nm	~ 200 - 300 nm

Table 2.1: **Some important parameters in PLD process for fabrication of cobalt-PTFE composite films and dimensions of the deposited films.**

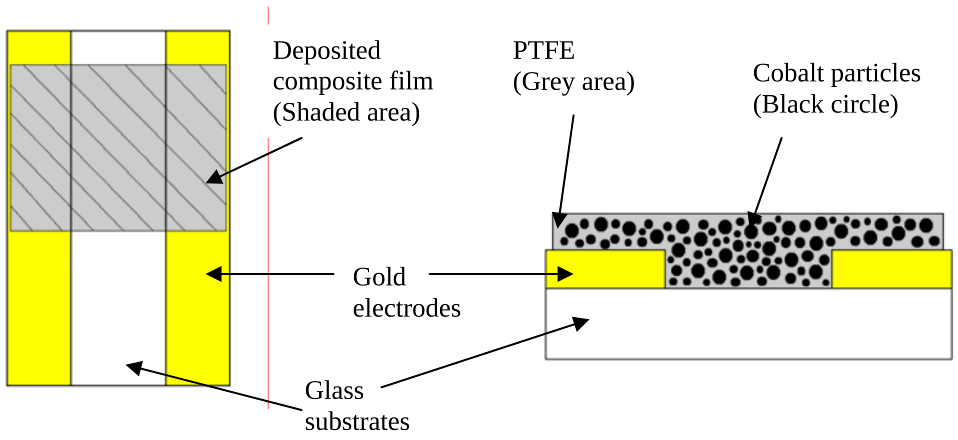

(a) (b)

Figure 2.2: **Schematic diagram of the (a) top-view and (b) cross-section of a cobalt-PTFE composite film on glass substrate with gold electrodes.**

Sample Characterizations

The chemical structure of the samples was investigated by Infrared absorption spectra. The absorption spectra of the samples were measured with a Fourier Transform Infrared (FTIR) spectrometer (NICOLET MAGNA-IR 760). The prepared samples were put into the spectrometer without further treatment and were investigated through Specular Reflectance technique.

The surface and cross-section morphology of the prepared samples was inspected by a field-emission scanning electron microscope (SEM) (JEOL JSM-6335F) at a voltage of 3 kV. Very thin gold layer (generally 10-20 nm thick) was sputtered on every sample’s surface before SEM investigation in order to enhance the emission of secondary electrons, reduction of thermal damages as well as the elimination of charging effect.

The particle size and structure in the samples was investigated by Transmission Electron Microscope (TEM) (JEOL 2010F TEM). The composite films were directly deposited on carbon-coated copper grid by PLD at room temperature. The deposition time was 7 min in order to produce a film with size thin enough for TEM investigations.

The magnetic properties of the samples were measured with a vibrating sample magnetometer (VSM) equipped with a cryostat for low temperature measurement. Samples with weak magnetic signals were measured with a Superconducting Quantum Interference Device (SQUID) Magnetometer (MPMS-5s) equipped with a superconducting magnet. Each data point was taken every 10 seconds.

All resistance measurements were performed using the two terminal method with an electrometer (KEITHLEY 6517A) with internal source provided. Copper wires connected to the gold electrodes by silver paste were used as the electrical contact. A helium filled close cycle cryostat was used for the temperature dependence of resistance measurements, with samples mounted on a cold finger. Magnetic field for the magnetoresistance measurements was produced by an electromagnet (LDJ 9500). Temperature dependence of magnetoresistance measurements were measured in helium filled close cycle cryostat placed in an electromagnet (LDJ 9500).

2.2 Cobalt Nanoparticles Fabricated by Laser Ablation in Liquid

Sample Preparations

The target used in this study is a metal disk of cobalt (2.5 cm in diameter). At the beginning, the target was first put in acetone, ethanol and then deionized water in sequence vibrated with an ultrasonic cleaner, in order to remove organic contaminations. In this study, hexane, ethanol and toluene were used as the solvent. The distance between the solvent surface and the target surface was kept at about 6 mm for all ablation process. An Nd:YAG laser (Spectra-Physics GCR 16) with a repetition rate of 10 Hz was used in this study, with the use of second harmonic wavelength of 532 nm.

Fig. 2.3 shows the schematic diagram of the PLAL setup used in this study. The laser beam was first reflected down to the liquid surface, being focused by a convex lens, and finally onto the target surface immersed in the solvent. The laser spot on the target surface has a diameter of about 1 mm. The laser fluence before entering any solvent was about 3 J/cm^2. During laser ablation, the target was rotated constantly by using a rotating motor or moved horizontally along X or Y directions by a computer-control X-Y stage in order to perform laser rastering on the target surface, ensuring uniform laser ablation of the target surface and well dispersion of the fabricated nanoparticles.

For all kinds of solvent, the laser ablation time was kept at about 30 min for each collection of the colloidal solution. Several collections of the colloidal solution were then transferred to a glass bottle in order to increase the concentration of the nanoparticles in the solvent. A small amount of black particles, which could be seen by naked eyes, was appeared in the solvent on the side of the glass bottle after putting a magnet near the glass bottle for about 24 hours. This indicated that cobalt nanoparticles with magnetic properties were successfully fabricated. The remaining solvent was poured away while keeping the magnetic black particles with small amount of the solvent inside the glass bottle. Finally, the other freshly prepared collections of colloidal solution were poured into the same glass bottle again. The above process was repeated several times until significant amount of magnetic black particles were observed by naked eyes. In addition, nearly no color change of the solution was observed after laser ablation in hexane. For laser ablation in both ethanol and toluene, the solution was changed from colorless to yellowish-grey. The yellowish liquid have no effect with applied magnetic field.

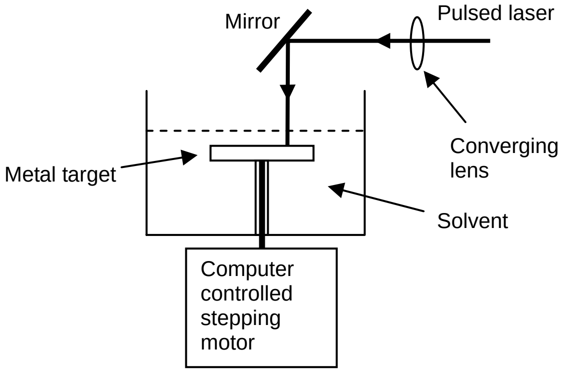

Figure 2.3: Schematic diagram of the setup used in the process of pulsed laser ablation in liquid (PLAL).

Sample Characterizations

The particle size and morphology was investigated by SEM. Two kinds of preparation were performed. (1) The black particles in the colloidal solution, which can be seen by naked eyes due to agglomeration, were well dispersed in the solvent by an ultrasonic vibrator. Then a drop of the colloidal solution was put on a clean silicon wafer as substrate and dried up in air at room temperature for investigations directly. In this case, the searching of the particles under SEM were very difficult since only very few particles separated far away with each other were located on the substrate surface. (2) The black particles in the colloidal solution were firstly attracted by a magnet. The agglomerated particles, with size that can be seen by naked eyes, were transferred on the substrate surface directly. In this case, particles were easily found on the substrate surface but with serious agglomerations. A field-emission scanning electron microscope (SEM) (JEOL JSM-6335F) at a voltage of 3 kV was used throughout the investigations.

For TEM investigation, a drop of well dispersed colloidal solution with volume of about 5 μL was placed on the carbon-coated copper grid. The sample was then dried up in air at room temperature for more than 12 hr. The particle size and structure was investigated by a Transmission Electron Microscope (JEOL JEM 2010).

2.3 Superhydrophobic Polytetrafluoroethylene Thin Film Fabricated by Pulsed Laser Deposition

Sample Preparations

PTFE thin film was deposited on glass cover slides by PLD at room temperature. A KrF excimer laser (λ=248nm, Lambda Physik COMPex 205) with laser pulse duration of about 25 ns at a repetition rate of 10 Hz was used in the samples fabrication. All of the glass cover slides were first cleaned with acetone, ethanol and deionized water subsequently and then dried up in air at room temperature. Circular PTFE target was used as the target material in the PLD process. The PTFE target was mounted on a target holder and rotated by a rotating motor during laser ablation. The PTFE targets were polished by silicon carbide paper before use. Similar PLD process described in section 2.1 was used for all samples preparation. Some of the important parameters used in the PLD process were shown in Table 2.2.

Laser wavelength	248 nm
Laser spot area (on target surface)	~ 3.5 mm x 5 mm
Laser fluence	~ 1 J/cm^2
Substrate-to-Target distance	3 cm
Vacuum condition	~ 10 mTorr
Effective Area of Deposited Film	~ 1.5 cm x 1.5 cm

Table 2.2: Some important parameters in PLD process for fabrication of superhydrophobic PTFE films.

Sample Characterizations

The chemical structure of the samples was investigated by Infrared absorption spectra, measured with a Fourier Transform Infrared (FTIR) spectrometer (NICOLET MAGNA-IR 760). Potassium Bromide (KBr) particles, a kind of IR transparent material, were grinded into smaller size and mixed with the PLD deposited PTFE film. The KBr particles with the samples were then pressed into a pellet, and put into the spectrometer and were investigated through Transmission technique.

The surface morphology of the prepared samples was inspected by a scanning electron microscope (SEM) (Leica Stereoscan 440). Very thin gold layer (generally 10-20 nm thick) was sputtered on every sample’s surface before SEM investigation in order to enhance the emission of secondary electrons, reduction of thermal damages as well as the elimination of charging effect.

Atomic Force Microscope (AFM) (Veeco NanoScope IIIa, tapping-mode, etched silicon probe) was used to examine the surface morphology and the surface roughness (rms) of the PTFE thin film deposited on glass substrates.

The contact angle was measured using a Standard Automated contact angle goniometer (Rame-Hart, Model 200-F1) with deionized water. Water droplets of volume ranging from 2 μL to 10 μL were used in these measurements.

2.4 Preparation of nano-sized cobalt hydroxide by laser deposition process

Sample Preparations

For the preparation of cobalt hydroxide platelets, cobalt thin film was firstly deposited on glass substrates by PLD at room temperature. An Nd:YAG laser (Spectra-Physics GCR 16) with a repetition rate of 10 Hz was used in the samples fabrication. The glass substrates were first cut into small pieces by a glass cutter. All of them were first cleaned with acetone, ethanol and deionized water subsequently and then dried up in air at room temperature. Circular cobalt target was used as the target material in the PLD process. The cobalt target was mounted on a target holder and rotated by a rotating motor during laser ablation. Silicon carbide paper was used for polishing the target surface before use. Similar PLD process was described in section 2.1. Important parameters used in the PLD process were shown in Table 2.3.

Laser wavelength	532 nm
Laser spot area (Diameter)	~ 1.5 mm
Laser fluence	~ 4.5 J/cm^2
Substrate-to-Target distance	3 cm
Vacuum condition	~ 10 mTorr
Deposition time	15 min

Table 2.3: Some important parameters in PLD process for fabrication of cobalt thin films.

Sodium hydroxide (NaOH) solution with a concentration of 0.5 M was prepared by dissolving a suitable amount of NaOH pellets into distilled water. The PLD deposited cobalt films were then immersed into the NaOH solution for about 90 min. The reaction time was not an absolute value. It was found that the colour of the cobalt film would change from shiny metallic grey to nearly completely white, after immersing into the solution for about 90 min. No significant colour change could be observed later on, indicated that the reaction was becoming mild or even stopped. The reacted film was then immersed into distilled water and rinsed for three times in order to remove any residual NaOH on the film. The film was finally dried up in air at room temperature for investigations.

Sample Characterizations

The surface morphology of the prepared samples was inspected by scanning electron microscopes (SEM) (model: Leica Stereoscan 440 and JEOL JSM-6335F). Very thin gold layer (generally 10-20 nm thick) was sputtered on every sample's surface before SEM investigation in order to enhance the emission of secondary electrons, reduction of thermal damages as well as the elimination of charging effect.

The chemical structure of the samples was investigated by Infrared absorption spectra, measured with a Fourier Transform Infrared (FTIR) spectrometer (NICOLET MAGNA-IR 760). The prepared samples were put into the spectrometer directly and were investigated through transmission configuration.

The crystal structure of the samples was identified by an X-Ray diffractometer (TF-XRD, Philips X'pert Systems), with Cu Kα radiation (40 kV, 35mA). A scan rate of 0.1 °/s was used.

CHAPTER 3

Cobalt-Polytetrafluoroethylene Granular Composite Film on Glass Substrate

3.1 Introduction

Metal-insulator granular composite materials, consisting of nano-sized ferromagnetic metal particles embedded in an insulating matrix would exhibit magnetoresistance effect. For instance, the Ni-SiO_2 granular films studied by Gittleman et al. [Gittleman 1972] show a large tunneling magnetoresistance (TMR) effect. This effect of the granular films observed is caused by the spin-dependent tunneling of electrons between the magnetic particles through the insulator [Mitani 1997]. Subsequently, different granular films with ferromagnetic particles (Fe, Co, CoFe) embedded in various kinds of inorganic insulating matrix (Al_2O_3, SiO_2, MgF_2) have been studied in details [Honda 1997, Ohnuma 1997, Zhu 1999, Kobayashi 2001], with different fabricating techniques including co-sputtering and Pulsed Laser Deposition (PLD) methods. These granular composites can be prepared in form of thin film and have been developed for sensing, optical and medical applications as well as data recording and storage. Although multilayer-type TMR systems with large MR value have been reported, very high quality of the fabrication process is required in order to avoid any metallic pinholes and large disorderness formed in the insulator layer which may cause breakdown when operated with a low applied voltage. Moreover, the MR value will decrease with increasing bias voltage. For insulating granular system, it is possible to overcome the above unfavourable factors. In considering of making sensors, insulating granular system is also better than multilayer type TMR system. A reverse magnetic field is needed in order to change the resistance state in the multilayer type TMR system, while the resistance state of granular type system will immediately go back to the origin state when a magnetic field is removed due to the superparamagnetic behaviour. On the other hand, magnetic nanoparticles composite system with polymer as the insulating matrix has also been investigated but being focused on their optical properties and the microstructures [Pelecky 1996, Park 2003, Faupel 2004, Maceira 2006, Roder 2006, Schurmann 2006], while their magnetoresistance have not gained much attention. Composites utilizing polytetrafluoroethylene (PTFE) as the matrix material fabricated by PLD has also been reported, while the study was mainly focused on the dielectric permittivity and electromechanical strain [Vrejoiu 2003].

However, based on the spin-dependent tunneling mechanism, there should not be any physical reason to exclude using the organic materials, such as the polymers to serve as the insulating phase from obtaining the TMR effect.

In this chapter, a type of granular composite film prepared by using the PLD technique was studied. The composite consists of the polymer PTFE as the insulating matrix and the ferromagnetic cobalt particles as the granular phase. It is well-known that PTFE have excellent chemical stability among the polymers and its working temperature can be close to 250°C. It is no doubt that this type of granular composite film with PTFE as the matrix can maintain its performance even in harsh environment.

Fundamental wavelength (1064 nm) and the third harmonic (355 nm) of the Nd:YAG laser were used to fabricate two series of samples in the PLD process. The fundamental wavelength, which is in the IR region, was first attempted because of its higher output energy. Since metal-polymer composite films are going to be deposited, relatively high laser fluence is needed in order to obtain efficient ablation of metal by the IR. However, due to the high laser fluence used thermal degradation and carbonization of the polymer and also the formation of particulates were resulted in the deposition. Accordingly third harmonic (355 nm) of the Nd:YAG laser, which is in the UV region, was also chosen in the sample fabrication process. A lower laser fluence threshold is enough for metal to obtain efficient ablation because of the higher photon energy and at the same time thermal damage of the polymer can be minimized. These two series of samples were studied and the results will be presented in the following sections. The nomenclature "**IR-PLD samples**" will be given to samples fabricated by the laser of IR wavelength and "**UV-PLD samples**" will be used to describe samples fabricated by the laser of UV wavelength.

The Infrared Spectroscopy, microstructure, magnetic and electrical properties as well as magnetoresistance of the prepared films had been studied. The experimental results reveal that our composite samples consist of the nano-sized cobalt particles embedded homogenously in the PTFE matrix. These samples process interesting properties like spin-dependent tunneling effect and show the superparamagnetic relaxation behavior which is common in many nanostructured magnetic granular materials.

3.2 Infrared Spectroscopy

Fig. 3.1 (a) and (b) show the Fourier Transform Infra-Red (FTIR) spectra of the PTFE target and the PTFE film produced by PLD using laser of wavelength 1064 nm. The absorption peaks at 1300-1100 cm^{-1} are assigned to the asymmetrical and symmetrical stretching modes of CF_2 bond, which is a typical characteristic absorption band for the fluoropolymer. The peaks with smaller intensity at around 640-620 cm^{-1} are attributed to the chain stretching and wagging modes of CF_2 bond, while the bending and rocking modes are at around 553-505 cm^{-1} [Li 1998]. As both spectra obtained from the target and the film show very similar features, it can be confirmed that the composition of the PTFE film produced was almost the same as the target material.

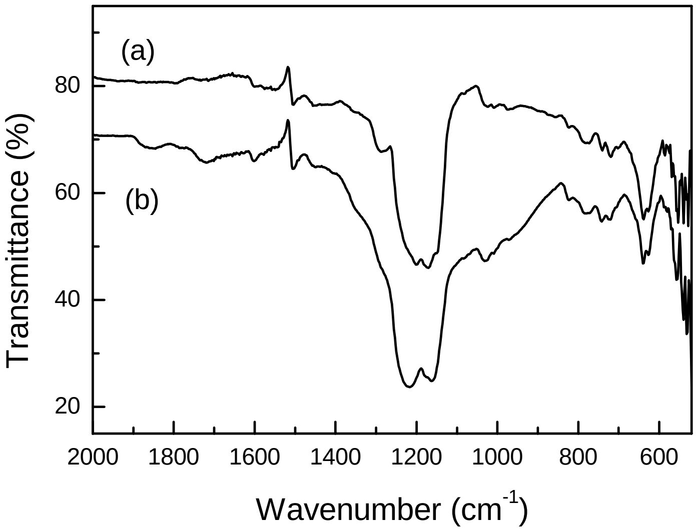

Figure 3.1 **FTIR spectra of (a) bulk PTFE and (b) PTFE film produced by PLD (IR-PLD samples).**

Fig. 3.2 and 3.3 show the FTIR spectra of Co-PTFE composite films of IR-PLD and UV-PLD samples respectively.The relatively noisy spectra at around 1800-1400 cm^{-1} is mainly due to the unbalanced ratio of the water vapor background. . Most of the characteristic absorption peaks of PTFE appear in the spectrum of both samples, which confirms that PTFE-containing composite film was successfully deposited. One interesting point is that the absorption peaks in the spectrum of the IR wavelength laser deposited sample are less significant to differentiate which may due to the higher thermal damage and degradation of the polymer caused in the deposition process. In addition, the PTFE films fabricated by using both laser wavelengths also appear a very light yellowish-grey color, as reported from other study, which is possibly due to the fluorine deficiency in the samples [Holland 1976].

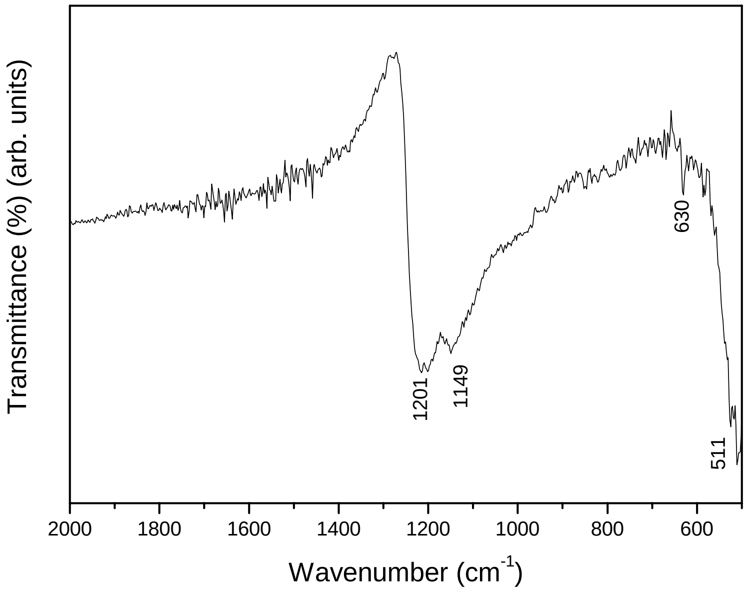

Figure 3.2 **FTIR spectra of Co-PTFE composite film (IR-PLD samples).**

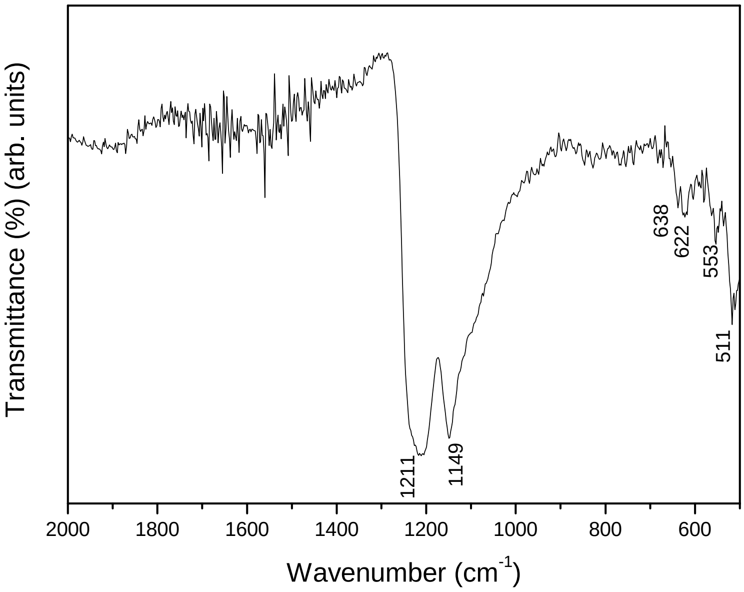

Figure 3.3 FTIR spectra of Co-PTFE composite film (UV-PLD samples).

3.3 Microstructure of the composite films

The SEM images of the Co-PTFE composite films (IR-PLD and UV-PLD samples) are shown in Fig. 3.4 and Fig. 3.6 respectively and the corresponding higher magnification images are shown in Fig. 3.5 and Fig. 3.7. Similar granular morphologies were found on both samples. In general, there exist two kinds of particles. One kind is the sphere-like particles of sizes smaller than 50 nm which are the cobalt particles. The others are particles of sizes larger than 200 nm with irregular shape, appearing brighter, which is due to the charge accumulation. These are PTFE particulates that were commonly found in the deposition of polymeric materials by PLD [Li 1998].

However, it is still difficult to differentiate the metal and the polymer phase. It is well-known that PTFE have excellent chemical stability, in order to differentiate the cobalt and PTFE phase, diluted hydrochloric acid (HCl) was used to remove the Co particles and therefore, leaving the PTFE matrix on the substrate.

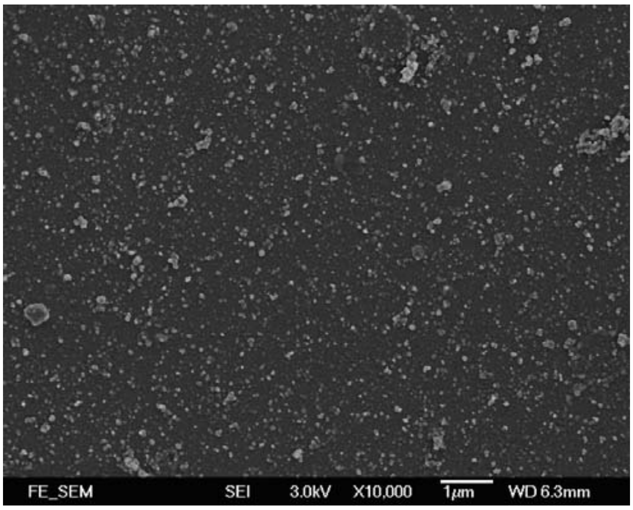

Figure 3.4 SEM image of Co-PTFE composite film (IR-PLD samples).

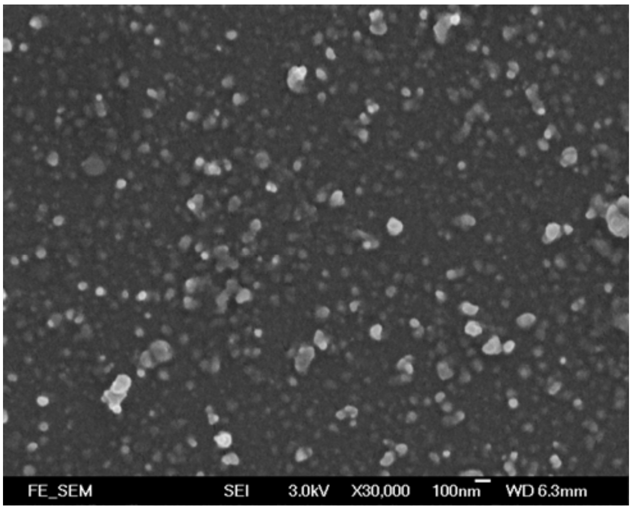

Figure 3.5 A higher magnification image of Co-PTFE composite film (IR-PLD samples).

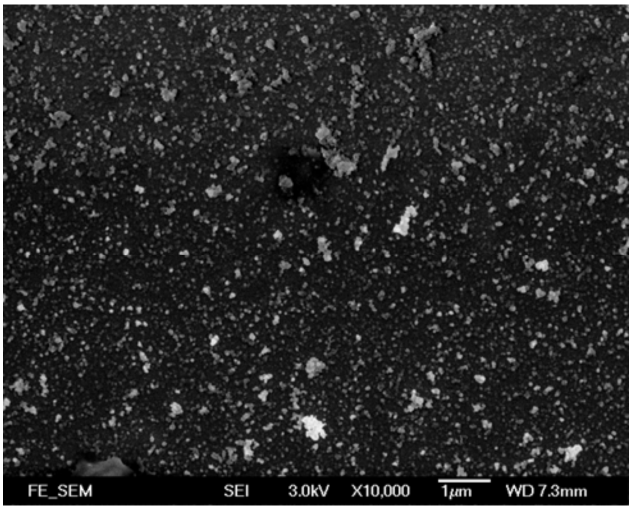

Figure 3.6 SEM image of Co-PTFE composite film (UV-PLD samples).

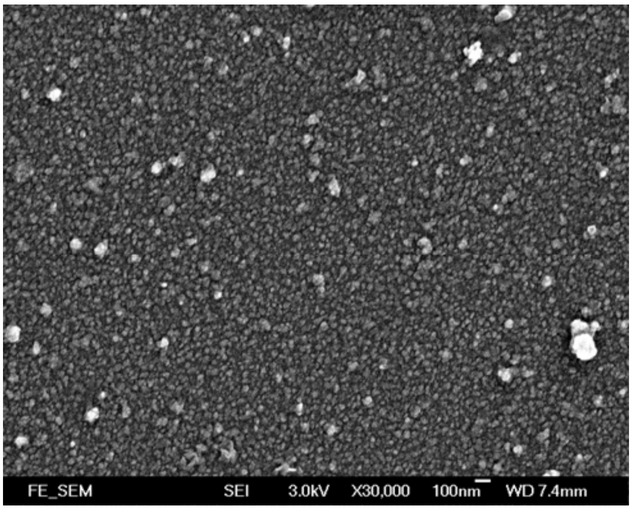

Figure 3.7 A higher magnification image of Co-PTFE composite film (UV-PLD samples).

As shown in Fig. 3.8 and Fig. 3.10, the SEM pictures reveal that both IR-PLD and UV-PLD Co-PTFE composite films consist of a PTFE matrix in form of a well connected porous network. The sizes of the polymer voids are ranged from few nanometers to several hundred nanometers. It can be inferred that the polymer deposited by PLD formed a more or less continuous but porous network, several nano-sized cobalt particles and/or some large PTFE particulates are embedded in the voids of the PTFE network. Cobalt particles are thus separated by the PTFE barriers. From the SEM pictures, the estimated thickness of the barriers should be less than 10 nm.

However, as shown in Fig. 3.9 and Fig. 3.11, comparatively smaller polymer voids can be seen at the HCl etched boundary, which were not as large as fully etched region. This may be due to the polymer structural deformation and relaxation after the metal phase was entirely removed. Therefore, the actual polymer voids in the network and the nano-sized cobalt particles embedded inside may be even smaller.

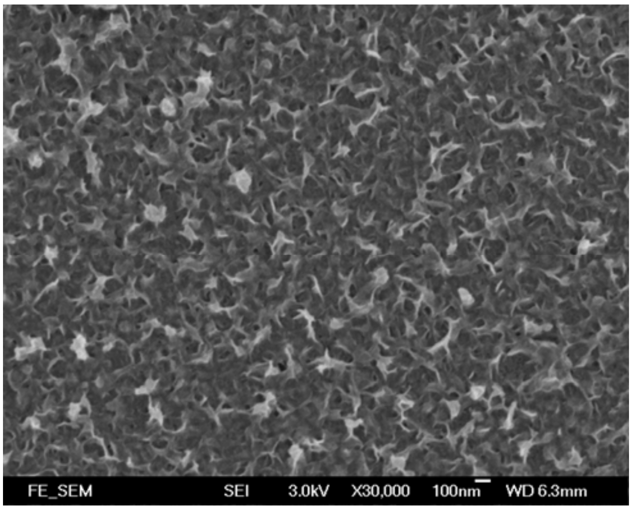

Figure 3.8 **SEM image of Co-PTFE composite film after etching with 0.1M HCl (IR-PLD samples).**

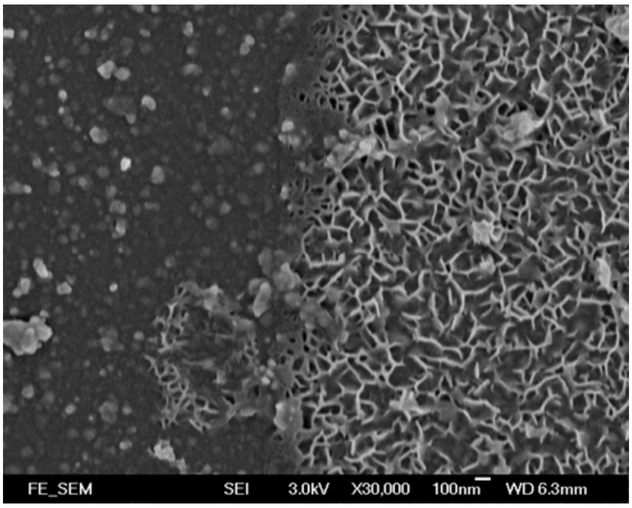

Figure 3.9 **SEM image of Co-PTFE composite film at the etched boundary (IR-PLD samples).**

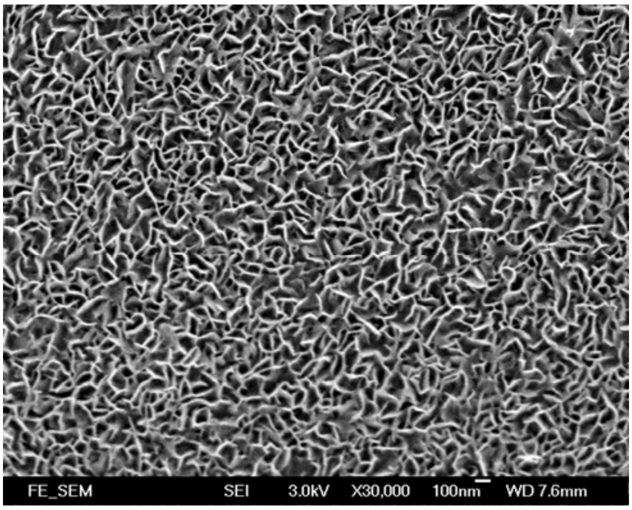

Figure 3.10 SEM image of Co-PTFE composite film after etching with 0.1M HCl (UV-PLD samples).

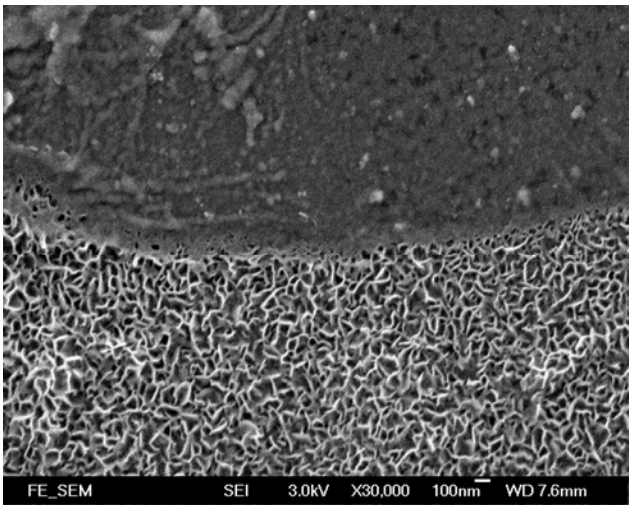

Figure 3.11 SEM image of Co-PTFE composite film at the etched boundary (UV-PLD samples).

3.4 Microstructure Characterization by TEM

In order to investigate the cobalt particle size, Co-PTFE composite film was deposited on carbon-coated copper grid directly by PLD for 7 min. A shorter deposition time was used for preparing thin enough sample for TEM investigation, and therefore, the particles distribution inside the sample may be different from the samples used for electrical measurement. As shown in Fig. 3.12 (a), cobalt particles, (represent in dark color) are located separately with some material forming a barrier in between (represent in white color). A clearer image can be seen in Fig. 3.12 (b), which reveals the Co particle diameter in a range of about 3 - 5 nm. The barrier has a thickness of about 1 - 2 nm, which is thin enough for tunneling to occur. A bad crystallinity is observed for the particles which may due to the fact that the PLD process is performed at room temperature, such that the growth of well-crystalline materials are inhibited.

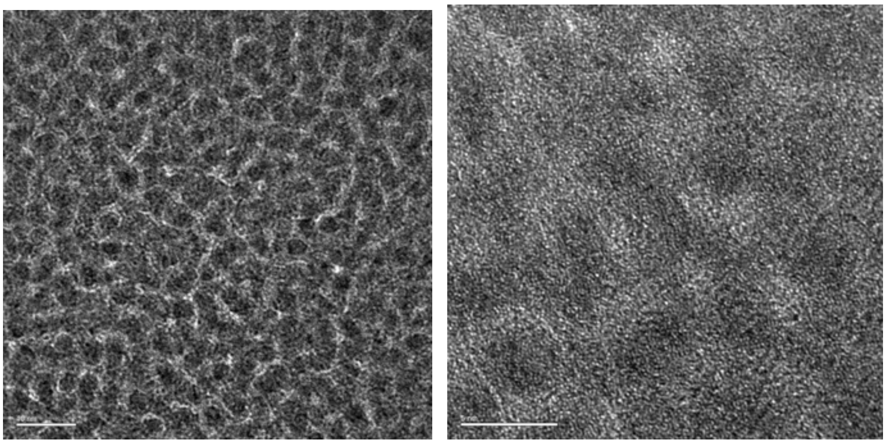

(a) **(b)**

Figure 3.12 (a) TEM image of Co-PTFE composite film deposited on carbon-coated copper grid for 7 min (UV-PLD samples) (b) High Resolution TEM image.

3.5 Temperature Dependence of Resistance of Co-PTFE Composite Films

Fig. 3.13 and Fig. 3.14 show the temperature dependence of the resistance of Cobalt-PTFE composite films (IR-PLD and UV-PLD samples) at zero applied magnetic field. As shown in the graphs, the resistance of both kinds of sample decreases nonlinearly when the temperature increase. It suggests a tunneling conduction mechanism.

The tunneling conductivity for granular metals embedded in insulator has been studied by Sheng et al. [Sheng 1973, Helman 1976]. They suggested a functional form for the temperature dependence of resistance R:

$$\ln R = 2(C/\mathrm{k_B}T)^{1/2} + \text{constant}, \qquad \text{(Eq. 3.5.1)}$$

where $C = (2\pi/h)(2m\phi)^{1/2}\, sE_c$, was the tunnel activation energy, in which ϕ is the effective barrier height, s is the separation between metallic granules (tunnel-barrier thickness), and E_c is the charging energy of a metallic granule.

As shown in the inset of Fig. 3.14, the plot of ln$R$ against $T^{-1/2}$ reveals a linear relationship. This result of the UV-PLD samples suggests the tunneling of electrons between Cobalt granules through the PTFE barriers. However, for the IR-PLD samples, as shown in the inset of Fig. 3.13, the plot of ln$R$ against $T^{-1/2}$ maintains a linear relationship until about 40 K, then it becomes non-linearly. This is the most significant difference that can be found when comparing the IR-PLD and UV-PLD samples prepared by using different wavelength. The result denotes that electron transport mechanism other than tunneling may occur inside the sample at temperature below 40K. Electron scattering by impurities, carbonization of the polymer due to the high laser fluence used and metallic conducting paths formed by incomplete isolation of individual cobalt granules may contribute to this result.

From the gradient of the plot of ln*R* against $T^{-1/2}$, as shown in the inset of Fig. 3.14, C is estimated to be 17 meV for the UV-PLD sample.

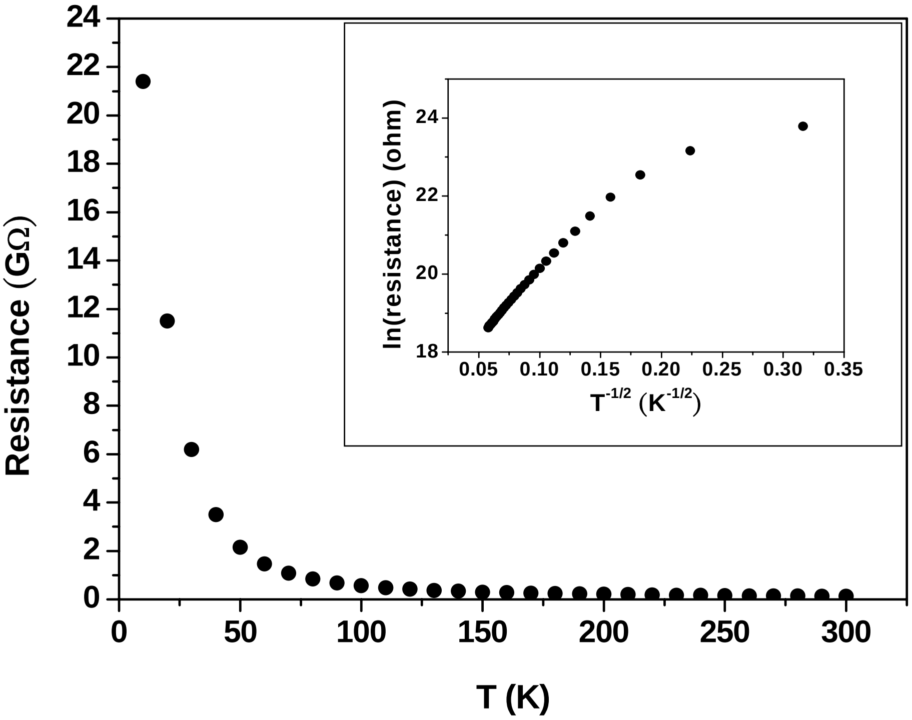

Figure 3.13 **Temperature dependence of the resistance of Cobalt-PTFE composite film. The inset is a plot of ln*R* against $T^{-1/2}$ (IR-PLD samples).**

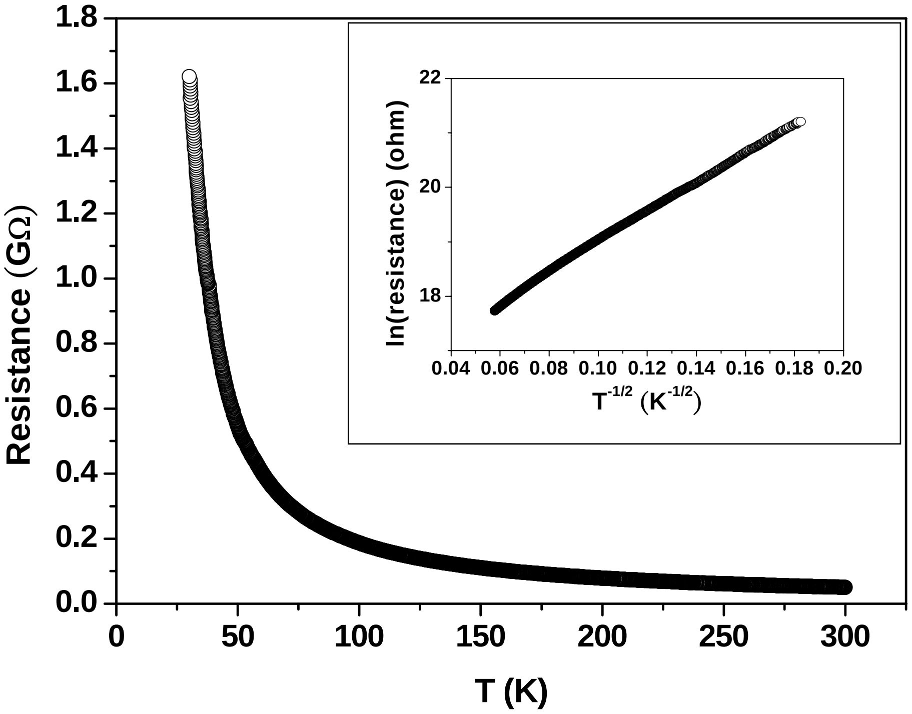

Figure 3.14 **Temperature dependence of the resistance of Cobalt-PTFE composite film. The inset is a plot of ln*R* against $T^{-1/2}$ (UV-PLD sample A).**

3.6 Magnetic Properties of Co-PTFE Composite Films

Fig. 3.15 (a) and (b) show the magnetization curves of the composite film (IR-PLD samples) measured at 300K and at 10K, respectively, using the vibrating sample magnetometer (VSM) equipped with a closed cycle liquid helium cryogenic chamber. At 300K, the magnetization curve is a hysteresis-type of nearly zero coercive field, whereas it shows a significant coercive field at low temperature. This characteristic reveals that the composite film exhibits superparamagnetic nature, as a result of its nano-sized cobalt particles content [McHenry 1994, Chen 1995, Batlle 2002]. At room temperature, the thermal energy is large enough to randomize the magnetic moments of the nano-sized particle, so the particles have a very small or nearly zero coercive field. However, at low enough temperature, the ferromagnetic state of the particles does not disturb by the thermal energy, therefore, the sample shows a significantly large coercive field again. From the magnetization curve, the coercive field of this composite film is about 590 Oe at 10K.

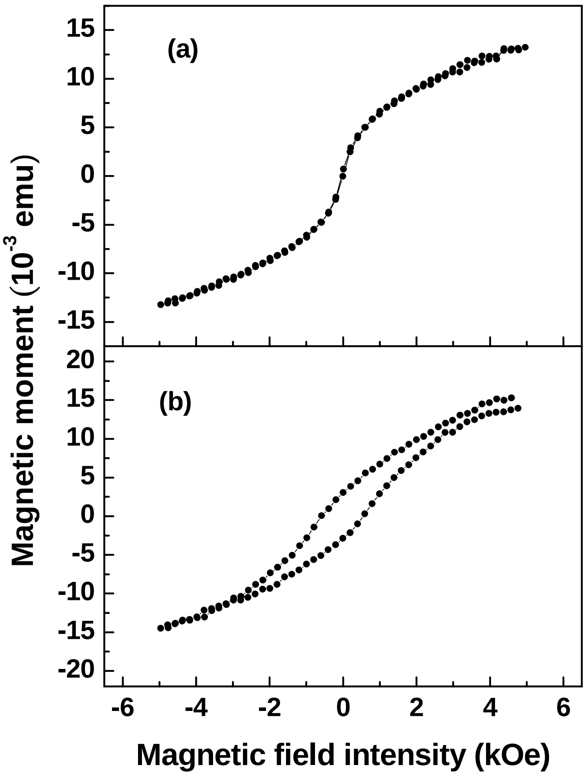

Figure 3.15 **Magnetization curves of Cobalt-PTFE composite film (IR-PLD samples) measured at (a) 300K and (b) 10K**

Since the signal of the prepared UV-PLD samples is too weak for the VSM measurement, the magnetic properties of this sample were measured using a SQUID magnetometer (Quantum Design). Fig. 3.16 shows the two magnetization curves (a) and (b) of the composite film (UV-PLD sample A) measured at 300K and at 20K, respectively. As shown in the graph, the coercivity of the hysteresis loop at 20K was quite obvious compared with the hysteresis of nearly zero coercive field at 300K, which reveals again the superparamagnetic nature of the nano-sized cobalt particles in the composite film. The magnetic moment of the composite film are increased at low temperature and does not reach saturation even at 10kOe. This result may be due to the superparamagnetic relaxation, indicating a transition from superparamagnetic to ferromagnetic behavior [Chen 1995]. The coercive field of this composite film obtained from the curve is about 430 Oe at 20K.

According to the theory of superparamagnetism, the magnetic moments of the nanoparticles are more easily to align along the applied magnetic field above a temperature named "blocking temperature (T_B)". Therefore, the curve of magnetic moments versus applied magnetic field would have no hysteresis effect measured above T_B and the magnetic particles are said to be in the superparamagnetic state. In the superparamagnetic state, the magnetization (M) of a system consisting of nanoparticles is described by the standard Langevin function:

$$M = M_o \left[\coth (\mu H/k_B T) - (k_B T/\mu H) \right],$$

which is equivalent to:

$$\mu = \mu_s \left[\coth (\mu_p H/k_B T) - (k_B T/\mu_p H) \right],$$

where μ is the measured total magnetic moments of the system at an applied magnetic field H, μ_s is the measured total magnetic moment of the system at saturation, μ_p is the magnetic moment of one nanoparticle and k_B is the Boltzmann constant.

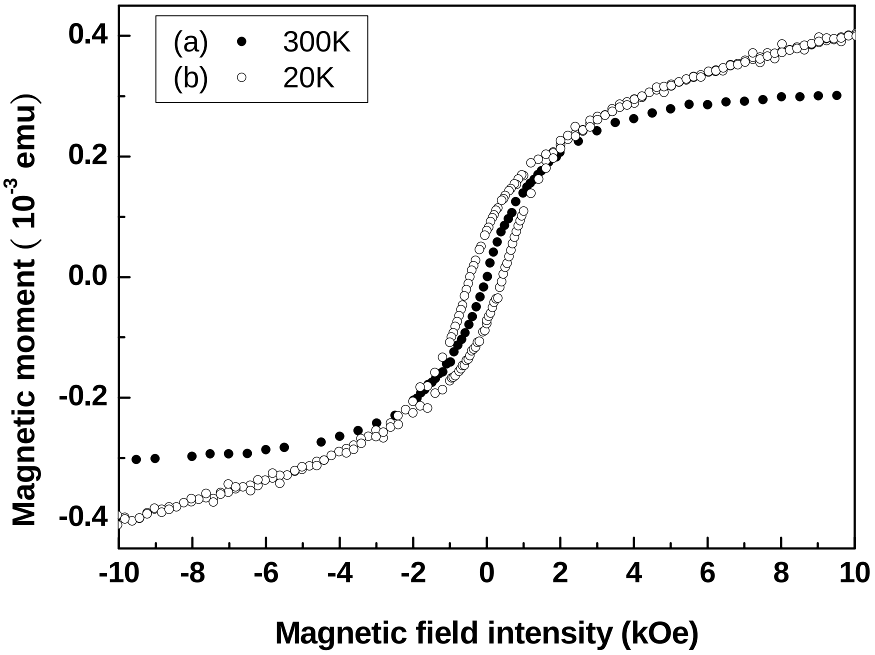

Figure 3.16 **Magnetization curves of Cobalt-PTFE composite film (UV-PLD sample A) measured at (a) 300K and (b) 20K, both with in-plane measurement.**

In order to obtain a more detail study of the UV-PLD composite film, Langevin function is used to fit the magnetization curve of the UV-PLD sample A measured at 300K, as shown in Fig. 3.17. From the graph, the Langevin fitting shows a good agreement of the experimental data.

From the fitting parameter, the total magnetic moment of the composite film (μ_s) at saturation is about 3.24 x 10^{-4} emu. The magnetic moment of one Co nanoparticle (μ_p) is about 6400 μ_B, where μ_B is the Bohr magneton.

According to some experimental value reported, the possible magnetic moment of one Co atom is ranged from 1.6μ_B to 2.1μ_B (μ_{Co} = 1.6 - 1.7μ_B for bcc, fcc and hcp crystalline structures), depending on the size of the Co nanoparticle, and the surface effect at the interface of the Co nanoparticle and the material surrounding it such as surfactant or a polymer matrix [Respaud 1998]. Therefore, it is reasonable to use these reported values to estimate the number of Co atoms in one Co nanoparticle. It is found that in the samples prepared each Co nanoparticle contains about 3000 - 4000 Co atoms.

Using the metallic radius of one Co atom, which is equal to 0.126 nm, it is found that the average diameter of the Co nanoparticle in this composite film is around 3.6 - 4 nm, which is quite consistent with the value obtained from TEM.

It should be noted that this is an average value among all the nanoparticles, two approximations have been taken in the standard Langevin model: the shape of each nanoparticle is assumed to be perfectly spherical and the particle size distribution follow a linear-logarithmic size distribution reported in most real systems [Batlle 2002]. In any case, the estimated particle size produces no contradiction to the superparamagnetic effect observed in our experimental results since it is below the critical diameter of the single domain size, which is ~ 20 nm for Co particles based on the domain theory [Gong 1991, Batlle 2002].

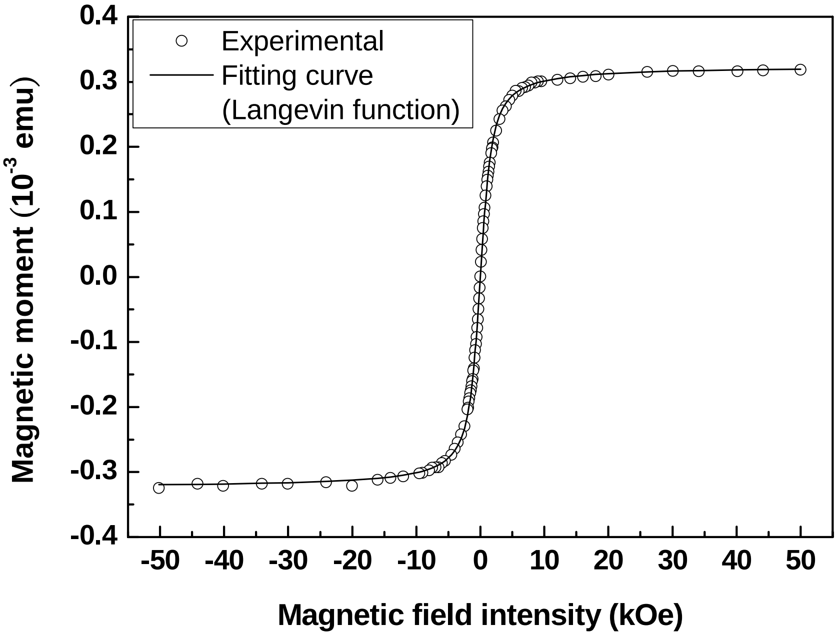

Figure 3.17 **Magnetization curve of Cobalt-PTFE composite film (UV-PLD sample A) with Langevin fitting at 300K, with in-plane measurement.**

In Fig. 3.18, curves (a) and (b) show the field cooled (FC) and zero field cooled (ZFC) magnetization as a function of temperature of the Cobalt-PTFE composite film (UV-PLD sample A) respectively. For the ZFC magnetization, the sample was firstly cooled to 5 K in the absence of magnetic field, and then a field of 50 Oe was applied and the magnetization was measured as the sample was heated up to 300 K. The FC magnetization was measured by cooling the sample to 5 K in the presence of 50 Oe magnetic field and then taking the measurement while heating up the sample to 300 K.

It can be seen in the figure that the ZFC and FC curves start to diverge from each other at 200K, the point of irreversibility. Below this temperature, the magnetization of ZFC curve reaches a maximum and then decreases again, while the magnetization of the FC curve keeps on increasing without a peak.

Indeed, magnetization curves for nano-sized magnetic particles as a function of temperature reveal a typical characteristic of superparamagnetism, in which the ZFC curve exhibits a peak temperature, named “blocking temperature (T_B)”. An analysis of the magnetic behavior in the ZFC condition for fine nanoparticles has been discussed by Bitoh et al [Bitoh 1996]. Consider a system of magnetic single domain or superparamagnetic particles, having the same volume and uniaxial magnetic anisotropy with zero applied magnetic field and at a temperature below the blocking temperature. The magnetic moment of each particle lies along their easy axis. The easy axes of the particles are randomly oriented and therefore the net magnetization for the system is zero. If a small external magnetic field is applied, the magnetic moment for each particle will lie along the easy axis with minimized free energy.

The system is said to be in a “blocked state”. When the temperature is increased above the blocking temperature, thermal energy is large enough to help the particle to overcome the energy barrier for rapidly switching the magnetic moment in between the easy axis direction and the opposite direction. Therefore, after integrating the component of the magnetization along the field direction for all particle orientations, the overall magnetization of the system will decrease continuously as the temperature is increasing above T_B.

The ZFC and FC curves shown in Fig. 3.18 can be explained by the above theory. Ideally, the blocking temperature and the temperature at which ZFC and FC curves start to diverge from each other should be nearly the same. The large difference in these two temperatures observed is attributed to the size distribution of the nanoparticles, and correspondingly, a large spread in the blocking temperatures. From the graph, the average blocking temperature (T_B) is estimated to be ~ 90 K.

Another interesting feature shown in Fig. 3.18 appears in the low temperature regime. Normally, for many magnetic nanoparticles systems, the ZFC magnetization will decrease below $\mathrm{T_B}$ down to the lowest temperature. It can be seen in Fig. 3.18 that there is an unusual increase of magnetization below 30 K. One of the possible reasons is that the result is attributed to those very small size nanoparticles, which behave paramagnetically even at very low temperature.

Another possible reason is the presence of some antiferromagnetic (AFM) nanoparticles in the composite film. A similar enhancement of magnetization below the Neel temperature (T_N) has been observed in some AFM nanoparticles system [Makhlouf 2002, Bhowmik 2007]. The observed temperature for this unusual behavior is about 30K, which is close to the Neel temperature of bulk Co_3O_4. This cobalt oxide is antiferromagnetic with spinnel structure. It is possible for the nanosized cobalt be oxidized during the PLD process or after the sample preparation. The exposure of these Co nanoparticles in the air for a long time may lead to the formation of cobalt oxides including the Co_3O_4, as a result contributing to this unusual magnetization behavior.

In addition, Gubin et al. had reported that the formation of Co nanoparticls on the surface of PTFE would induce a sharp enhancement of magnetization [Gubin 2005]. They claimed that it should be due to the perpendicular magnetic susceptibility significant grows below the Neel temperature (~38 K). However, the mechanism of the enhancement is still not fully understood.

More experiments need to be done in order to clarify the unusual behavior observed below 30K. However, the general trend observed in the ZFC and FC curves, the hysteresis obtained at 20 K and the Langevin fiting all confirm that our system consist of magnetic Co nanoparticles with size small enough to behave superparamagnetically with a T_B of about 90 K.

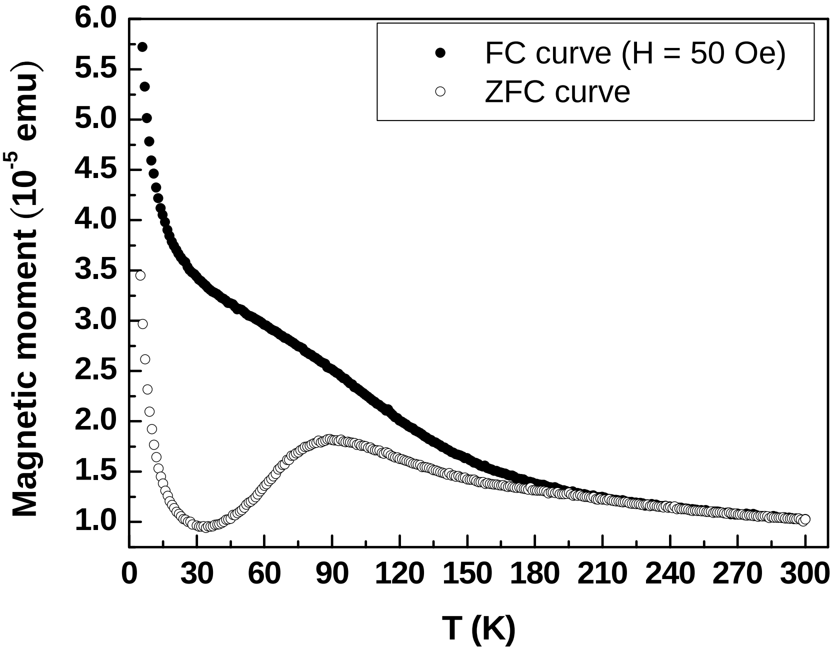

Figure 3.18 (a) FC and (b) ZFC magnetization as a function of temperature of Cobalt-PTFE composite film (UV-PLD sample A), with in-plane measurement.

3.7 Room Temperature Magnetoresistance of Co-PTFE Composite Films

Other than the interesting magnetization properties of the Co-PTFE composite films, they also exhibit significant magnetoresistance effect. The DC resistance of the samples placed in a magnetic field will be decreased. The larger is the applied magnetic field, the lower the resistance of the samples. Fig. 3.19 shows the effect of applied magnetic field on the resistance of one of the IR-PLD samples. The magnetoresistance shown is the relative change of resistance and is defined as $MR = \frac{R(H) - R(H_o)}{R(H_o)}$, where H and H_0 being the applied magnetic field and the magnetic field of maximum resistance, respectively. These results were measured with H perpendicular to the film surface at room temperature. As shown in the graph, the Cobalt-PTFE composite film exhibits a 5% change of MR at an applied field of 10kOe at room temperature, which is the largest MR% obtained among all the IR-PLD and UV-PLD samples. It should be noted that the MR has not reached saturation at 10kOe, which implies a larger value of MR could be achieved at a higher magnetic field.

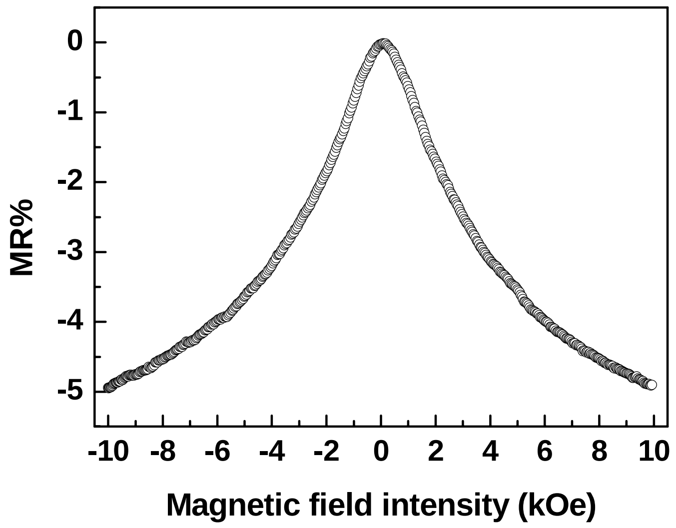

Figure 3.19 **Magnetic field dependence of the magnetoresistance of the Cobalt-PTFE composite film (IR-PLD samples), with out-of-plane measurement.**

Both the IR-PLD and UV-PLD samples reveals a negative MR effect as shown in Fig. 3.20 and 3.21, which denotes the resistance of the sample was decreased with an increase in magnetic field. A negative MR effect has also been observed in most of the oxide based granular films [Fujimori 1995].

The effect of applied magnetic field on the magnetoresistance change of the IR-PLD and UV-PLD samples, at out-of-plane and in-plane measurement, is shown in Fig. 3.20 and 3.21 respectively. The Cobalt-PTFE composite film (UV-PLD sample A) exhibits about 4% change in MR at an applied field of 8 kOe at room temperature. It can be seen that a difference in out-of-plane and in-plane measurement of the MR profiles exhibit for both kinds of samples. The difference is mainly due to the demagnetization field generated inside the sample. The magnitude of the demagnetization field is related to the geometry of the sample and the direction of the applied magnetic field. The applied field parallel to the film surface with distant edges, which corresponds to the in-plane measurement, produces a weak demagnetization field. On the other hand, the demagnetization field is stronger when the magnetic field is applied perpendicularly to the film surface, which corresponds to the out-of-plane measurement. Thus a larger external magnetic field is needed in order to produce the same magnitude of internal field compared with the in-plane configuration. Therefore, the in-plane MR profile shows a more sharp change at low field. As the field increases the magnetization of cobalt particles approach saturation, the demagnetization field becomes of the same magnitude at both configuration of measurement, thus the MR profiles merge together at high field.

The origin of the MR in the Cobalt-PTFE granular composite film can be interpreted by the “spin-dependent tunneling” mechanism [Tedrow 1973, Julliere 1975, Mitani 1997]. At room temperature, the magnetic moment of the cobalt nanoparticles, which are in superparametic state, fluctuates between the directions of the anisotropic easy-axes due to the thermal excitation, such that the magnetic moments of the cobalt nanoparticles are randomly oriented in the Cobalt-PTFE granular composite film. When an external magnetic field is applied, the magnetic moments of the cobalt particles tend to align in parallel with the field direction. Consequently, the resistance of the film decreases as a function of the applied magnetic field, because the probability of electron tunneling process increases when the magnetization of the cobalt particles are in parallel state.

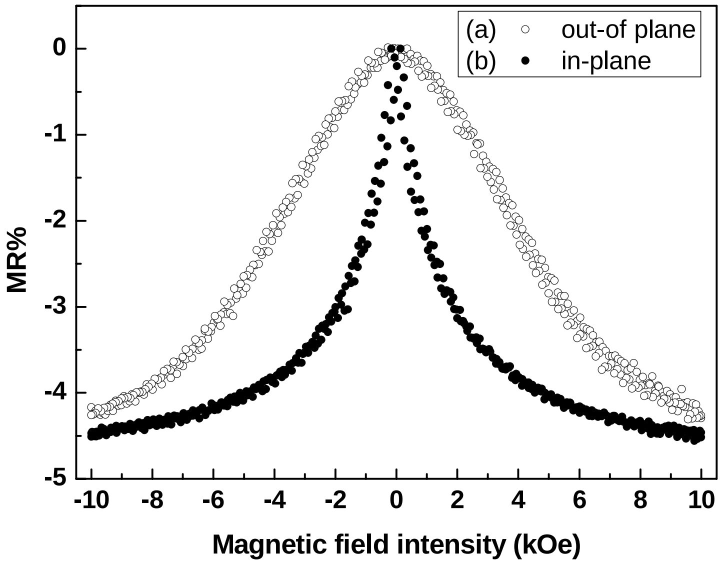

Figure 3.20 **Magnetic field dependence of the magnetoresistance of the Cobalt-PTFE composite film (IR-PLD samples) with (a) out-of-plane measurement and (b) in-plane measurement.**

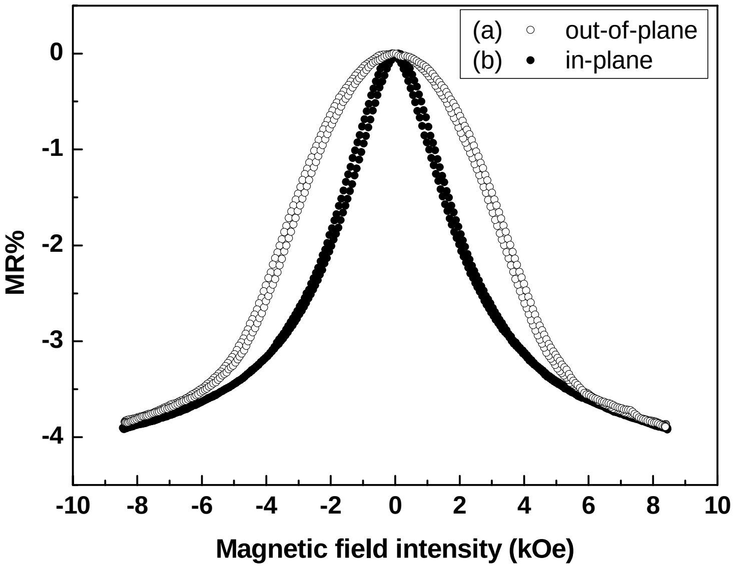

Figure 3.21 **Magnetic field dependence of the magnetoresistance of the Cobalt-PTFE composite film (UV-PLD sample A) with (a) out-of-plane measurement and (b) in-plane measurement.**

According to J. Inoue and S. Maekawa, the tunneling magnetoresistance (TMR) of nano-granular films in superparamagnetic state can be expressed by the following equation [Inoue 1996]:

$$\mathrm{TMR} = P^2m^2 / (1 + P^2m^2), \qquad \text{(Eq. 3.7.1)}$$

where P is the spin polarization of cobalt tunneling electrons and m (= $M(H)/M_\mathrm{s}$) is the reduced magnetization of the system and M_s is the saturation magnetization. The Langevin fitting magnetization given in Fig. 3.17 was used to calculate the reduced magnetization for the present evaluation. Equation 3.7.1 thus can be used to fit the measured MR data. The result is shown in Fig. 3.22. From the graph, it can be seen that the fitting curve with spin polarization P = 0.22 is in good agreement with the experimental data. However, some reported values are 0.35 or 0.42 but the theoretical P value for cobalt is 0.33 [Stearns 1977, Meservey 1994, Soulen 1998]. Here, the small P value obtained from the fitting could be originated from the following reasons: As suggested by Slonczewski, the material of the insulating matrix (PTFE in our case) may need to be considered in determining the actual P value of the ferromagnetic metal in a composite system [Slonczewski 1989], which is unknown at the mean time. Moreover, as Tsymbal and Pettifor predicted, the spin polarization can be decreased with increasing disorder for tunneling through a barrier containing defects [Tsymbal 1999]. Since the creation of carbon particles due to polymer degradation in the PLD process is possible, polymer of amorphous phase and the incorporation of amorphous carbon in the polymer may lead to a more disordered barrier, thus lowering the P value.

Spin-dependent tunneling from clean and oxidized cobalt surfaces have been studied by Belashchenko et al [Belashchenko 2004]. According to their results, oxidized cobalt surface can create a strong spin-filter effect, which strongly suppresses the tunneling of those minority-spin states that dominated the conductance for the clean Co surface, and making the conductance almost 100% positively spin-polarized ($P \approx 1$) . Putting this P value into the equation, the calculated TMR% will become too large which greatly deviate from the experimental result. Therefore, oxidation of the metal nanoparticles surface may not be considered.

Indeed, spin flipping effect caused by the magnetic impurities located in the insulating matrix [Zhu 1999], which was neglected in the equation, may also suppress the TMR value. Since the appearing of some cobalt ions or very small cobalt clusters in the polymer matrix during PLD process is not really impossible. Incomplete isolation of individual nanoparticles in the matrix which deviates from the ideal model, magnetic interaction between nanoparticles which was neglected in the equation, may also be the possible factors. In fact, temperature dependence of spin polarization may also be an important factor [Lyu 1999].

Nevertheless, the above results confirm that the magnetoresistance of cobalt-PTFE system can be explained by the "spin-dependent tunneling" theory, which is common in many nano-granular systems.

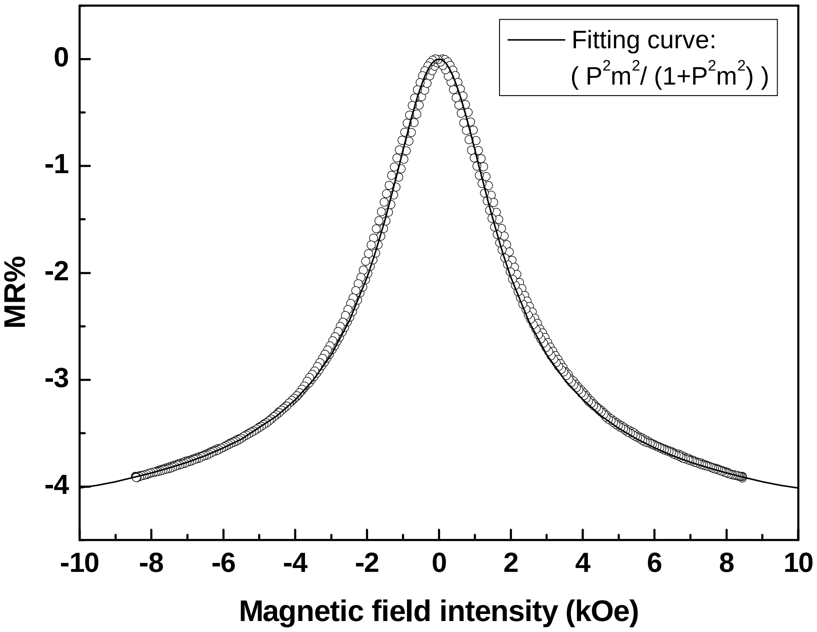

Figure 3.22 **Magnetic field dependence of the magnetoresistance of the Cobalt-PTFE composite film (UV-PLD sample A) with in-plane measurement. The solid line is the fit to equation: $P^2m^2/(1 + P^2m^2)$.**

3.8 Temperature Dependence of Magnetoresistance of Co-PTFE Composite Films

The curves (a) and (b) in Fig. 3.23 show the MR% profile of the IR-PLD samples measured at 300 K and 30 K respectively, both are the in-plane measurements. A significant enhancement of MR% was achieved at 30 K, to a value larger than 5% at 6 kOe, comparing with about 4% at room temperature. The profile is symmetric and still does not reach saturation even at 30 K. Split of the MR% profile peaks become obvious at 30 K. The splitting is resulted from the measurement when the direction of the magnetic field is applied oppositely. However, direct comparison between the MR loop splitting and the M-H hysteresis loop is not possible here. The origin of the MR enhancement at low temperature and the MR loop splitting will be explained in the following.

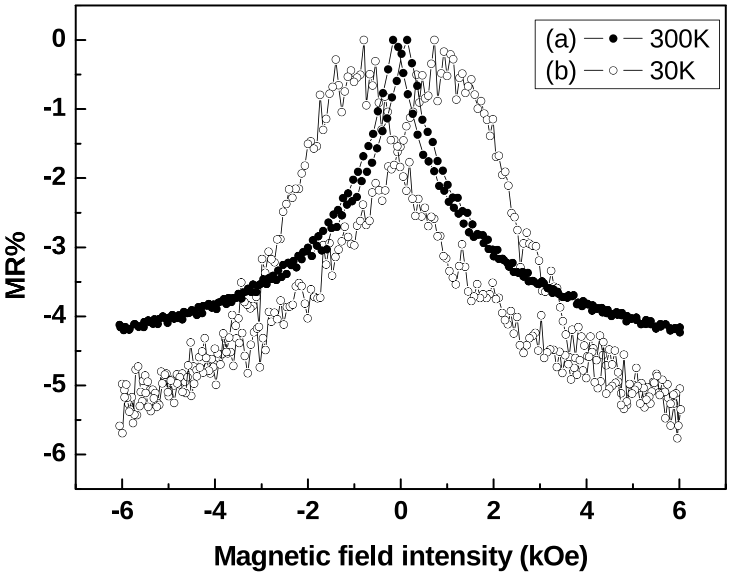

Figure 3.23 Magnetic field dependence of the magnetoresistance of the Cobalt-PTFE composite film (IR-PLD samples) measured at (a) 300 K and (b) 30 K, both are with in-plane measurement.

The curves (a) and (b) as shown in Fig. 3.24 give the MR profile of the Cobalt-PTFE composite film (UV-PLD sample A) measured at 300 K and 20 K respectively, while both are in-plane measurement. A significant enhancement of MR value to 6% was achieved at 20 K at 8 kOe. The MR profile at 20 K is symmetric and still does not reach saturation at 8 kOe, which exhibits a significant hysteresis compared with the room temperature profile.

The shifting of the MR profile at low temperature can be interpreted by the superparamagnetism of the cobalt nanoparticles in the composite film. At room temperature, the thermal energy is large enough to randomize the magnetic moments of the nano-sized particle, so the particles have a very small coercive field. However, at low enough temperature, the particles regain their ferromagnetic state which shows a significantly large coercive field below the blocking temperature (T_B). In fact, T_B depends on both the particles size and the applied magnetic field [Zhang 1998]. Since the energy barrier $E(H)$ is related to applied magnetic field H as $E(H) = E_o(1 - \frac{H}{H'})^{\alpha}$ where E_o is the energy barrier at zero field and H' is the field required to switch the magnetization of the particles. In general, the superparamagnetic regime would shift to lower temperatures at a stronger applied magnetic field or for smaller particles [Chen 1995, Respaud 1998, Batlle 2002]. A non-zero magnetic field is needed in order to oppose the coercive field of the cobalt particles in the sample and bring the sample to the highest resistance state with highest degree of disorder in magnetic moments, resulting in the shifting of the MR profile.

The two peaks of the profile within a complete magnetic cycle, as shown in Fig.

3.24, are located at ±750 Oe which should correspond to the coercive field of the cobalt particles at 20K. This value is too large when comparing with the coercive field (~430 Oe) obtained in the M-H measurement, as shown in Fig. 3.16. In addition, as shown in Fig. 3.24, a magnetic field of 8 kOe is still not enough to produce the overlapping MR curves at low temperature, while the M-H curves is about to overlap at a field of about 4 kOe.

Just like most of the nanogranular systems, the characteristic features of the MR and the M-H hysteresis loop should be consistent. In fact, the MR profile and the M-H profile are measuring in two different experimental setups. A slight misalignment between the sample plane and the applied magnetic field could contribute to this result. Moreover, as shown in the FC and ZFC curve, there exists some strange behavior in the sample below 30 K which may also be found in the MR measurement at 20 K. Although the mechanism behind is not fully known at the moment, an enhancement of the MR% is clearly observed at 20 K and can be explained by the temperature dependence of spin-dependent tunneling and the superparamagnetic relaxation.

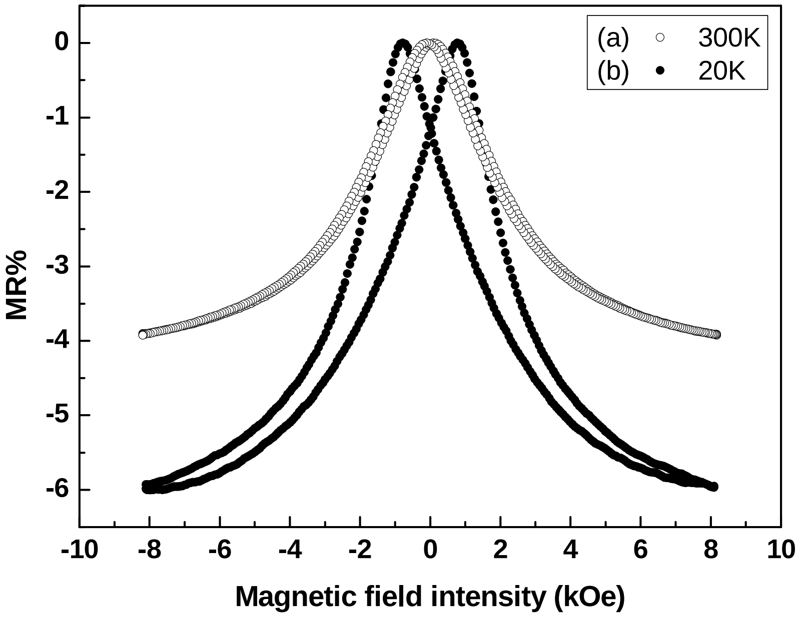

Figure 3.24 **Magnetic field dependence of the magnetoresistance of the Cobalt-PTFE composite film (UV-PLD sample A) measured at (a) 300 K and (b) 20 K, both are with in-plane measurement.**

A plot of the separation of the peaks, i.e. twice of the coercive field from 20 K to 300 K is given in Fig. 3.25. It shows that the peak separation is about 200 Oe at 300 K, which refers to a coercive field of about 100 Oe of the composite film. The non-zero coercive field may be due to the offset of the hall probe sensor used in the measurement, the coercive field should be close to zero which will be consistent to the magnetization curve at 300 K. The peak separation does not change much from 300 K to around 100 K. Below this temperature, the peak separation starts to increase. With a further decrease in temperature of the sample, the separation increases further to a value of ~ 1.6 kOe at 20 K. The increase of the coercive field above a transition temperature should correspond to the changing from the paramagnetic state to the ferromagnetic state of the cobalt nanoparticles. This transition temperature, which should correspond to the blocking temperature (T_B), is ~ 100 K from the graph. This blocking temperature obtained from the MR measurement agrees well with the one obtained from the ZFC and FC magnetization measurement with a difference of only 10 K. In fact, Fujimori et al. have reported that the Co grains behave as superparamagnets above ~ 100 K [Fujimori 1995]. This result further verifies that our Co-PTFE samples consist of nano-sized cobalt particles exhibiting a superparamagnetic nature and becomes ferromagnetic which contribute to the splitting of the MR curve at low temperature.

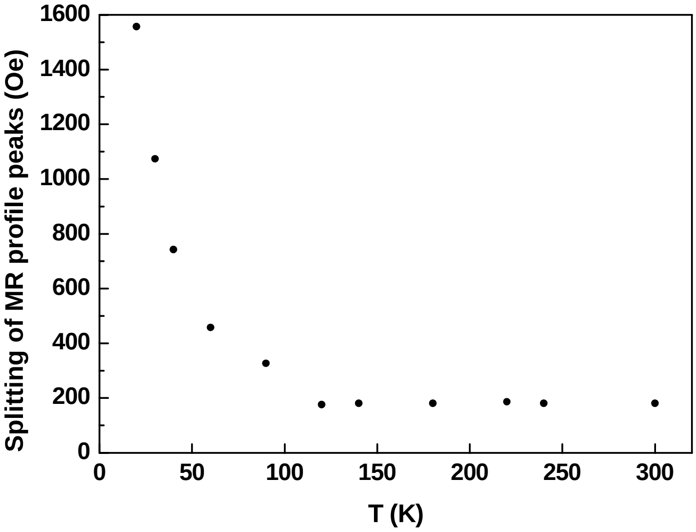

Figure 3.25 **Temperature dependence of the separations of the MR peaks at a temperature range from 20 K to 300 K (UV-PLD sample A).**

Fig. 3.26 shows the temperature dependence of MR values of two different Cobalt-PTFE composite films (UV-PLD samples) fabricated by using different laser pulse ratio, measured at 8 kOe. Sample A (corresponding to UV-PLD sample A) and B were fabricated with the Cobalt:PTFE laser pulse ratio of 30:2 and 34:2, respectively. Although the MR values at room temperature of the two samples are different, they show similar temperature dependence. The MR values measured at 8 kOe of both samples increase steadily from 300 K to about 60 K, followed by a steeper increase of MR with a further decrease in temperature.

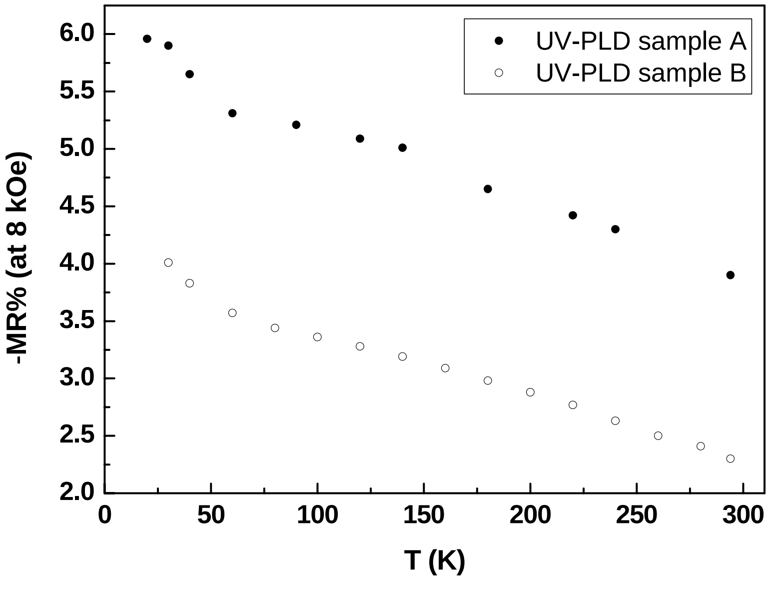

Figure 3.26 **Temperature dependence of MR of two Cobalt-PTFE composite films (UV-PLD samples) fabricated by different laser pulse ratio of cobalt and PTFE, measured at the applied magnetic field of 8 kOe, with in-plane measurement.**

According to the Eq. 3.7.1 describing the tunneling magnetoresistance of nano-granular systems, the MR value approaches $P^2/(1 + P^2)$ at sufficiently high magnetic field. However, for small applied magnetic field, the reduced magnetization (m) will be temperature dependence. For superparamagnetic nanoparticles system, a phase transition from superparamagnetic to ferromagnetic state will occur at the blocking temperature (T_B). Therefore, the reduced magnetization and the MR value would decrease as the applied magnetic field is not large. From the experimental data obtained in the FC magnetization curve with 8 kOe and 15 kOe measuring field (which have not shown here), it can be found that the value m starts to decrease from ~200 K which indicates the system is changing to ferromagnetic state. From the fitting curve (dashed line) as shown in Fig. 3.27, a decreasing MR value is resulted after putting the m values into Eq. 3.7.1, with a spin polarization $P = 0.216$. Obviously, these fitting parameters cannot produce MR values that match the measured MR at low temperature for our system.

In fact, the contribution of temperature dependence of spin polarization (P) should not be neglected [Shang 1998, Lyu 1999, Moodera 1999, Chen 2001]. The values of P for various kinds of magnetic materials are determined from the tunneling measurement at low temperature ($T < 4.2$ K), with a superconductor acting as spin analyzer. Thus, it is reasonable that the value of P is only available at low temperature. Here, it is found that by considering a temperature dependence of P in Eq. 3.7.1 as shown in the inset in Fig. 3.27, the predicted curve (solid line) fit the experimental data above 60 K. The temperature dependence of P was determined by considering the spin polarization of cobalt as reported at low temperature ($P_{Co} = 0.42$)

and the *P* value used for the fitting in Fig. 3.22. Although the origin of this temperature dependence of *P* is still an unknown, it gives a good prediction of the MR values above 60 K. However, as seen in the graph, the predicted MR values become saturated and even decrease below 60 K, because the *P* value already reached the reported value. Therefore, other mechanism must contribute to the further increase of MR.

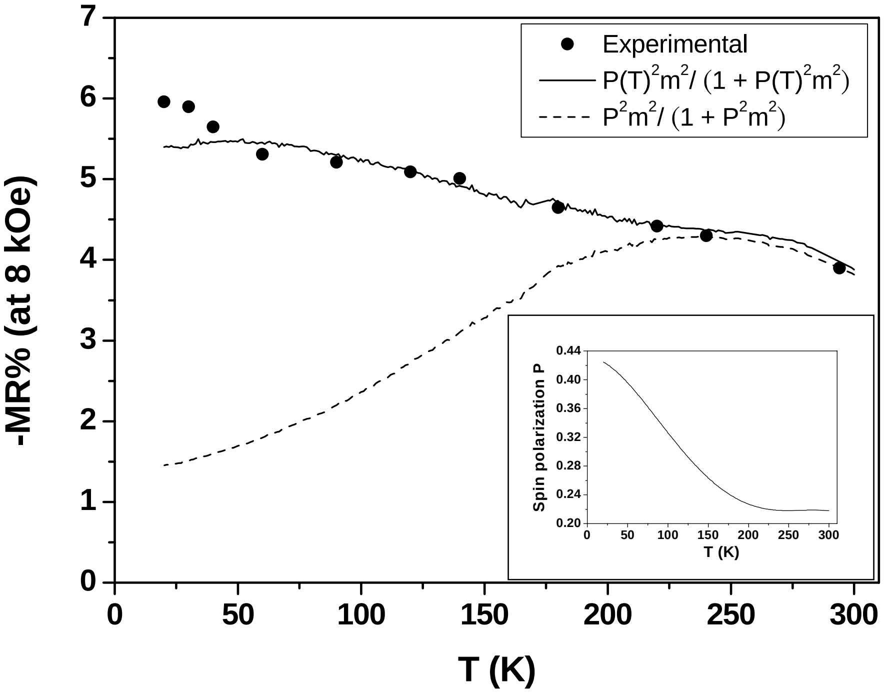

Figure 3.27 **Temperature dependence of MR of Cobalt-PTFE composite films (UV-PLD sample A) measured at the applied magnetic field of 8 kOe, with in-plane measurement. Dashed line represents the theoretical MR value given by the equation as shown, with *P* = 0.216. Solid line represents the calculated MR value in considering the temperature dependence of *P*, as shown in the inset.**

In fact, high values of MR observed at low temperature, which surpassed the upper limit of the theoretical expectation of Eq. 3.7.1, has been reported. Mitani et al. explained the large MR at low temperature by considering the tunneling process between granules with different sizes, which has not been considered in Eq. 3.7.1 [Mitani 1998]. A broad particle size distribution is an intrinsic property of many insulating granular systems. The larger the granule size is, the larger the separation of the granules, and therefore, there will be a number of smaller granules in between those larger one. For structure like this, the charging energy (E_c) or Coulomb blockade effect will become important. Assuming there are large granules with size n$<d>$ and charging energy $<E_c>$/n, which are separated by n smaller granules with average diameter $<d>$ and charging energy $<E_c>$ on a conduction path. The thermally activated charge carriers occupy mostly the large granule with probability proportional to the Boltzmann factor $\exp(-<E_c>/2nk_BT)$. The ordinary tunneling of an electron from the large granule to the small one increases the charging energy by $\Delta<E_c> \sim n<E_c>/2(n+1)$. At low enough temperature, the ordinary tunneling will be suppressed by the Coulomb blockade when thermal energy k_BT is smaller than $\Delta<E_c>$. In this regime, the higher-order tunneling processes will be dominant which the charge carriers are transferred between the large granules through the array of small ones using the simultaneous tunneling of (n+1) electrons. Finally, the conductivity σ can be estimated:

$$\sigma(T) \propto (1 + P^2m^2)\exp(-2\sqrt{2ksE_c/k_BT}), \qquad \text{(Eq. 3.8.1)}$$

where P is the spin polarization, m is the reduced magnetization, k is related to the effective tunnel-barrier height, s is the separation between metallic granules (tunnel-barrier thickness), and E_c is the charging energy of the metallic granule. In fact, the value ksE_c is the same as the constant C appearing in Eq. 3.5.1. The MR can then be expressed as:

$$\mathrm{MR} = 1 - (1 + P^2m^2)^{-(n^*+1)}, \qquad \text{(Eq. 3.8.2)}$$

where $n^* = (E_c/8ks\mathrm{k_B}T)^{1/2}$ with $\mathrm{k_B} = 1$.

According to Eq. 3.8.2, the values of ks and E_c can be found from the gradient of the plot of ln$R$ against $T^{-1/2}$, as shown in the inset of Fig. 3.14. It should be noted that by only considering the higher-order tunneling model resulted a decreasing trend of MR (not shown here) similar to the one predicted by Eq. 3.7.1. Therefore, here we put a temperature dependence of P into Eq. 3.8.2 as shown in the inset of Fig. 3.28. The temperature dependence of P used here is not the same as the one shown in Fig. 3.27. As shown in Fig. 3.28, the predicted curve (solid line) fit well with the experimental data even below 60 K, with $ks = 3$ and $E_c = 33$ be the fitting parameters.

The above fitting results infer that the MR enhancement at low temperature is due to the interplay of the superparamagnetic relaxation, normal and higher-order spin-dependent tunneling and the contribution of the temperature dependence of spin polarization. However, high applied magnetic field measurement may need to perform in order to give a clearer explanation.

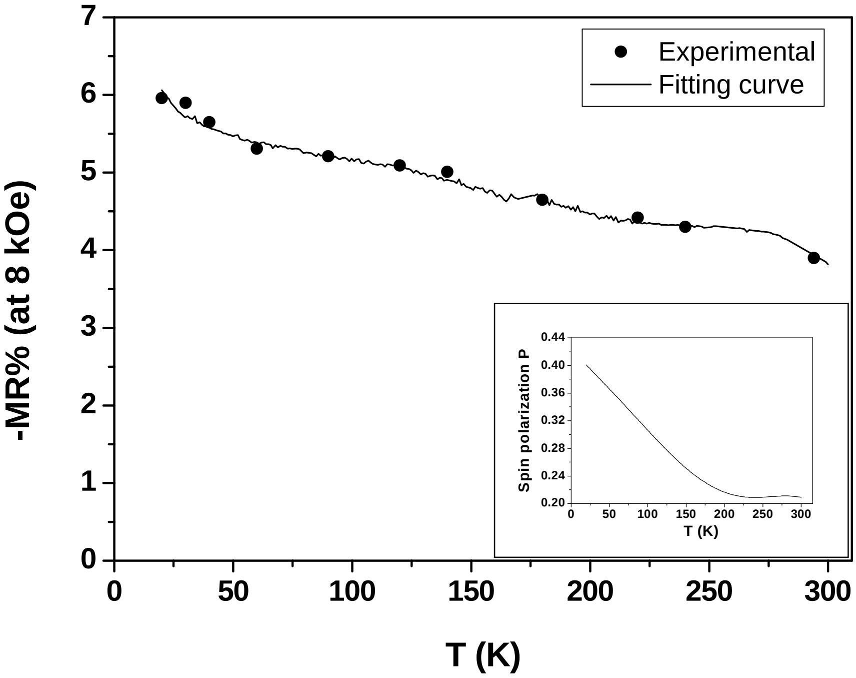

Figure 3.28 **Temperature dependence of MR of Cobalt-PTFE composite films (UV-PLD sample A) measured at the applied magnetic field of 8 kOe, with in-plane measurement. Solid line represents the calculated MR value using the higher-order tunneling model in considering the temperature dependence of *P*, as shown in the inset.**

3.9 Reproducibility of Resistance and Magnetoresistance

The reproducibility of the resistance and magnetoresistance of UV-PLD samples has been studied. Table 3.1 shows the resistance and magnetoresistance of 4 different samples prepared at same experimental conditions. A variation of at least one order of magnitude can be found in both resistance and magnetoresistance value. The difficulties of reproducing samples of similar resistance and MR are mainly attributed to the randomness of the laser deposition process. Target material, especially for polymer, may not be deposited uniformly such that the samples microstructure, such as the particles separation and the barrier thickness, may vary from sample to sample. These variations in sample microstructure are the main causes which lead to the difference of the resistance and magnetoresistance.

	Resistance (Ω)	Magnetoresistance (%)
1st sample	0.17 M	1.56
2nd sample	3.64 M	1.51
3rd sample	80 M	0.8
4th sample	5.47 M	0.5

Table 3.1 Resistance and Magnetoresistance of 4 different Cobalt-PTFE composite films (UV-PLD sample) prepared at same experimental conditions.

CHAPTER 4

Cobalt Nanoparticles produced by Laser Ablation of Cobalt Target in Liquid

4.1 Introduction

Nanosized materials have attracted much attention due to their interesting properties and potential applications in various areas such as optical and magnetic devices, chemical sensors [Kruis 1998, Wilcoxon 1998, Vaseashta 2005, Sun 2007, Tang 2007]. The technique for fabricating nanoparticles or nanostructured thin films is still a hot topic in both science and engineering's concerns. For obtaining pure nanoparticles used for further treatment, laser ablation of the bulk solid target both in vacuum and inert atmospheres has been reported [Sasaki 1998, Li 1999, Dureuil 2001, Happy 2006]. It is evident that this is a promising method to produce nanoparticles. However, agglomeration of the nanoparticles during the fabrication process and oxidation after exposing to oxygen environment gives limitation of this technique. Recently, a technique called "Pulsed Laser Ablation in Liquid" (PLAL) attracts attention as a new method to prepare nanoparticles. The pioneer work of PLAL was reported by Patil et al., in which a metastable phase of iron oxides was synthesized by ablating an iron target in water [Patil 1987]. After that, several groups had demonstrated that nanosized metal particles can be produced by laser ablating the metal targets settled in water or other liquids [Dolgaev 2002, Chen 2004, Tsuji

2005, Kawaguchi 2007]. It has also been shown that size control of the nanoparticles and formation of metal compounds is available by changing the ablation parameters, the choice of liquids or adding suitable organic surfactants [Mafune 2000, Simakin 2001, Mafune 2001, Liang 2004, Besner 2006].

Besides PLD technique, it is expected that PLAL is a feasible technique to prepare composite of nanosized particulate phase. Suitable polymer can be dissolved in the solvent that can be mixed with the nanoparticles prepared by PLAL, and subsequently using spin-coating technique or evaporating the solvent directly to obtain nanocomposite thin films. Magnetic nanocomposite thin films can also be fabricated by simply using a ferromagnetic metal target. In this chapter, we have reported some investigations on the PLAL technique utilizing cobalt as the metal target, settled in hexane, ethanol and toluene, to produce cobalt nanoparticles. The nanoparticles fabricated were then investigated by SEM and TEM. The success in producing nanosized cobalt particles in liquid demonstrates that this work is worth for further development.

4.2 Laser ablation in Hexane

Hexane was firstly chosen as the solvent in the PLAL process. Since very high temperature and pressure can be induced at the solid-liquid interface in the PLAL process [Fabbro 1990], any chemical reactions and oxidation could occur resulting in the formation of metal compounds or metal oxides rather than pure metal nanoparticles. Therefore, hexane may be a good choice since there are only hydrocarbon chains without any source of oxygen atoms. After ablation of the cobalt target in hexane, no color change of the solution was observed. Only a few black particles, which can be seen by naked eyes, can be attracted by a magnet. These black particles should be the ferromagnetic cobalt particles.

4.2.1 SEM Analysis

Fig. 4.1 (a) shows the SEM image of a drop of solution with those black particles, which has been well dispersed by an ultrasound, on a clean silicon wafer. It reveals the spherical particles of size ranging from 20 - 100 nm. No serious agglomeration of nanoparticles can be seen. However, only few areas with nanoparticles can be found on the silicon wafer which may due to the low yielding of this process. To further verify the result, a drop of the solution was put on a copper grid for SEM inspection. Fig. 4.1 (b) and (c) reveal a surface with nanoparticles of similar sizes as shown in Fig. 4.1 (a), but with more serious agglomeration.

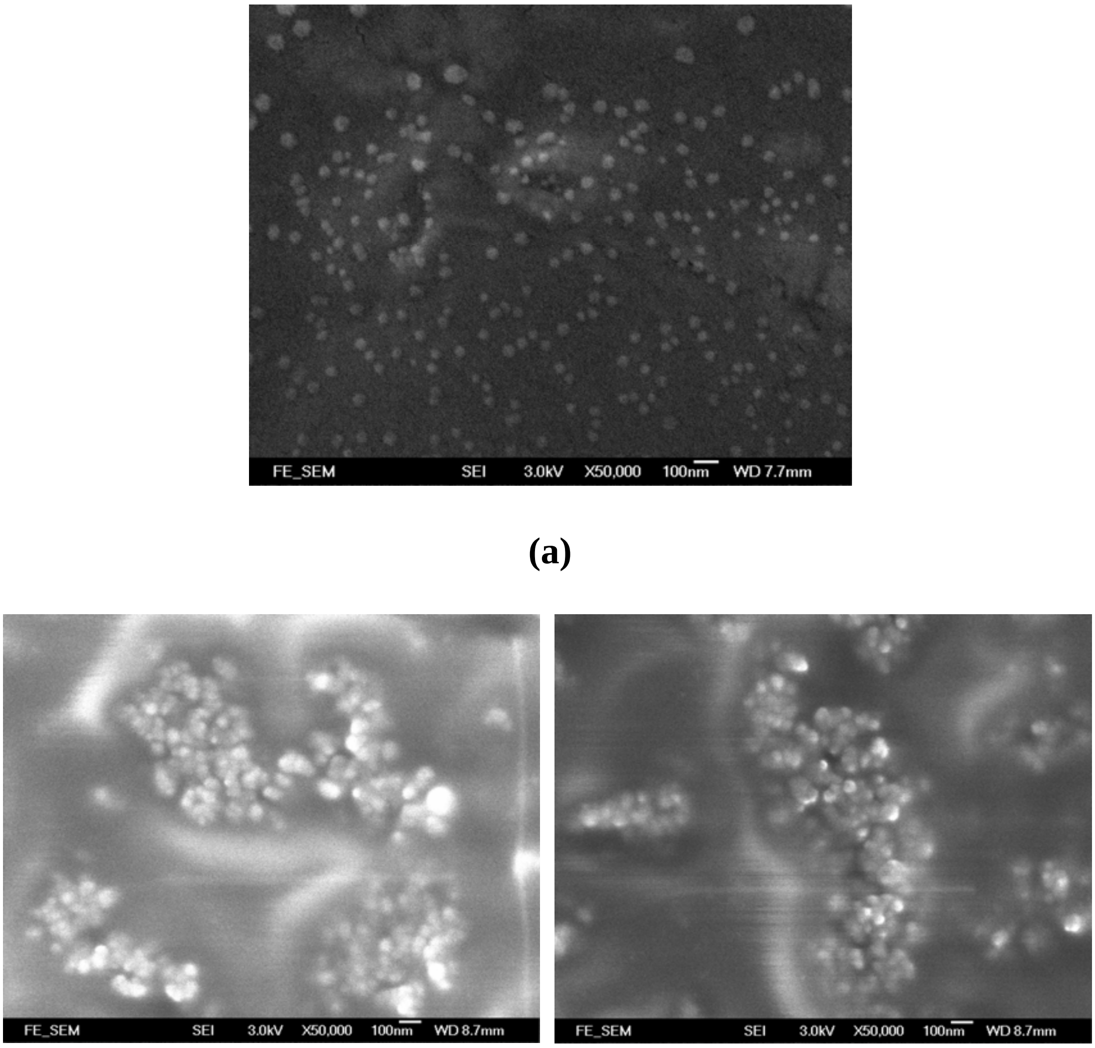

(a)

(b) **(c)**

Figure 4.1: (a) SEM images of cobalt nanoparticles prepared in hexane; (b) and (c) SEM images of cobalt nanoparticles same as (a) but displayed on carbon coated copper grid.

4.2.2 TEM Analysis

A solution droplet was also applied to the carbon coated copper grid for TEM investigation. Fig. 4.2 (a) and (b) show the TEM image of the cobalt nanoparticles. A large particle size distribution is revealed. Particles with size smaller than 20 nm can be resolved, and larger particles of size around 500 nm can also be found. Similar features have been reported by Tsuji [Tsuji 2005]. The crystalline structure of the nanoparticles was analyzed by using Selected Area Electron Diffraction (SAED) patterns. The d-spacing values obtained from diffraction bands or spots are summarized in Table 4.1. By comparing the d-spacings obtained from the SAED patterns with the values obtained from the XRD database, the nanoparticles produced was confirmed to be cobalt with HCP structure.

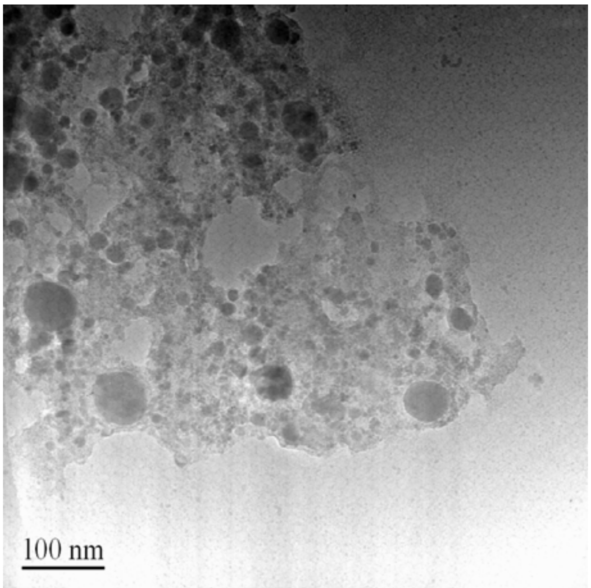

(a)

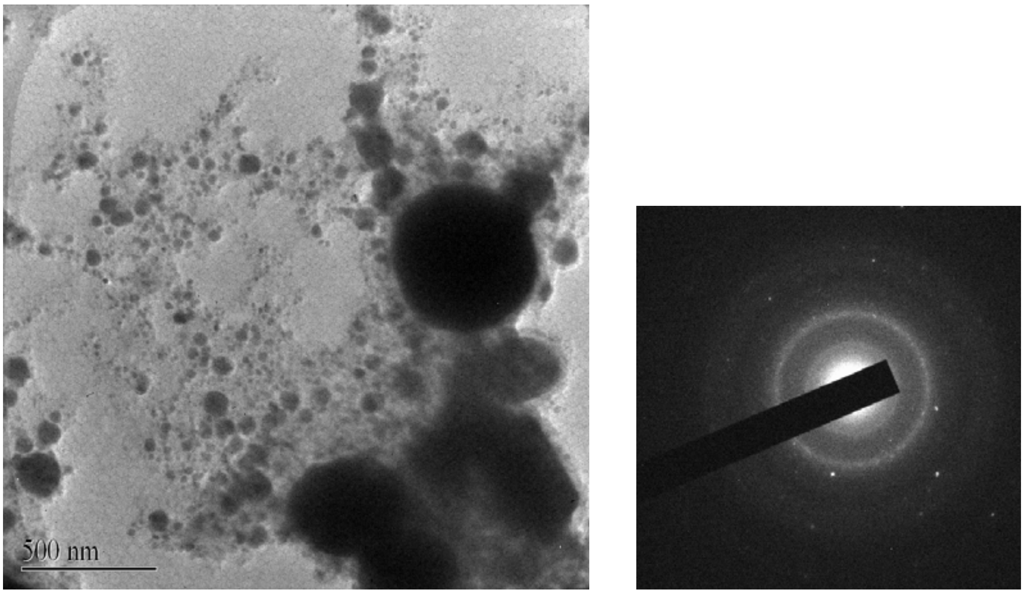

(b) (c)

Figure 4.2: **(a) and (b) TEM images of a drop of cobalt nanoparticles in hexane on carbon coated copper grid; (c) SAED of images (b).**

d-spacings (Å) (From SAED)	d-spacings (Å) of HCP-cobalt (From XRD database)	Miller index (hkl) (From XRD database)
2.05	2.02	(002)
1.94	1.91	(101)
1.27	1.25	(110)
1.2	1.15	(103)

Table 4.1: **d-spacings of cobalt of HCP structure and its corresponding miller index.**

4.3 Laser ablation in Ethanol

According to the results obtained in last section, it seems that hexane may not be a proper solvent to fabricate nanoparticles with small particle size distribution, and many of the particles are too large to behave superparamagnetically [Gong 1991, Batlle 2002]. Therefore, ethanol was chosen as another solvent for investigation and as reported by Chen [Chen 2004], no oxidation of cobalt nanoparticles was observed in the laser ablation of cobalt in ethanol.

During the whole ablation process, small bubbles can be observed along the laser beam path from the liquid surface down to the target surface. These bubbles may be the vaporized ethanol due to the high temperature [Park 2002]. After the ablation process, the color of the liquid became brownish-yellow. A magnet was then placed near the container in order to collect the magnetic cobalt nanoparticles. Black particles started to appear on the inner wall of the container after 24 hours, while the color of the liquid was still yellowish. It may be due to the carbonization of the ethanol after laser ablation. The collected black particles were then rinsed by pure ethanol for several times and finally they were dried on the silicon wafer and lined up by a magnet for convenient to the SEM investigation.

SEM Analysis

As shown in Fig. 4.3, although agglomeration of nanoparticles can be seen, the morphology of the particles can be resolved easily. The particle size is ranging from smaller than 10 nm to nearly 1 μm. Since these particles are too large and is not suitable to make thin film of few hundred nanometers thick. Therefore, laser ablation in ethanol is not a favorable method to prepare nanosized particles, at least for the magnetic cobalt metal.

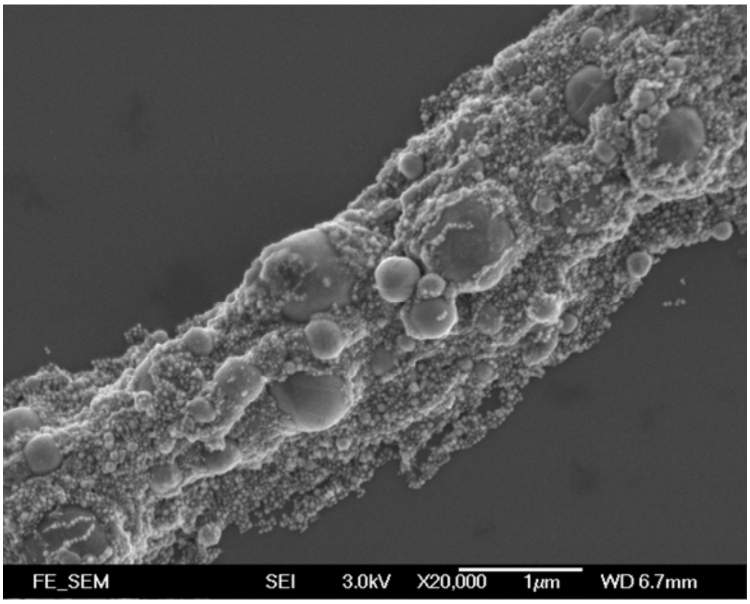

(a)

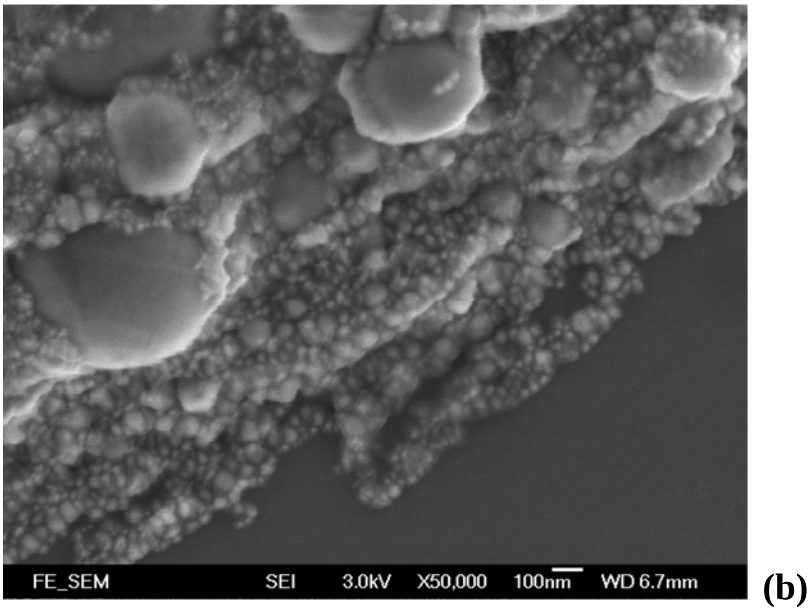

Figure 4.3: **(a) SEM images of a drop of cobalt nanoparticles in ethanol on silicon wafer (black particles can be seen by naked eyes in the droplet); (b) Higher magnification images of (a)**

4.4 Laser ablation in Toluene

For fabricating polymer film mixed with nanoparticles, it will be more convenient to find a solvent used in PLAL process which can dissolve the polymer directly without any extra cleaning or reaction process. Therefore, toluene is chosen as the solvent since it can well dissolve PMMA. In addition, the chemical formula of toluene is C_7H_8, it consists of no oxygen element, and thus oxidation of the nano-cobalt can be avoided in such a high pressure and temperature environment during the laser ablation.

The liquid is colorless at the beginning but becoming brownish-yellow after the laser ablation. After 24 hours, some black particles appeared in the solvent and were evident to be magnetic.

4.4.1 SEM Analysis

The collected black particles in the solvent by using a magnet were then transferred to a silicon wafer for SEM investigation, as shown in Fig. 4.4 (a) and (b). Serious agglomeration of the nanoparticles can be seen. The morphology of individual particle is unclear and some of them have irregular shape. The solution containing the nanoparticles was then transferred to a test tube and placed in an ultrasound machine in order to well disperse the nanoparticles in solution. The solution was then transferred to the silicon wafer and dried again, and the corresponding SEM image is shown in Fig. 4.4 (c). It can be seen that the agglomeration was less serious than before. From the SEM image, the particle size is ranged from about 20 nm - 100 nm. No particles of size larger than 100 nm have been found, which is different from the laser ablation in ethanol.

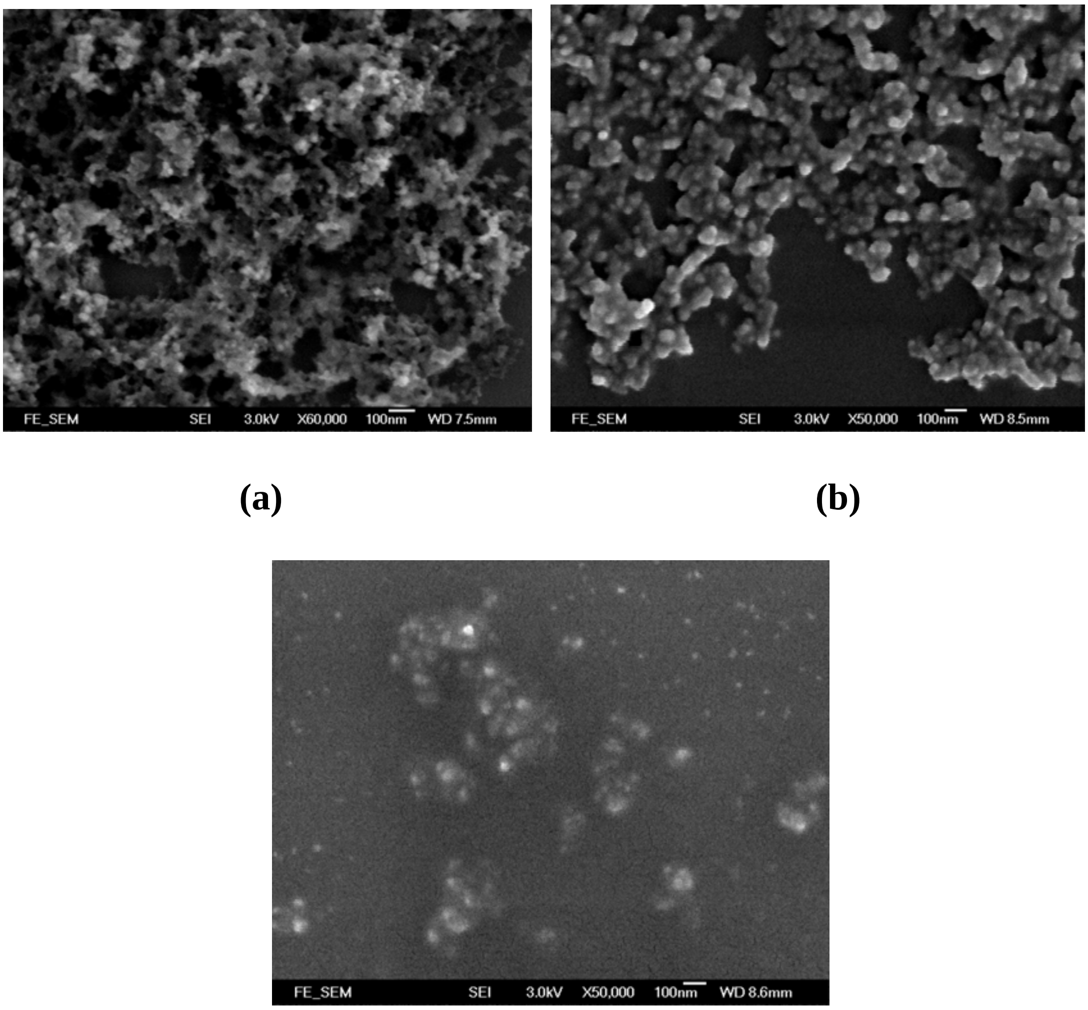

(a) **(b)**

(c)

Figure 4.4: **(a) and (b) Two different morphologies of the cobalt nanoparticle displayed on silicon wafer for SEM inspection. (c) After ultrasound dispersion, the agglomeration is less serious.**

4.4.2 TEM Analysis

Fig. 4.5 (a) and (b) show the TEM image of the cobalt nanoparticles produced by laser ablation in toluene. A relatively small particle size distribution is revealed. Most of the particles are smaller than 20 nm in diameter, which is smaller than the critical diameter of single magnetic domain [Gong 1991, Batlle 2002]. The crystalline structure of the nanoparticles was analyzed by using Selected Area Electron Diffraction (SAED) patterns. The d-spacing values obtained from diffraction bands or spots are summarized in Table 4.2. By comparing the d-spacings obtained from the SAED patterns with the values obtained from the XRD database, the nanoparticles produced was confirmed to be cobalt with HCP structure.

In fact, some of the TEM images show that the nanoparticles are located inside an unknown layer, which could be an amorphous carbon layer produced by the laser breakdown of toluene, as suggested by Toyota [Toyota 2001]. The amorphous carbon may also be the origin of the yellowish color of the solvent after the laser ablation. In addition, the produced cobalt nanoparticles can be attracted by a magnet in the solution after heating the solution to about 90°C (The purpose for heating up the solvent is to evaporate the excess solvent in a faster way) and a storage time of about one year, which indicate that there is no oxidation of the ferromagnetic cobalt nanoparticles. Laser ablation of gold in toluene has been reported by Amendola [Amendola 2005]. They found that the gold nanoparticles were covered by a very thin graphitic or amorphous carbon layer. The cobalt nanoparticles in the present study may also be protected by a very thin carbon layer such that no oxidation of the nanoparticles was occurred.

Indeed, the ablation of cobalt in toluene can be described by the nucleation and growth of nanoparticles during PLAL process [Fabbro 1990]. Immediately after the laser ablation of the cobalt target, a dense plasma plume with cobalt atoms is created at the solid-liquid interface due to the high temperature and pressure generated. When the pressure and temperature of the plasma plume start to drop down, the condensation of the plasma would result in the formation of cobalt clusters. The cobalt atoms may aggregate and form cobalt clusters by the diffusion and collision of atoms follow by steady growth of nanoparticles progress. The growth process will be stopped due to the further dropping down of the temperature and pressure. However, in between this process, laser breakdown of toluene may occur simultaneously which generate carbon atoms or clusters. The newly formed cobalt clusters or nanoparticles can be surrounded by these carbon atoms or clusters, and thus, limiting the further growth of the cobalt nanoparticles resulted in a small particle size distribution as shown in the TEM images.

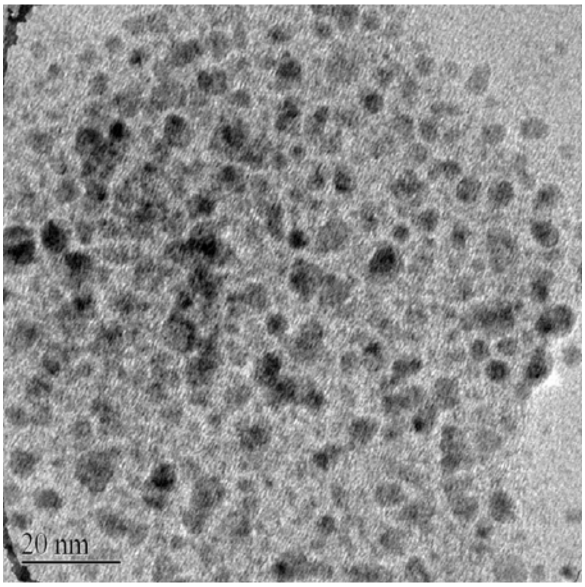

(a)

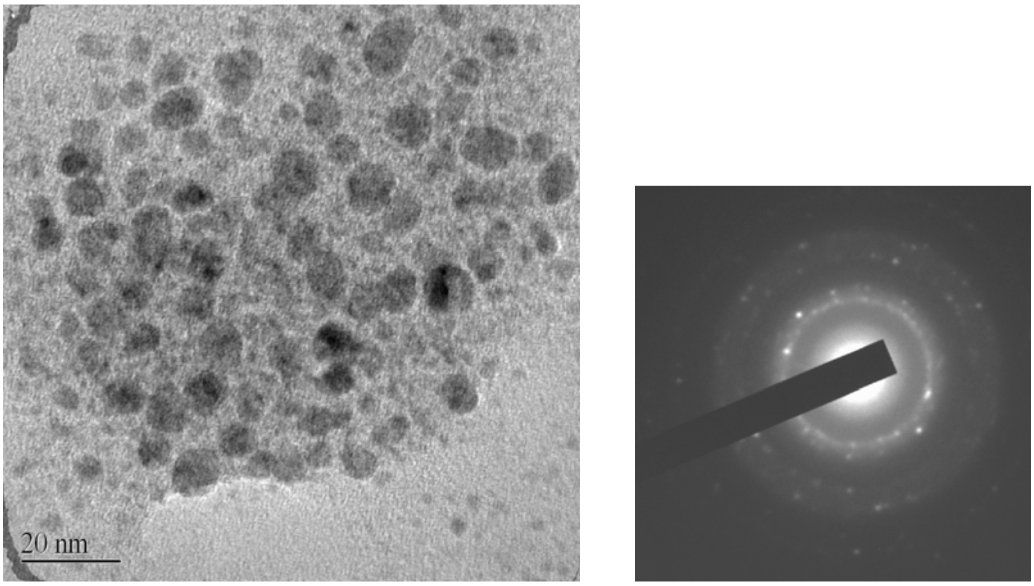

(b) **(c)**

Figure 4.5: **(a) and (b) TEM images of a drop of cobalt nanoparticles in toluene on carbon coated copper grid; (c) SAED of images (b).**

d-spacings (Å) (From SAED)	d-spacings (Å) of HCP-cobalt (From XRD database)	Miller index (hkl) (From XRD database)
2.17	2.17	(100)
2.02	2.02	(002)
1.91	1.91	(101)
1.20	1.25	(110)
1.16	1.15	(103)

Table 4.2: **d-spacings of cobalt of HCP structure and its corresponding miller index.**

CHAPTER 5

Superhydrophobicity of Polytetrafluoroethylene Thin Film Fabricated by Pulsed Laser Deposition

5.1 Introduction

Water-repellent surface is important in our daily lives as well as in many biological processes and industrial applications. In particular for the latter, a handful of examples can be named such as, fabrication of self-cleaning surfaces for windows on vehicles and buildings, prevention of icing by water-repellent coating on aerocrafts, reduction of frictional drag for underwater-processing machines, stopping clotting in artificial blood vessels and stain-resistant textiles [Coulson 2000, Nakajima 2001] etc. Due to the wide applications of surfaces with hydrophobicity, many studies have been focused on surface modification to achieve such water-repellent property. Coating with a low surface energy thin film is one of the commonly used techniques, the water contact angle of such surface can be reached is usually no more than 110°. However, in more recent studies, the contact angle of some surfaces with further treatment can reach 170° or even higher. Some of these superhydrophobic surfaces reported were roughened surfaces while many others were entrenched or grown on top of substrates with regular patterned polymers of low surface energy. The spacing of the patterns are usually less than micrometer. Therefore, it is no doubt that the enhancement of hydrophobicity of a surface is attributed to the increasing of the surface area by increasing the surface roughness [Wenzel 1936] or due to the trapped air between the water droplet and the surface as described in the Cassie-Baxter's model [Cassie 1944]. Superhydrophobic surfaces can be achieved by various processing such as the inductive coupling plasma method, plasma enhanced and hot filament chemical vapor deposition, oxygen plasma micro-roughening, soft lithography and chemical etching [Coulson 2000, Yoshimitsu 2002, Erbil 2003, Lau 2003, Tang 2006, Guo 2006] etc. The materials being utilized in these processing can be polymers with intrinsic hydrophobic properties, nano-tube, nano-wire, or bulk metal substrates. However, most methods may involve poisonous chemicals and tedious processing steps which may not be cost-effective to obtain a superhydrophobic surface for industrial applications.

Here, we present a simple one-step, easily-control and dry process for fabricating superhydrophobic surface by utilizing Pulsed Laser Deposition (PLD) technique. The superhydrophobic behavior of the PLD deposited PTFE has been observed by the past researchers in our department. And now we give a more detail study and interpretation of the results. In fact, various kinds of sensors, including the successfully prepared cobalt-PTFE composite film which can be used as a magnetic sensor, may need some protection layer on top for different purposes. Since the technique reported here is a dry process, it can be deposited on the cobalt-PTFE composite film directly, without altering the microstructure of the samples which may occur in many wet process. This layer can no doubt prevent the sensor from icing or water condensation when functioning at very low temperature or wet environment.

A well-known polymer, Polytetrafluoroethylene (PTFE) of excellent chemical stability, was chosen as the target material, since it can be easily deposited on substrates by the PLD method [Blanchet 1993, Norton 1996, Li 1998, Smausz 2002, Womack 2004]. PTFE is also known as a polymer of low surface adhesion and low surface energy, The contact angle of a smooth PTFE surface is about 108° [Fox 1950], while the samples prepared by this simple method can reach 170° or even higher. It is shown to be dependent on the deposition number of pulses. Therefore, it is obvious that in combining materials with low surface energy and the PLD technique to produce nano-structured surface, products or devices which require superhydrophobicity can be fabricated with an easy and convenient method.

Literature Review of Superhydrophobicity

Hydrophobic property of a surface, or wettability, are characterized by the static contact angle (or simply contact angle) made between a surface and a water droplet. In general a surface is hydrophobic if the contact angle is greater than 90°. For surface with a contact angle larger than 150°, is usually called superhydrophobic. Superhydrophobic phenomena have been firstly observed in nature, for example the unwettable lotus leaf. In recent year, superhydrophobicity have attracted much interest in both fundamental research and practical applications. Owing to the rapid advances in nanotechnology since 1980s, fabrication of surfaces with non-wetting behavior in micro/nanoscale becomes important. Moreover, there are always demands of self-cleaning surfaces for applications on vehicles, buildings and aerocrafts [Coulson 2000, Nakajima 2001].

The contact angle θ depends on the interfacial free energies: solid-liquid (γ_{sl}), solid-vapor (γ_{sv}), and liquid-vapor (γ_{lv}). The Young's equation, $\gamma_{sl} + \gamma_{lv} \cos \theta = \gamma_{sv}$, correlates the free energies of the three interfaces with the liquid-solid contact angle. There is always a tendency of the liquid to minimize the total free energy of the system on a flat substrate surface. Complete wetting ($\theta = 0°$) happens on solids with a high surface energy (γ_{sv}), while liquid on low energy surfaces tends to form droplets with a high contact angle. Therefore, material with low surface energy, such as fluorinated material, is normally used in fabricating non-wetting surface. It is well known that roughness of a hydrophobic solid enhances its hydrophobicity. Two different models have been proposed to explain this effect. The first one was proposed by Wenzel which considered the increase of contact area due to the surface roughness [Wenzel 1936]. Considering a rough solid surface with the size of roughness smaller than the size of the droplet, as shown in Fig. 5.1, and a homogeneous interface formed by the water droplet in contact with the rough surface without air pockets, the contact angle is given in the following equation:

$$\cos\theta = R_f \cos\theta_{0,}$$

where θ_0 is the contact angle for a smooth surface, θ is the contact angle for a rough surface, and R_f is the roughness factor defined as the ratio of the solid-liquid area (A_{sl}) to its projected area on a flat plane (A_0) :

$$R_f = A_{sl}/A_{0,}$$

Wenzel's model predicts that the hydrophobicity will be enhanced if θ_0 is greater than 90° and will be decreased if θ_0 is less than 90°, with increasing R_f.

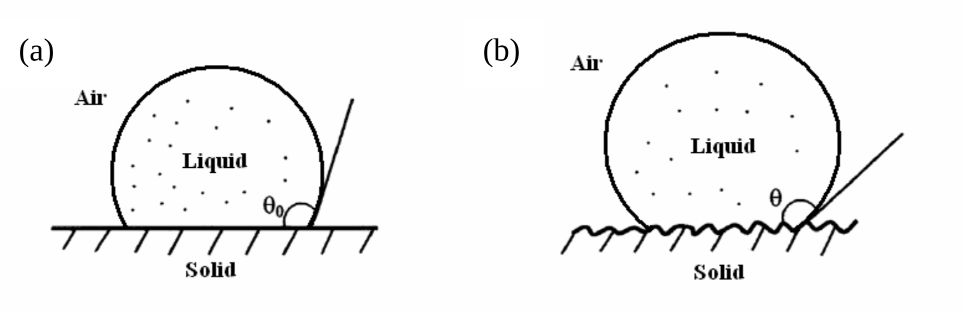

Figure 5.1: **Schematic diagram of a droplet of liquid in contact with a solid surface (a) smooth surface with contact angle θ_0 and (b) rough surface with contact angle θ.**

Cassie and Baxter have extended Wenzel's model, which was originally developed for a homogeneous solid–liquid interface [Cassie 1944]. In their model, liquid may not fully penetrate into cavities between the asperities of a rough surface, but forming air pockets underneath the liquid. This will lead to a formation of a composite solid-liquid-air interface as shown in Fig. 5.2. Cassie and Baxter proposed a model to calculate the contact angle by considering the contribution of the fractional area of wet surfaces (solid-liquid interface) and the fractional area with air pockets (liquid-air interface). The contact angle is finally given by:

$$\cos\theta = f_{\mathrm{sl}} \cos\theta_0 + f_{\mathrm{sl}} - 1,$$

where f_{sl} is the fractional area of the solid-liquid interface, θ is the calculated contact angle and θ_0 is the contact angle on the smooth surface of the same material. It was found that the Cassie and Baxter's model fit many micro- or nano-structured systems.

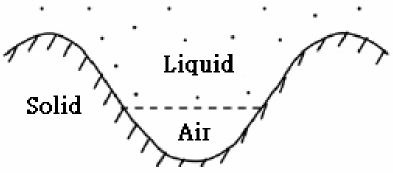

Figure 5.2: **Schematic diagram of a composite solid-liquid-air interface for a rough surface.**

Another important characteristic appearing on a rough surface is the contact angle hysteresis. Contact angle hysteresis (θ_{H}), as shown in Fig. 5.3 (a), is defined as the difference between the advancing and receding contact angles, i.e. $\theta_{\mathrm{H}} = \theta_{\mathrm{adv}} - \theta_{\mathrm{rec}}$. The sliding angle, as shown in Fig. 5.3 (b) schematically, is defined as the angle when a water droplet of certain volume begins to slide down an inclined plane. Small sliding angle is always observed with small contact angle hysteresis. The contact angle hysteresis occurs due to surface roughness and heterogeneity. It was found that for a homogeneous interface without any air pockets (liquid-air interface), increasing roughness tends to increase the contact angle hysteresis, while for a composite interface with air-trapping, increasing roughness results both high contact angle and small contact angle hysteresis. Therefore, composite interface with air-trapping, described by Cassie and Baxter's model, is a main factor to produce superhydrophobic surface with good self-cleaning properties. It was also reported that the combination of micro- and nano-structures is needed in order to produce a stable composite interface and minimize the destabilizing factors such as capillary waves, nanodroplet condensation, and liquid pressure.

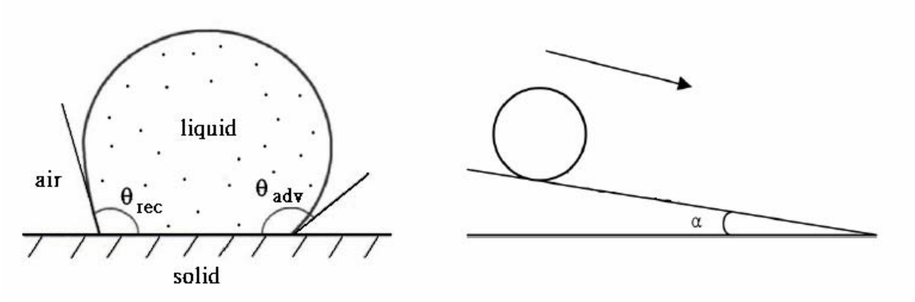

(a) (b)

Figure 5.3: **Schematic diagram of (a) a liquid droplet in contact with a rough surface, with advancing (θ_{adv}) and receding contact angle (θ_{rec}); (b) a liquid droplet sliding down on a tilted surface, with a sliding angle α.**

5.2 Infrared Spectroscopy

Fig. 5.4 shows the FTIR spectrum of PTFE produced by PLD. The inclined baseline is caused by the scattering of KBr particles which was used to mix with the PTFE for the FTIR measurement. The typical absorption peaks of PTFE at around 1224 and 1155 cm^{-1} are assigned to the asymmetrical and symmetrical stretching modes of CF_2 bond respectively. The peaks with smaller intensity at around 640-620 cm^{-1} are attributed to the chain stretching and wagging modes of CF_2 bond, while the bending and rocking modes are at 553 and 507 cm^{-1} respectively [Li 1998, Womack 2004]. This spectrum shows that PTFE film was successfully deposited. However, the PTFE films fabricated also appear a very light yellowish-grey colour, as reported from other study, which is possibly due to the fluorine deficiency in the samples [Holland 1976].

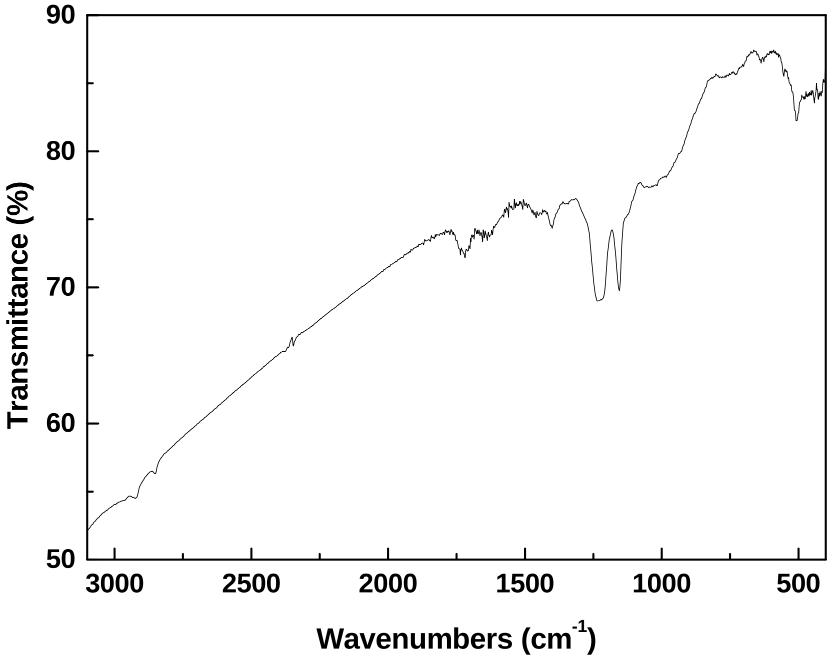

Figure 5.4: **FTIR spectra of PTFE film deposited by PLD.**

5.3 Surface Morphology

The SEM images of the deposited PTFE film fabricated with various number of laser pulses were shown in Fig. 5.5, where (a), (b) and (c) are of 200, 500 and 1800 number of pulses respectively. They reveal a rough morphology consisting of mainly two kinds of particles. One is the particles, or say, asperities, of size ranging from 60 nm to 500 nm. The other is larger particles of size larger than 500 nm which may correspond to the agglomeration of individual smaller particles or the particulates which are commonly generated during the PLD deposition of polymer [Blanchet 1993, Norton 1996, Li 1998, Smausz 2002, Womack 2004]. Despite the larger particulates, it can be seen that the film surface consist of only few asperities of size smaller than 500 nm in Fig. 5.5(a). The film surface becomes rougher with increasing number of nano-size asperities when number of pulses increases to 1800, as shown in Fig. 5.5(c).

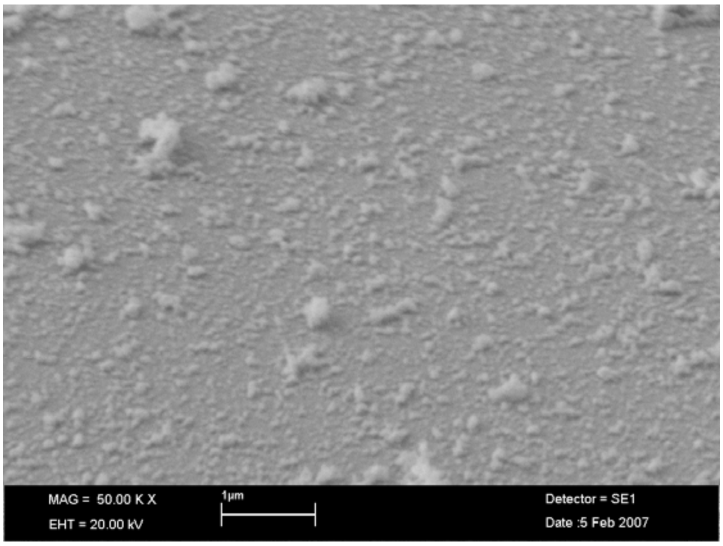

(a)

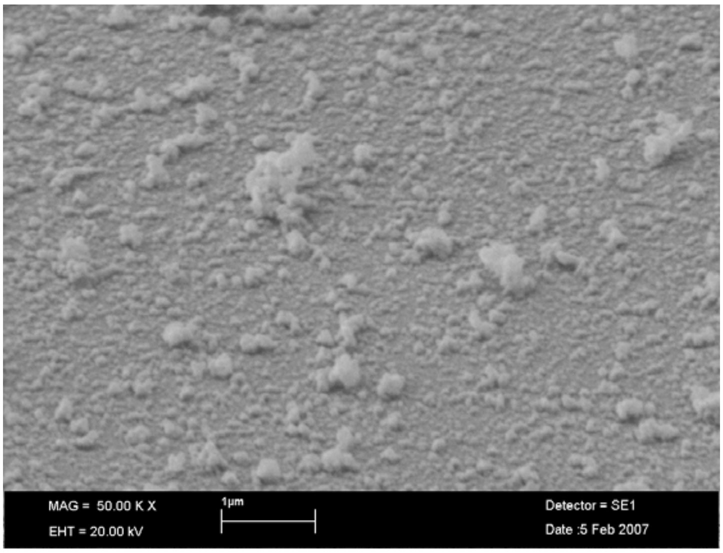

(b)

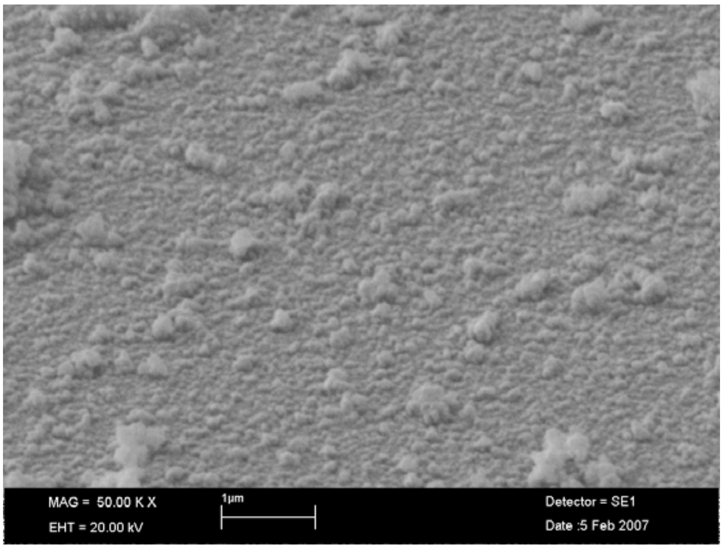

(c)

Figure 5.5: **SEM images of the PLD deposited PTFE film fabricated with (a) 200, (b) 500 and (c) 1800 number of pulses. The contact angles on the corresponding surface are (a) 103°, (b) 144° and (c) 168° respectively.**

The surface roughness of the PTFE film versus different number of pulses was investigated by AFM as shown in Fig. 5.6. The number of pulses dependence of the surface morphology and the size of the asperities are consistent with the SEM images.

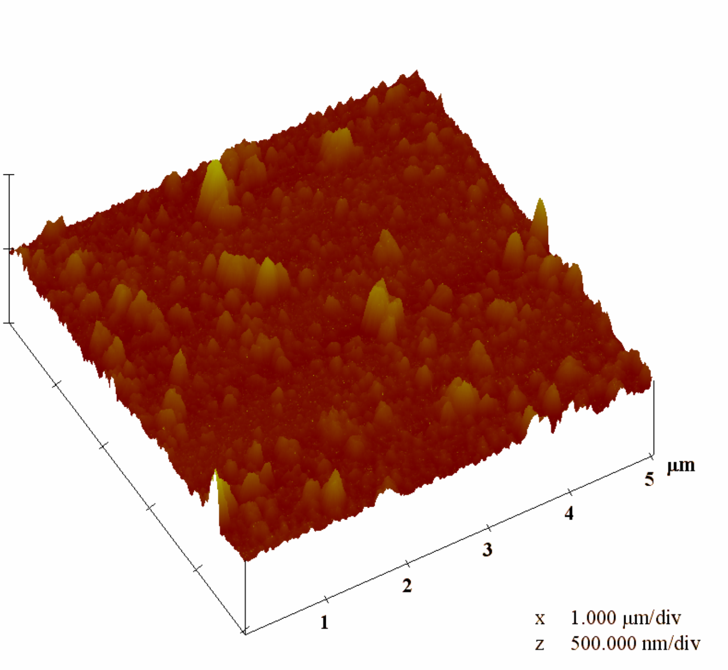

(a)

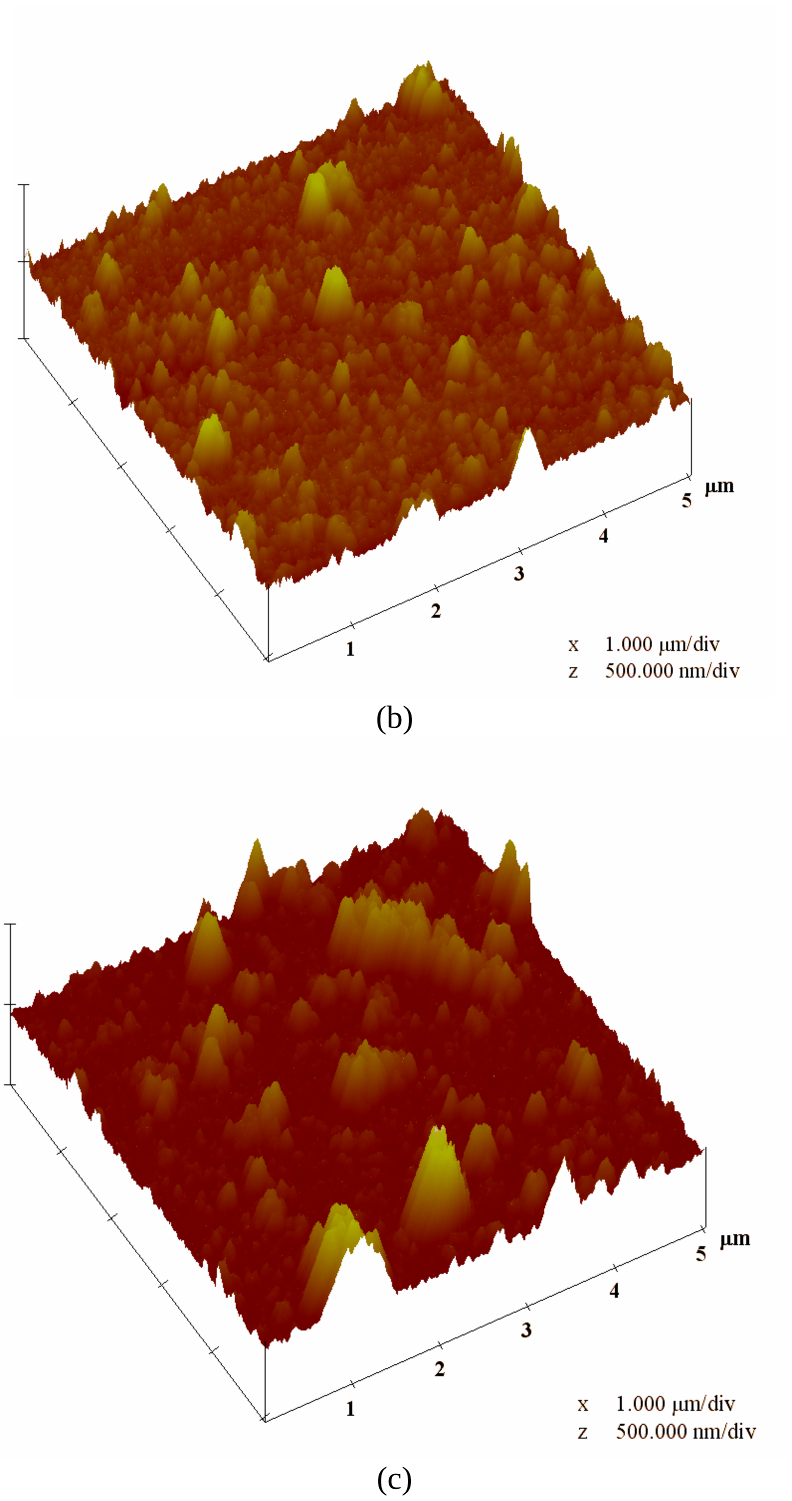

(b)

(c)

Figure 5.6: **AFM images of the PLD deposited PTFE film fabricated with (a) 200, (b) 500 and (c) 1800 number of pulses. The corresponding surface roughness (rms) are (a) 33.6 nm, (b) 40.4 nm (c) 77.6 nm respectively.**

The relation between the root-mean-square (rms) roughness, which was the standard deviation of the height values obtained from the AFM images of a given area, and the number of pulses was shown in Fig. 5.7. It shows a clear trend that the roughness (rms) increases with the number of laser pulses. This trend is consistent with the SEM and AFM images, which may be due to the increasing numbers of nano-sized asperities.

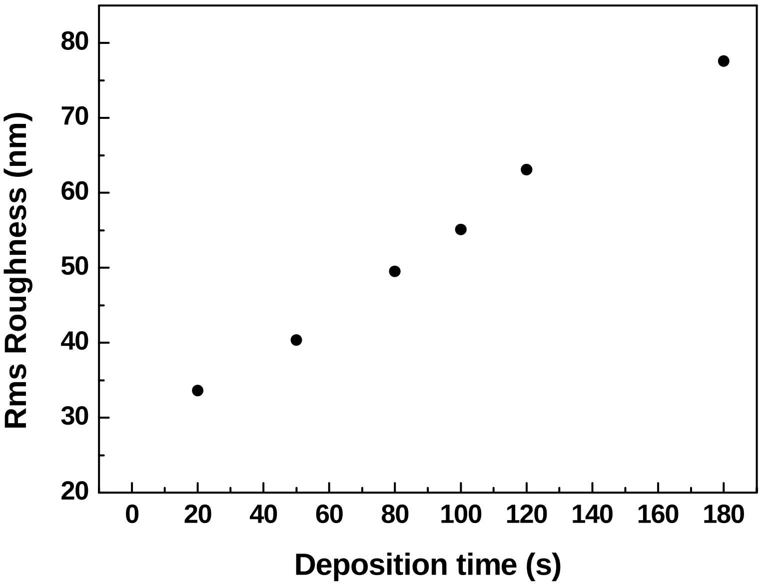

Figure 5.7: Number of pulses dependence of roughness (rms) of the PLD deposited PTFE film.

5.4 Contact Angle Measurement

The measured water contact angle against the roughness (rms) was shown in Fig. 5.8. It shows that the value of contact angle continue to increase until the roughness (rms) reaches a value larger than 50 nm, and then it comes to saturate, achieving a contact angle of about 170°. The measured contact angle of the glass substrate is about 60°.

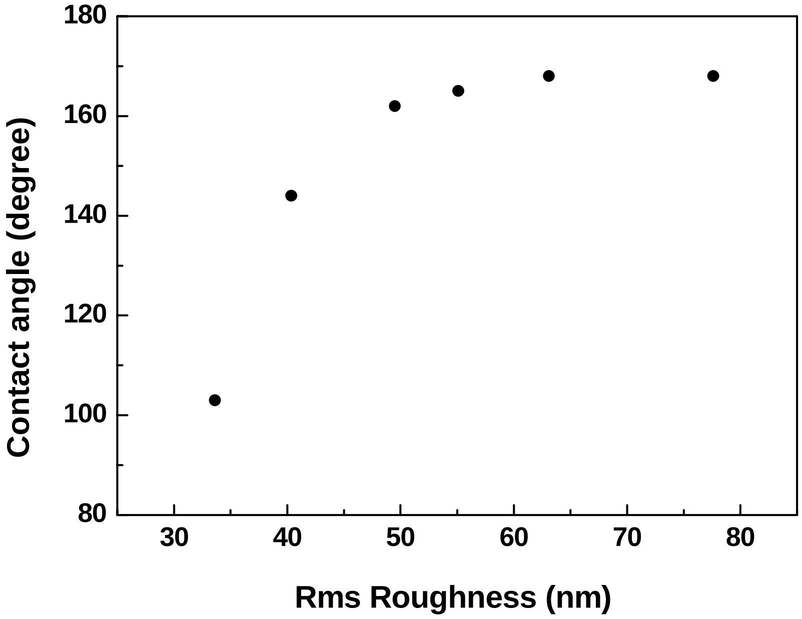

Figure 5.8: Roughness (rms) dependence of contact angle of the PLD deposited PTFE films. Water droplet with volume of 5 μL was used in the measurement.

The images of 5 μL water droplet locating on the PLD deposited PTFE film with different number of pulses, were shown in Fig. 5.9. The corresponding number of laser pulses of Fig. 5.9 (a), (b) and (c) are 200, 500 and 1800 respectively, which are the same as those shown in the captured SEM and AFM images.

The sliding angle, defined as the angle when a water droplet of certain volume begins to slide down an inclined plane, was also measured. The sample with contact angle of about 170° was used for this measurement. The result shows that the sliding angle is smaller than 2° for both 5 μL and 10 μL water droplets. In addition, the contact angle remains nearly the same when changing the volume of the water droplet from 2 μL to 10 μL, as shown in Fig. 5.10. This indicates that the fabricated PTFE films have a good self-cleaning ability in real application with a stable surface structure. In addition, the superhydrophobic PTFE film was also deposited on polymer surface besides glass substrates. Polymethyl methacrylate (PMMA) polymer film was fabricated on glass substrate by using spin-coating method and the superhydrophobic PTFE film was then deposited on top directly. The contact angle of smooth PMMA surface is about 74°. It is found that the new surface becomes superhydrophobic and has a very small sliding angle, protecting the underlying PMMA layer from wetting. This result shows the flexibility of this technique.

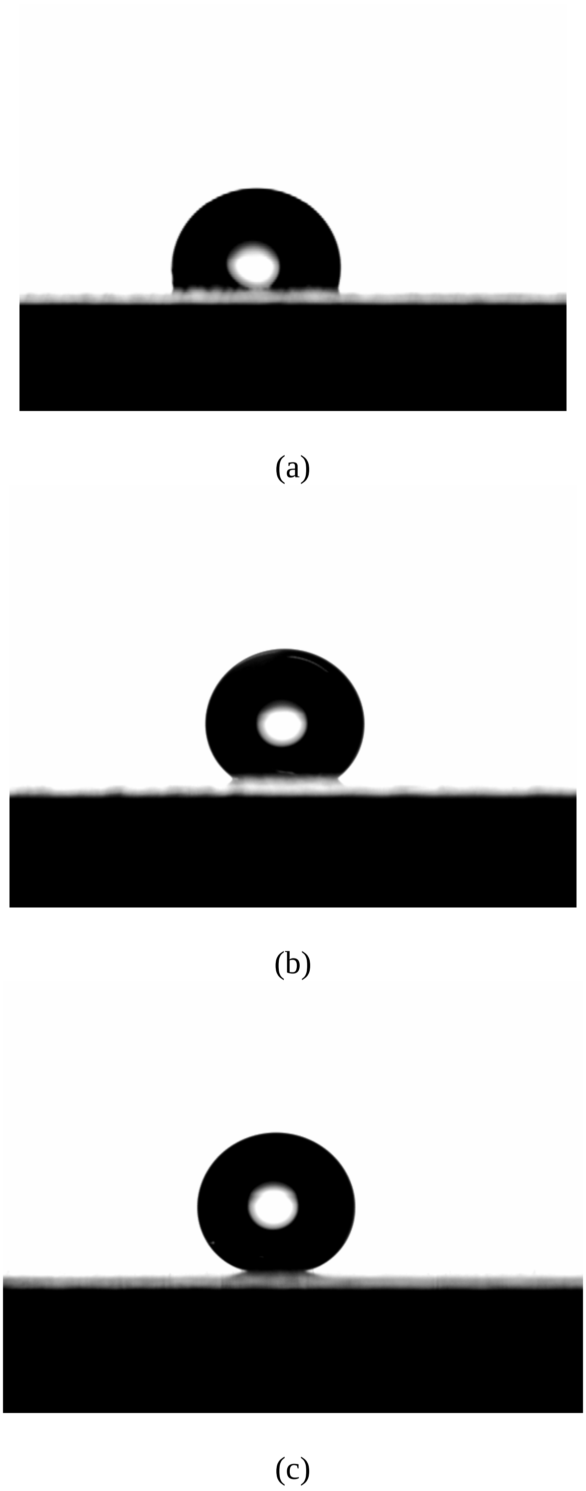

Figure 5.9: Images of 5 μL water droplets on the PLD deposited PTFE films fabricated with (a) 200, (b) 500 and (c) 1800 number of pulses. The corresponding contact angles are (a) 103°, (b) 144° and (c) 168° respectively.

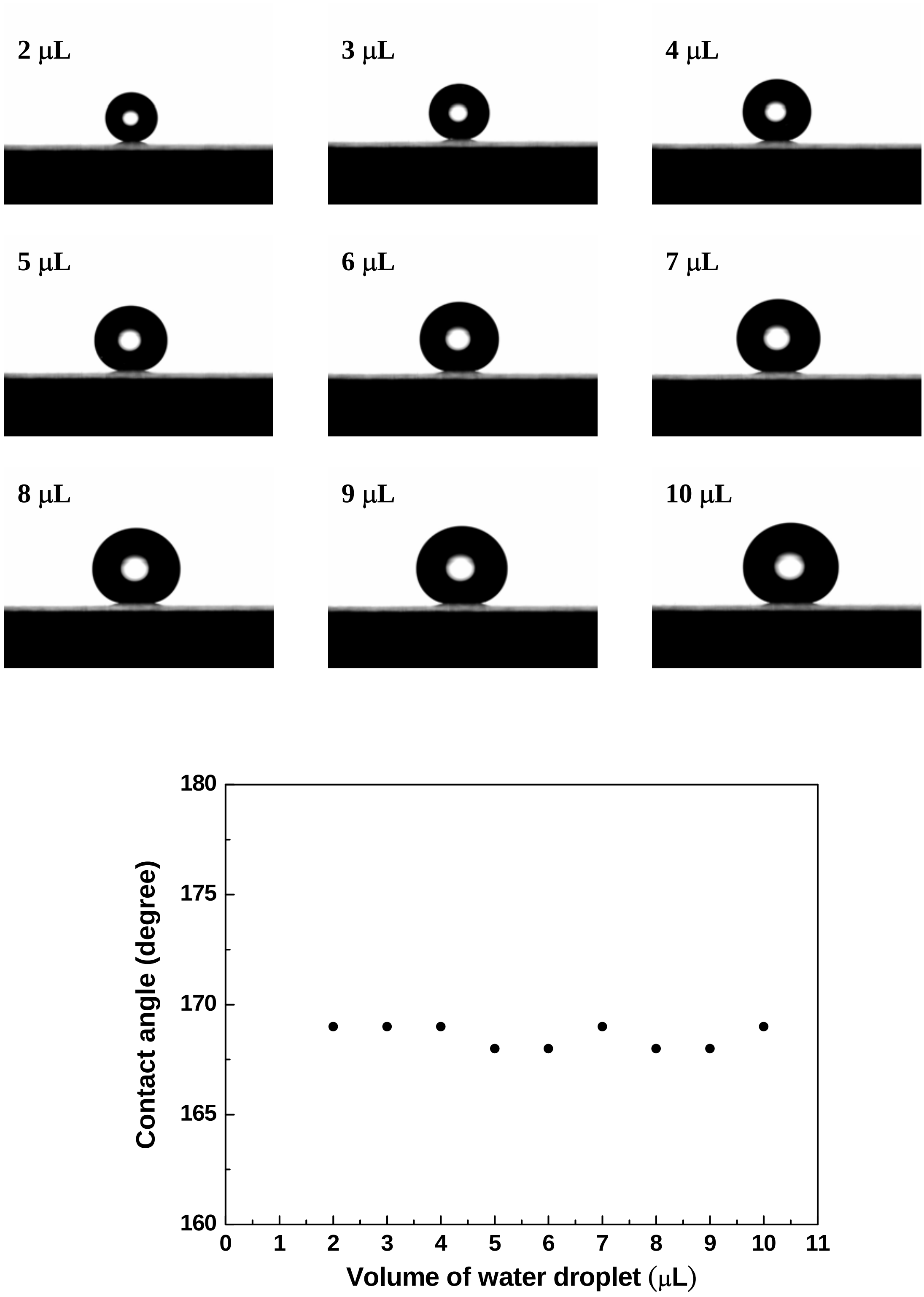

Figure 5.10: **Water droplet volume dependence of contact angle of the PLD deposited PTFE films.**

The observed increasing of contact angle with deposition time can be explained as follow. When the number of pulses increases to 200, the deposited PTFE starts to form a compact film with very few nano-sized asperities, which achieving a contact angle of about 103°, quite near the contact angle of the smooth bulk PTFE surface [Fox 1950]. When the number of pulses was increased, the roughness of the deposited PTFE film was increased associated with the increasing number of nano-size asperities produced on the surface. These nano-sized asperities help to trap air in between the water droplet and the space between the asperities, such that the water droplet stands on them with small liquid-solid contact area. This follows the Cassie-Baxter's model [Cassie 1944] with their proposed equation, $\cos\theta' = f\cos\theta + f - 1$, where f is the area fraction of the liquid-solid interface, θ' is the observed contact angle and θ is the contact angle on the smooth surface of the same material. When the roughness increases, more air can be trapped in between the asperities and the water droplet surface, thus reducing the liquid-solid contact area.

According to the Cassie-Baxter's equation, the reduction of liquid-solid contact area will lead to a higher contact angle. Therefore, when the number of laser pulses was larger than 800, a surface of very dense nano-sized asperities was produced, such that the space trapped with air is the largest and the total contact area of water and the film surface is the smallest, and finally achieving the largest contact angle. In addition, the small sliding angle observed indicate a low contact angle hysteresis, which is also contributed to the air trapping under the water droplet [Johnson 1963]. The large contact angle and the small sliding angle observed infer that the superhydrophobicity of the PLD deposited PTFE film is no doubt a result of the nano-scale structure induced air trapping [Soeno 2004, Wu 2006] as suggested by Cassie-Baxter.

CHAPTER 6

Fabrication of nano-sized cobalt hydroxide through laser deposition process

6.1 Introduction

In this chapter, we will discuss the formation of uniform hexagonal nanoplatelets on glass substrates. This study is motivated by the surprising results obtained as a result of the Cobalt-PTFE composite film is reacted with NaOH. It was originally intended to remove the cobalt particles in the composite films prepared by PLD. However, the outcome is the formation of cobalt hydroxide in the PTFE network with an amazing regularity in the microstructure.

The preparation of cobalt hydroxides has drawn much attention in recent years because of their usage as electric and catalytic material with many other technological applications. Cobalt hydroxide has a hexagonal layered structure in which the divalent cobalt cation is located in the octahedral site generated by six hydroxylic oxygen ions [Kamath 1997]. These two dimensional metal–hydroxyl sheets are stacked up with hydrogen bond to form a three-dimensional structure. When the interlayer space of the two-dimensional metal-hydroxyl sheet contains no anion, the cobalt hydroxide is in the brucite-like phase and is denoted as β-cobalt hydroxide. Cobalt hydroxides prefer to grow into platelets due to their intrinsic lamellar structures. Cobalt hydroxides have been used as additives to improve the electrochemical activity of alkaline secondary batteries [Bauer 1990]. It has been reported that cobalt hydroxide films show catalytic and reversible electrochromic properties [Jozer 1998, Dinamani 2000]. Organic groups have been incorporated into the interlayer region of cobalt hydroxides to fabricate organic magnetic materials [Kurmoo 1999]. Recently, it has been found that nanosized cobalt hydroxide/zeolite composite shows potential application as an electrochemical supercapacitor [Cao 2004]. This interesting result indicates that nanosized cobalt hydroxide would have potential in both physical and chemical applications. Therefore, many approaches have been attempted to prepare cobalt hydroxide nanoplatelets [Hou 2005, Liu 2005, Yang 2006]. However, most of them are chemical process which involves time-consuming and complicated steps [Zhang 2000, Zhu 2002]. Toxic chemicals and contaminants may also be generated in these processes. The as-prepared cobalt hydroxide platelets are mostly in powder form.

Here, we will present an innovative method to fabricate the cobalt hydroxide nanoplatelets at room temperature. It is simply using the sodium hydroxide (NaOH) solution to react with a pure cobalt thin film prepared by pulsed laser deposition. This method provides a simple and relatively fast and clean route to produce nano-sized cobalt hydroxide. The as-prepared cobalt hydroxide platelets are in thin film form which is already grown on the substrate surface with good adhesion. Many practical applications as mentioned above are anticipating this format of nanosized cobalt hydroxide on substrate.

The starting material for the fabrication cobalt hydroxide was to prepare the cobalt thin films by PLD. Laser wavelength of 532 nm, which is generated by the second harmonic of Nd:YAG laser, was used in this PLD process. The concentration of the NaOH solution was about 0.5M and the reaction time was kept at about 90 min for all samples. It may not be the optimized value but is sufficient to get the required products. The nanoplatelets formed were characterized by scanning electron microscope (SEM), X-Ray Diffraction (XRD) and Fourier transform infrared spectroscopy (FTIR). The results obtained from these investigations inferred that the hexagonal shape nanoplatelets are the brucite-like phase β-cobalt hydroxide. It was also found that the deposition time is a crucial factor to control the size and morphology of the products.

6.2 Surface Morphology

Prior to the study of pure cobalt hydroxide, the composite film of Co-PTFE were put forth to the tests. Fig. 6.1 (a) and Fig. 6.2 (a) show the SEM images of the Co-PTFE composite film fabricated with Co:PTFE laser pulse ratio of 22:4 and 14:2 respectively. The samples were reacted with NaOH (0.5M) for 90 min at room temperature. The reaction results are shown in Fig. 6.1 (b) and Fig. 6.2 (b). The surface morphology of the samples changes significantly. Large amount of platelets grow upward from inside of the film with random orientation. The size of the platelets is from about 100 nm to 500 nm, and the thickness is about 50 nm or even smaller. Two kinds of platelets can be observed, irregular shape and nearly hexagonal shape. It is well known that PTFE is the most chemically stable polymer which cannot be easily attacked by acid or alkaline. Two PLD deposited PTFE films with and without treatment in NaOH solution were prepared for comparison. The surface morphologies of the two films are shown in Fig. 6.3 (a) and (b) respectively. As expected, no significant difference is found in the SEM images, except that the density of particulates changes due to its variation from different locations.

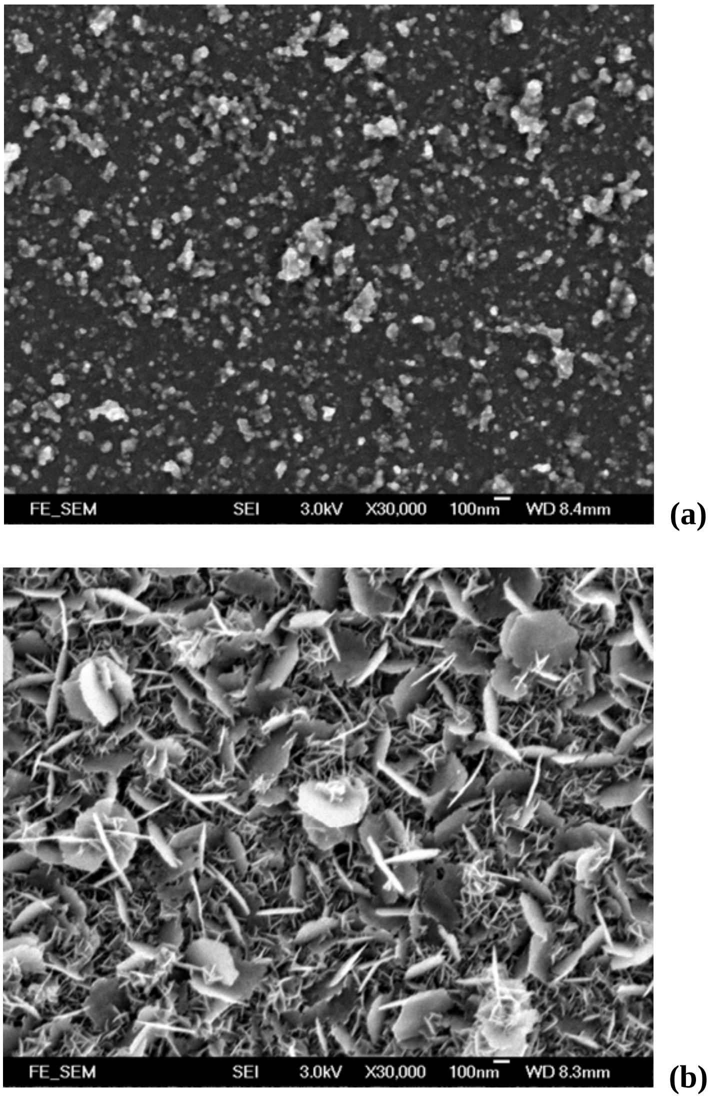

Figure 6.1: **SEM images of the Co-PTFE composite film fabricated with Co:PTFE laser pulse ratio of 22:4 (a) without any treatment; (b) reacted with NaOH (0.5M) for 90 min.**

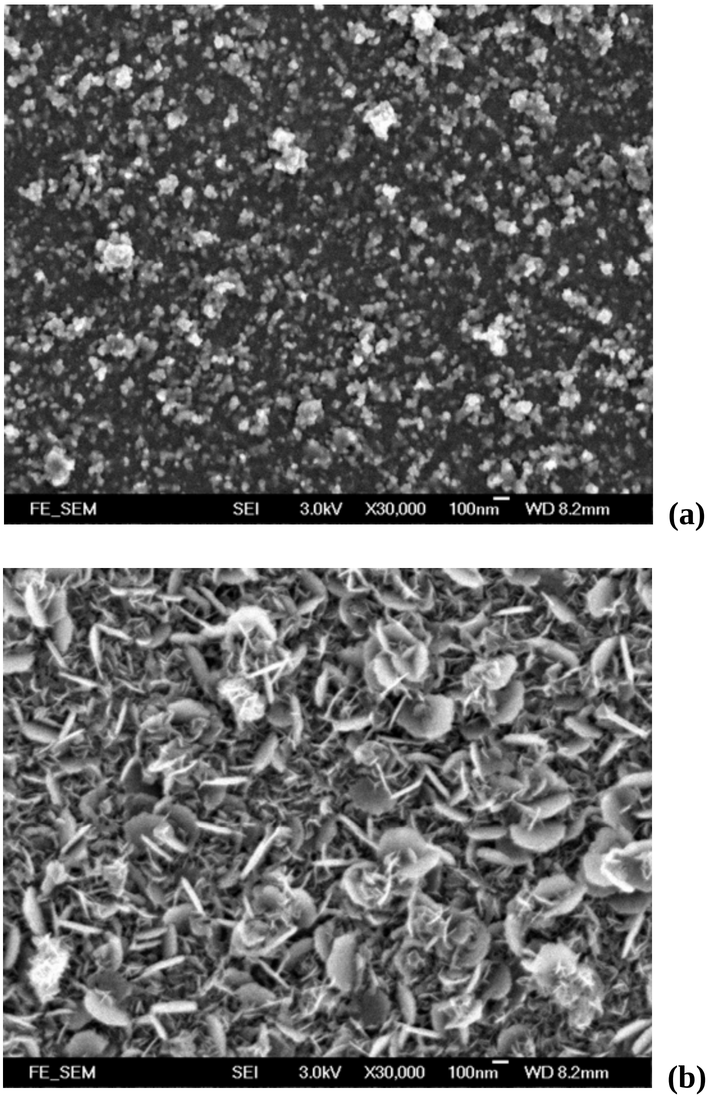

Figure 6.2: SEM images of the Co-PTFE composite film fabricated with Co:PTFE laser pulse ratio of 14:2 (a) without any treatment; (b) reacted with NaOH (0.5M) for 90 min.

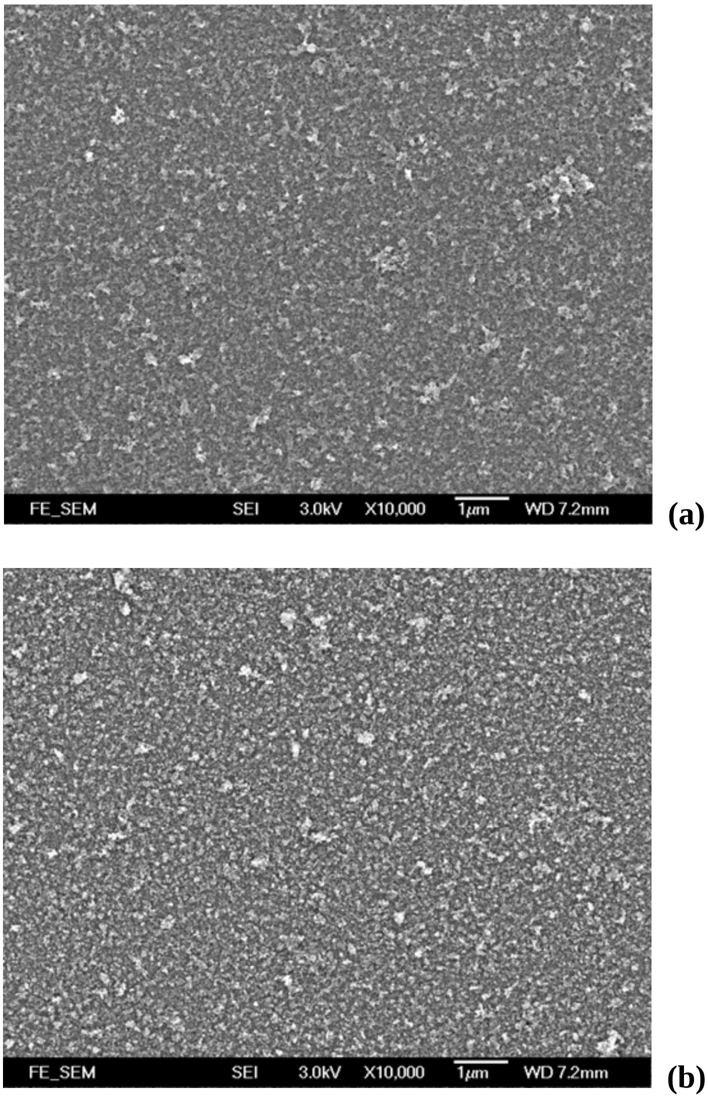

Figure 6.3: **SEM images of the PLD deposited PTFE film (a) without any treatment; (b) reacted with NaOH (0.5M) for 90 min.**

In order to further verify the contribution of the nanosized cobalt by PLD in the formation of the nanosized platelets, a neat Co film deposited by PLD was prepared. Its SEM image with a tilting angle of 30° is shown in Fig. 6.4 (a). The film surface is fairly smooth with just a few particulates. The film after reacted with NaOH is shown in Fig. 6.4 (b), with a tilting angle of 30°. The top view of the sample surface is also shown in Fig. 6.4 (c) for comparison. After the reaction, a lot of platelets appear on the surface, while most of them are hexagonal in shape with some smaller irregular platelets. These hexagonal platelets tend to grow up from the substrate surface, with a size of about 500 nm. This result confirms that the platelets appeared on the Co-PTFE composite film surface after reacting with NaOH, should only be the reaction between the NaOH and the Co particles embedded in the composite film.

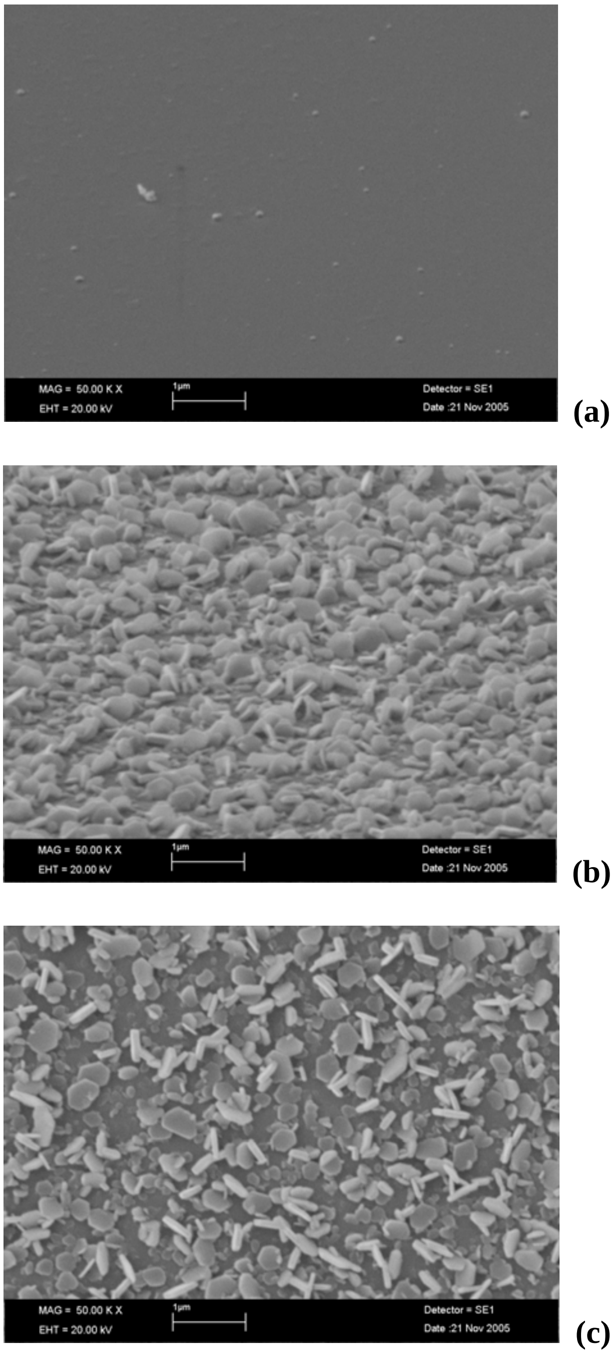

Figure 6.4: **SEM images of the PLD deposited Co film (a) without any treatment; (b) and (c) reacted with NaOH (0.5M) for 90 min. Images (a) and (b) was tilted 30° from horizontal. Image (c) is the top view of the sample surface.**

Besides, in a detail study of the neat Co PLD film after reaction with NaOH, it is found that the nano-sized platelets grew in a different morphology at different location of the sample. Fig. 6.5 (a) to (e) show the SEM image of the platelets at the corresponding locations as indicated in the schematic diagram in Fig. 6.5 (f). Location (a) is at the centre of the sample where the PLD plasma plume was directly pointed and the deposition rate is the highest. Location (e) is at the outer rim of the sample where the deposition rate will be lower.

As shown in Fig. 6.5 (a) and (b), platelet-like structure can be found growing on the sample surface, but nearly all of them can only grew into small part of platelets. However, as shown in Fig. 6.5 (c), the platelets grew larger but still only one half of a hexagon, and the platelets interpenetrated with each others. The average diagonal of these platelets is about 1 μm and the thickness is about 50 nm.

The surface morphology in location (d), which is white in appearance as seen by naked eyes, is shown in Fig. 6.5 (d). There are more or less complete hexagonal platelets but still many grew into only half of a hexagon. These platelets grow in random orientation, while some of them tend to interpenetrate in other platelets. A higher magnification SEM image is shown in Fig. 6.5 (e). The size of the platelets is quite similar and the diagonal of the hexagons is about 700 nm, and the thickness is about 100 nm. The above results imply that it is possible to produce a uniform size distribution of hexagonal nano-platelets with good adhesion on the glass substrate.

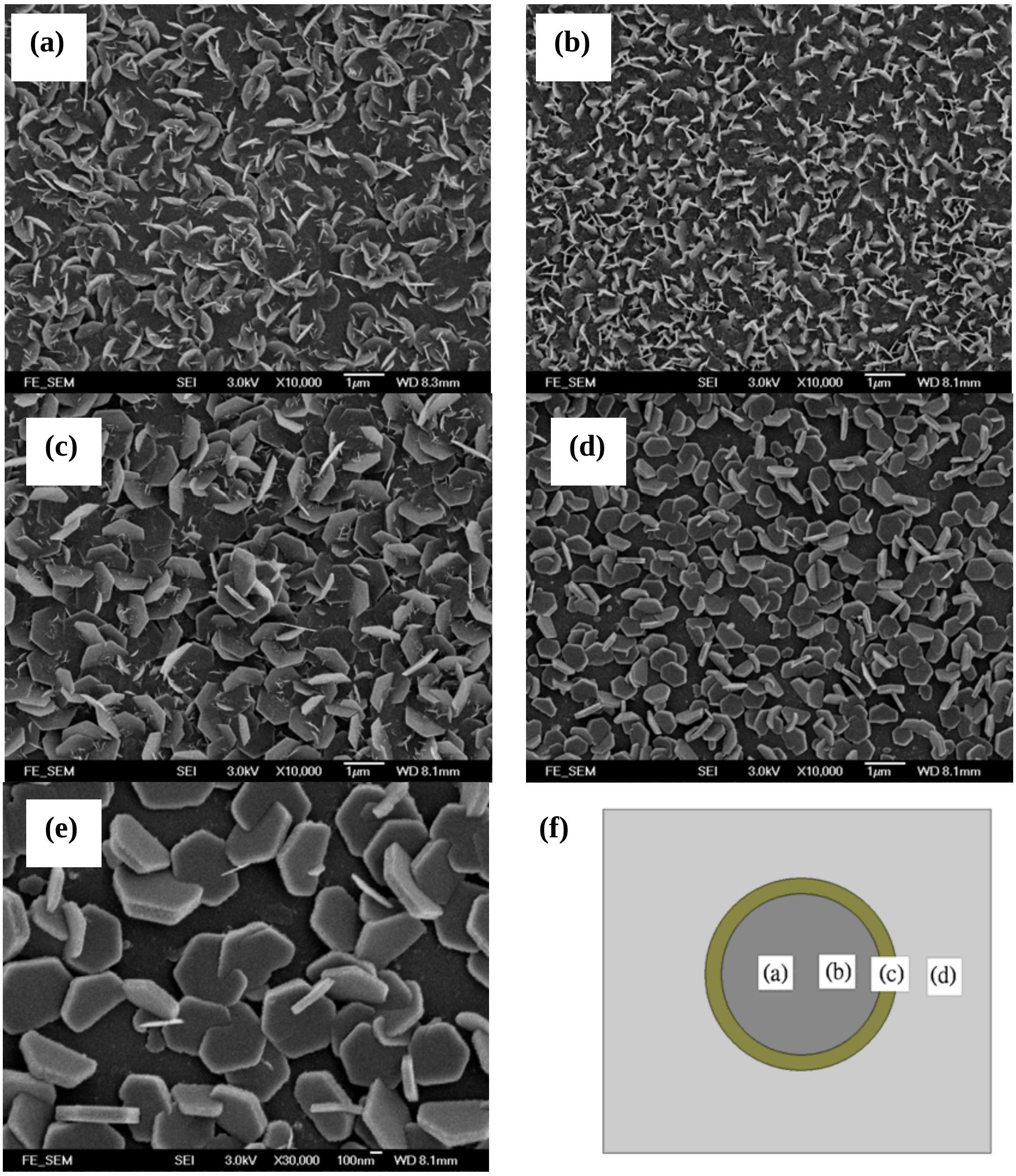

Figure 6.5: **(a) – (d) SEM images of the PLD deposited Co film reacted with NaOH (0.5M) for 90 min. (e) Higher magnification of (d). (f) Schematic diagram (top view) of a substrate surface with the reacted Co film, representing the locations for the observation of (a) – (d). The color is for easy differentiation only.**

6.3 XRD analysis

To identify these nano-sized hexagonal platelets, x-ray diffraction studies were firstly used to reveal their crystal structures. Fig. 6.6 (a) and (b) show the XRD profiles of the PLD deposited Co film and the film after reacted with NaOH, respectively. For the Co film, no characteristic peaks can be observed and therefore the crystal structure of the deposited Co film cannot be determined. This could be due to the limitation of the sensitivity of the XRD machine since the deposited Co film is very thin. For the NaOH reacted Co film, the several XRD peaks are located at 19.2°, 32.6°, 38.1° and 51.6° respectively. They match the brucite-like β phase cobalt hydroxide diffraction pattern according to the library JCPDS (file no. 30-443). The peaks are correspondingly related to the (001), (100), (101) and (102) diffraction planes. It indicates that the nano-sized hexagonal platelets could be the cobalt hydroxide

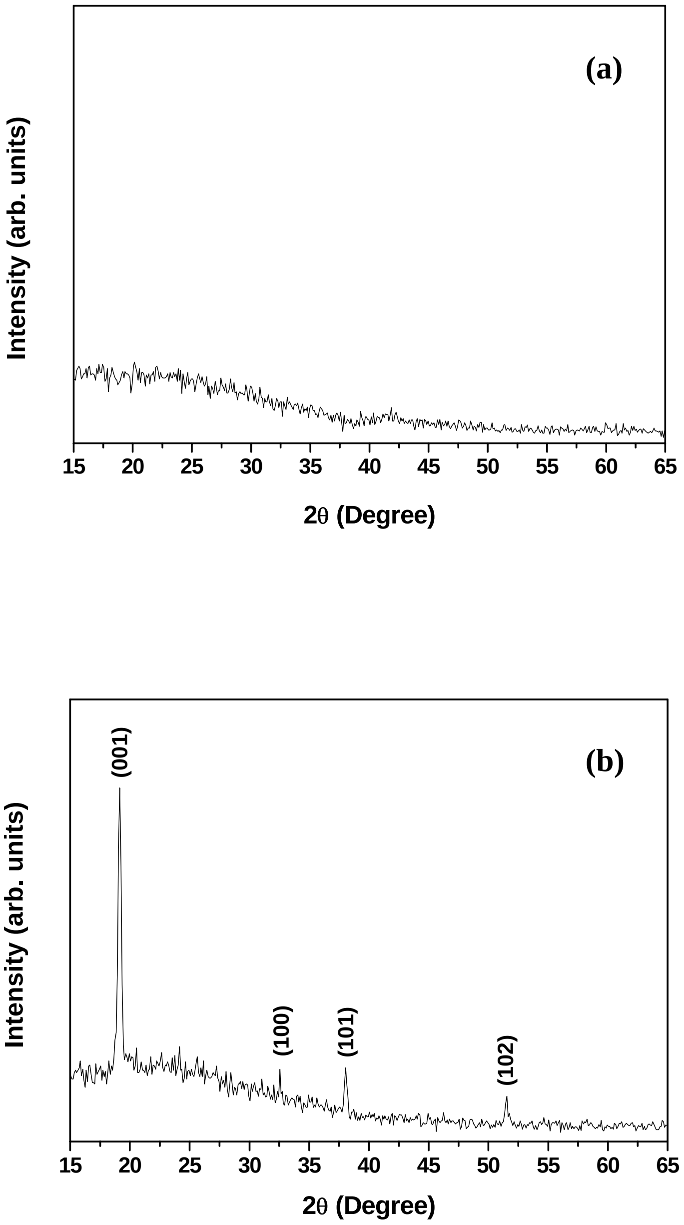

Figure 6.6: **XRD profiles of (a) PLD deposited Co film and (b) PLD deposited Co film reacted with NaOH (0.5M) for 90 min.**

6.4 Infrared Spectroscopy

The samples were further studied by FTIR. Fig. 6.7 shows the FTIR spectra of the PLD deposited Co film after reacted with NaOH, respectively. For the spectra of the NaOH reacted Co film, a sharp characteristic absorption peak is observed at 3631 cm^{-1}, while this absorption peak is not observed in the spectra of the pure Co film. This characteristic absorption peak can be assigned to the stretching mode of the hydroxyl group in the brucite-like phase β-cobalt hydroxide [Zhu 2002]. The peak in the region around 509 cm^{-1} should be contributed to the metal-oxygen vibrations and metal-OH bending vibrations in brucite-like octahedron sheets [Zhu 2002]. Thus, in connection the FTIR measurement with the XRD result, it can be confirmed that the nano-sized hexagonal platelets should be the brucite-like phase β-cobalt hydroxide.

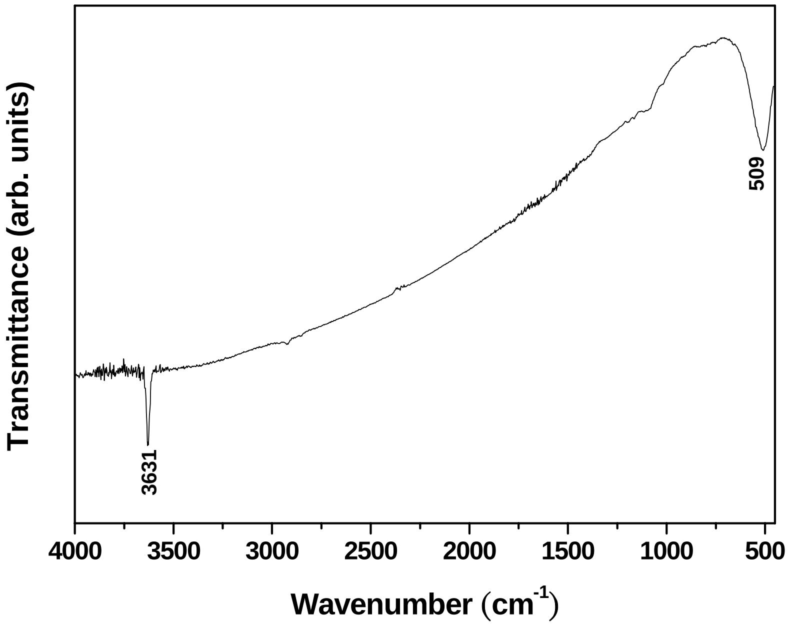

Figure 6.7: **FTIR spectra of PLD deposited Co film reacted with NaOH (0.5M) for 90 min.**

Here are some possible explanations of the formation of the hexagonal cobalt hydroxide. A schematic diagram of the PLD process is shown in Fig. 6.8. During the deposition, the target species will be ablated out from the target due to the high laser fluence. The ablated species will be mostly located at the region near the plasma plume. If a substrate with large size and the deposition time is not long enough to ensure a thick film being deposited, it can be expected that there will be a thickness change of the ablated species throughout the whole film. A compact film or densely packed nanoparticles may be found at the centre of the substrate, while the packing density decrease when moving away from the laser plume region such that the ablated species will be existed as the form of loosely packed nanoparticles.

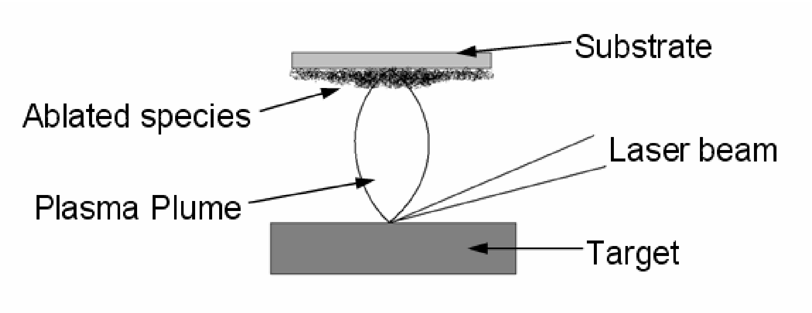

Figure 6.8: Schematic diagram of a PLD-deposited Co film.

In general, bulk cobalt or large cobalt particles react with NaOH mildly. This is verified as shown in Fig. 6.9. The reaction of NaOH with micron-sized Co particles only produces a small change on the surface of the particles while the whole particle shape remains nearly the same. No individual regular hexagonal platelets can be seen. Therefore, Fig. 6.5 (a) and (b) represent a mild reaction between the thick

Co film with NaOH just similar to bulk cobalt surface. The cobalt hydroxide cannot grow into a full platelet. When the Co film is thin enough or the film contains mainly nanosized Co particles, the chemical reaction is promoted due to the nanosize effect, regular hexagonal or half hexagonal cobalt hydroxide can be formed as a result of hydrolysis of Co nanoparticles with NaOH, as shown in Fig. 6.5 (c) and (d). However, more studies are needed in order to further verify the above growing mechanism. Deposition time and reaction time dependence may also need to be studied to gather more supporting experimental results.

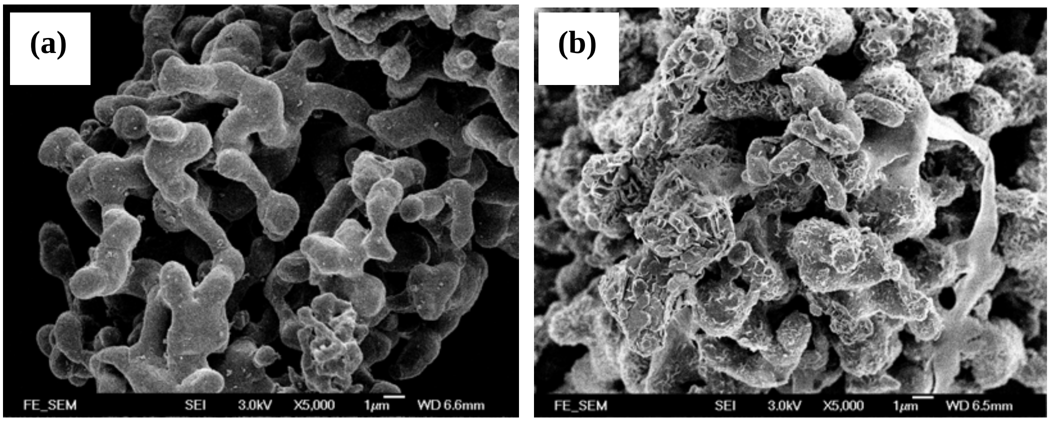

Figure 6.9: **SEM images of micron-sized Co particles (a) without any treatment; (b) reacted with NaOH (0.5M) for 90 min.**

CHAPTER 7

Conclusions

In the present study, a split target arrangement, utilizing cobalt and PTFE as the target materials, has been used to fabricate cobalt-PTFE granular composite thin films on glass substrate by the conventional PLD technique. The composite film samples exhibit a significant MR effect. To the best of our knowledge, this is the first reported study in litertures. Two kinds of samples fabricated with laser wavelength of 355 nm and 1064 nm respectively, reveal a large MR% value of 4% to 5% at room temperature in an applied magnetic field of 10kOe. The samples show a granular structure with nano-sized cobalt particles embedded in a well-connected PTFE network. The results obtained from TEM investigations and magnetic measurements confirm that the nano-sized cobalt particles are superparamagnetic. The electrical transport properties over a wide range of temperature of the film have been studied, which indicate tunneling mechanism is dominated in the electrical conduction of the composite films. The magnetoresistivity of the composite films observed can be interpreted by the spin-dependent tunneling between the cobalt nanoparticles through the PTFE insulating barrier. Temperature dependence of the composite films was also studied. Enhancement of the MR value to 6% was obtained for the measurement at 20 K. Significant shifting of the MR profile observed at low temperature is mainly due to the superparamagnetic effect of the cobalt nanoparticles in the composite films. The temperature dependence of MR can be interpreted by the spin-dependent tunneling of electrons and the superparamagnetic relaxation behavior of the cobalt nanoparticles embedded in the PTFE matrix. Fitting of the experimental data has inferred that higher-order tunneling process and temperature dependence of spin polarization may be also contributed to the observed MR enhancement at low temperature. This study opens the area of using polymeric material, PTFE in our case, as the insulating matrix for fabricating magnetic granular composite with significant MR effect by PLD method. The results indicate that the prepared cobalt-PTFE granular composite can be readily in use for fabricating device like magnetic sensors, or vibration sensors. Further investigations like utilizing ferromagnetic alloy such as CoFe with higher spin polarization combining with other kinds of polymer, in order to looking for higher MR% value, are also of potential interests.

Besides, fabrication of cobalt nanoparticles has been successfully demonstrated by PLAL technique. It was found that the fabricated cobalt nanoparticles have a smaller particle size distribution, with size small enough to become superparamagnetic, by using toluene as the solvent for the laser ablation process. This study provides fundamental results for fabricating ferromagnetic metal-polymer composites using PLAL technique. Suitable kind of polymer, such as PMMA, can be directly dissolved into the toluene solution consist of cobalt nanoparticles. The metal-polymer composites can simply produced on a glass substrate after evaporating the solvent. Further investigations are needed.

Superhydrophobic PTFE thin films were successfully fabricated by pulsed laser deposition technique. A large contact angle of about 170° and low sliding angle was achieved. The surface morphology shows that the surface roughness increased with the number of laser pulses. The water contact angle is related to the surface roughness. This result indicates that nano-scale surface roughness is important in producing superhydrophobic surface, since it will increase the volume of trapping air to achieve a large contact angle and low sliding angle with low contact angle hysteresis. This study provides a convenient one-step dry method to produce a superhydrophobic surface with good self-cleaning properties which can be applied in real life applications.

Apart from the above studies, an innovative method is also presented for fabricating the cobalt hydroxide nanoplatelets at room temperature. Sodium hydroxide (NaOH) solution was used to react with a pure cobalt thin film prepared by pulsed laser deposition. The morphology of the nanoplatelets was studied and the crystal structure was characterized and confirmed. This method provides a simple, relatively fast and clean route to produce nano-sized cobalt hydroxide. The as-prepared cobalt hydroxide platelets are in thin film form which is already grown on the substrate surface with good adhesion. Many practical applications as mentioned before, which need a format of nano-sized cobalt hydroxide on substrate, can be fabricated by this method. Further investigations like the growth mechanisms and other physical properties of the prepared cobalt hydroxide platelets are needed.

References

Amendola, V., Rizzi, G. A., Polizzi, S., Meneghetti, M.,
J. Phys. Chem. B, **109** (2005) 23125

Baibich, M. N., Broto, J. M., Fert, A., Nguyen Van Dau, F., Petroff, F., Etienne, P., Creuzet, G., Friederich, A., Chazelas, J.,
Phys. Rev. Lett., **61** (1988) 2472

Batlle, X., Labarta, A.,
J. Phys. D: Appl. Phys., **35** (2002) R15-R42

Bauer, J., Buss, D. H., Harms, H. J., Glemser, O.,
J. Electrochem. Soc., **137** (1990) 173

Belashchenko, K. D., Tsymbal, E. Y., Schilfgaarde, M., Stewart, D. A., Oleynik, I. I., Jaswal, S. S.,
J. Magn. Magn. Mater., **272-276** (2004) 1954-1955

Besner, S., Kabashin, A. V., Meuniera, M.,
Appl. Phys. Lett., **89** (2006) 233122

Bhowmik, R. N., Ranganathan, R.,
Solid State Communications, **141** (2007) 365-368

Binash, G., Grünberg, P., Saurenbach, F., Zinn, W.,
Phys. Rev. B, **39** (1989) 4828

Bitoh, T., Ohba, K., Takamatsu, M., Shirane, T., Chikazawa, S.,
J. Magn. Magn. Mater., **154** (1996) 59-65

Blanchet, G. B.,
Appl. Phys. Lett., **62** (1993), 479-481

Blanchet, G. B., Fincher, C. R., Jackson, C. L., Shah, S. I., Gardner, K. H.,
Science, **262**, (1993), 719-721

Blanchet, G. B., Shah, S. I.,
Appl. Phys. Lett., **62** (1993), 1026-1028

Cao, L., Xu, F., Liang, Y. Y., Li, H. L.,
Adv. Mater., **16** (2004) 1853

Cassie, B. D., Baxter, S.,
Trans. Faraday Soc. **40** (1944) 546-551

Chen, G. X., Hong, M. H., Lan, B., Wang, Z. B., Lu, Y. F., Chong, T. C.,
Appl. Surf. Sci., **228**, (2004), 169-175

Chen, J. P., Sorensen, C. M., Klabunde, K. J., Hadjipanayis, G. C.,
Phys. Rev. B, **51** (1995) 11527

Chen, P., Xing, D. Y., Du, Y. W., Zhu, J. M., Feng, D.,
Phys. Rev. Lett., **87** (2001) 107202-1

Chrisey, D. B., Hubler, G. K.,
Eds. *Pulsed Laser Deposition of Thin Films*; Wiley: New York, 1994

Coulson, S. R., Woodward, I., Badyal, J. P. S., Brewer, S. A., Willis, C.,
J. Phys. Chem. B, **104** (2000) 8836

Dijkkamp, D., et al.,
Appl. Phys. Lett., **51** (1987) 619-621

Dinamani, M., Kamath, P. V.,
Journal of Applied Electrochemistry, **30** (2000) 1157-1161

Djayaprawira, D. D., Tsunekawa, K., Nagai, M., Maehara, H., Yamagata, S., Watanabe, N., Yuasa, S., Suzuki, Y., Ando, K.,
Appl. Phys. Lett., **86** (2005) 092502

Dolgaev, S. I., Simakin, A. V., Voronov, V. V., Shafeev, G. A., Bozon-Verduraz, F.,
Appl. Surf. Sci., **186**, (2002), 546-551

Dureuil, V., Ricolleau, C., Gandais, M., Grigis, C., Lacharme, J. P., Naudon, A.,
Journal of Crystal Growth, **233** (2001) 737-748

Erbil, H. Y., Demirel, A. L., Avci, Y., Mert, O.,
Science, **299** (2003) 1377-1380

Fabbro, R., Fournier, J., Ballard, P., Devaux, D., Virmont, J.,
J. Appl. Phys., **68** (1990) 775

Faupel, J., Fuhse, C., Meschede, A., Herweg, C., Krebs, H. U., Vitta, S.,
Appl. Phys. A, **79** (2004) 1233-1235

Fox, H. W., Zisman, W. A.,
J. Colloid Sci., **5** (1950) 514-531

Fujimori, H., Mitani, S., Ohnuma, S.,
Mater. Sci. Eng. B - Sol. Stat. Mater. Adv. Technol., **31** (1995) 219

Furubayashi, T., Nakatani, I.,
J. Appl. Phys., **79** (1996) 6258

Gittleman, J.L., Goldstein, Y., Bozowski, S.,
Phys. Rev. B, **5** (1972) 3609

Gong, W., Li, H., Zhao, Z., Chen, J.,
J. Appl. Phys., **69** (1991) 5119

Gubin, S. P., Yurkov, G. Y., Korobov, M. S., Koksharov, Y. A., Kozinkin, A. V., Pirog, I. V., Zubkov, S. V., Kitaev, V. V., Sarichev, D. A., Bouznik, V. M., Tsvetnikov, A. K.,
Acta Materialia, **53** (2005) 1407-1413

Guo, Z. G., Fang, J., Hao, J. C., Liang, Y. M., Liu, W. M.,
ChemPhysChem, **7** (2006) 1674-1677

Han, X.F., Oogane, M., Kubota, H., Ando, Y., Miyazaki, T.,
Appl. Phys. Lett., **77** (2000) 283

Hansen, S. G., Robitaille, T. E.,
Appl. Phys. Lett., **52** (1988) 81-83

Hansen, S. G., Robitaille, T. E.,
J. Appl. Phys., **64** (1988) 2122-2129

Happy, Mohanty, S. R., Lee, P., Tan, T. L., Springham, S. V., Patran, A., Ramanujan, R. V., Rawat, R. S.,
Appl. Surf. Sci., **252** (2006) 2806-2816

Hattink, B. J., Garcia del Muro, M., Konstantinovic, Z., Batlle, X., Labarta, A., Varela, M.,
Phys. Rev. B, **73** (2006) 045418

Helman, J. S., Abeles, B.,
Phys. Rev. Lett. **37** (1976) 1429

Holland, L., Biederman, H., Ojha, S. M.,
Thin Solid Films, **35** (1976) L19-L21

Honda, S., Okada, T., Nawate, M.,
Phys. Rev. B, **56** (1997) 14566

Hou, Y., Kondoh, H., Shimojo, M., Kogure, T., Ohta, T.,
J. Phys. Chem. B, **109** (2005) 19094-19098

Inoue, J., Maekawa, S.,
Phys. Rev. B, **53** (1996) R11927

Jiang, W. B., Norton, M. G., Tsung, L., Dickinson, J. T.,
J. Mater. Res., **10** (1995) 1038-1043

Johnson, R.E. Jr., Dettre, R.H.,
Adv. Chem. Ser., **43** (1963) 112-135

Jozer, N., Chen, D. G., Buyuklimanli, T.,
Solar Energy Materials and Solar Cells, **52** (1998) 223-230

Julliere, M.,
Phys. Lett. A, **54** (1975) 225

Kamath, P. V., Therese, G. H. A., Gopalakrishnan, J.,
Journal of solid state chemistry, **128** (1997) 38-41

Kawaguchi, K., Jaworskib, J., Ishikawaa, Y., Sasakia, T., Koshizakia, N.,
Journal of Magnetism and Magnetic Materials, **310** (2007) 2369-2371

Kobayashi, N., Ohnuma, S., Masumoto, T., Fujimori, H.,
J. Appl. Phys., **90** (2001) 4159

Kruis, F. E., Fissan, H., Peled, A.,
J. Aerosol Sci., **29** (1998) 511-535

Kurmoo, M.,
Chem. Mater., **11** (1999) 3370-3378

Lau, K. K. S., Bico, J., Teo, K. B. K., Chhowalla, M., Amaratunga, G. A. J.,
Milne, W. I., McKinley, G. H., Gleason, K. K.,
Nano Lett., **3** (2003) 1701

Li, Q., Sasaki, T., Koshizaki, N.,
Appl. Phys. A, **69** (1999) 115-118

Li, S. T., Arenholz, E., Heitz, J., Bauerle, D.,
Appl. Surf. Sci., **125** (1998) 17-22

Li, Z., de Groot, C., Moodera, J.S.,
Appl. Phys. Lett., **77** (2000) 3630

Liang, C., Sasaki, T., Shimizu, Y., Koshizaki, N.,
Chemical Physics Letters, **389** (2004) 58-63

Liu, Z., Ma, R., Osada, M., Takada, K., Sasaki, T.,
J. Am. Chem. Soc., **127** (2005) 13869-13874

Lyu, P., Xing, D. Y., Dong, J.,
Phys. Rev. B, **60** (1999) 4235

Maceira, V. S., Duarte, M. A. C., Duman, E., Farle, M.,
J. Magn. Magn. Mater., **299** (2006) 467-471

Mafune, F., Kohno, J., Takeda, Y., Kondow, T., Sawabe, H.,
J. Phys. Chem. B, **104** (2000) 9111-9117

Mafune, F., Kohno, J., Takeda, Y., Kondow, T., Sawabe, H.,
J. Phys. Chem. B, **105** (2001) 5114-5120

Maiman, T. H.,
Nature, **187** (1960) 493

Makhlouf, S. A.,
J. Magn. Magn. Mater., **246** (2002) 184-190

McHenry, M. E., Majetich, S. A., Artman, J. O., DeGraef, M., Staley, S. W.,
Phys. Rev. B, **49** (1994) 11358

Meservey, R., Tedrow, P. M.,
Phys. Rep., **238** (1994) 173

Milner, A., Gerber, A., Groisman, B., Karpovsky, M., Gladkikh, A.,
Phys. Rev. Lett., **76** (1996) 475

Mitani, S., Fujimori, H., Ohnuma, S.,
J. Magn. Magn. Mater., **165** (1997) 141-148

Mitani, S., Takanashi, K., Yakushiji, K., Chiba, J., Fujimori, H.,
Mater. Sci. Eng. B, **84** (2001) 120–125

Mitani, S., Takahashi, S., Takanashi, K., Yakushiji, K., Maekawa, S., Fujimori, H.,
Phys. Rev. Lett., **81** (1998) 2799

Miyazaki, T., Tezuka, N.,
J. Magn. Magn. Mater., **139** (1995) L231

Moodera, J.S., Mathon, G.,
J. Magn. Magn. Mater., **200** (1999) 248-273

Mott, N. F.,
Proc. Roy. Soc.London Ser. A, **153** (1936) 699

Nakajima, A., Hashimoto, K., Watanabe, T.,
Monatshefte fur Chemie/Chemical Monthly, **132** (2001) 31-41

Norton, M. G.; Jiang, W. B.; Dickinson, J. T.; Hipps, K. W.,
Appl. Surf. Sci., **96-8** (1996) 617-620

Ohnuma, M., Hono, K., Abe, E., Onodera, H., Mitani, S., Fujimori, H.,
J. Appl. Phys., **82** (1997) 5646

Park, I. W., Yoon, M., Kim, Y. M., Kim, Y., Yoon, H., Song, H. J.,
Volkov, V., Avilov, A., Park, Y. J.,
Solid State Communications, **44** (2003) 385-389

Park, J., Zhu, R. S., Lin, M. C.,
Journal of chemical physics, **117** (2002) 3224

Patil, P. P., Phase, D. M., Kulkarni, S. A., Ghaisas, S. V., Kulkarni, S. K.,
Kanrtkar, S. M., Ogale, S. B., Bhide, V. G.,
Phys. Rev. Lett., **58** (1987) 238

Pelecky, D. L. L., Zhang, X. Q., Rieke, R. D.,
J. Appl. Phys., **79** (1996) 5312

Respaud, M., Broto, J. M., Rakoto, H., Fert, A. R., Thomas, L., Barbara, B.,
Verelst, M., Snoeck, E., Lecante, P., Mosset, A., Osuna, J., Ould Ely, T., Amiens, C.,
Chaudret, B.,
Phys. Rev. B, **57** (1998) 2925

Roder, J., Krebs, H. U.,
Appl. Phys. A, **85** (2006) 15-20

Rottlander, P., Hehn, M., Lenoble, O., Schuhl, A.,
Appl. Phys. Lett., **78** (2001) 3274

Sasaki, T., Terauchi, S., Koshizaki, N., Umehara, H.,
Appl. Surf. Sci., **127-129 (**1998) 398-402

Schad, R., Potter, C. D., Beliën, P., Verbanck, G., Moshchalkov, V. V.,
Bruynseraede, Y.,
Appl. Phys. Lett., **64** (1994) 3500

Schurmann, U., Takele, H., Zaporojtchenko, V., Faupel, F.,
Thin Solid Films, **515** (2006) 801-804

Shang, C. H., Nowak, J., Jansen, R., Moodera, J. S.,
Phys. Rev. B, **58** (1998) R2917

Sharma, M., Nickel, J.H., Anthony, T.C., Wang, S.X.,
Appl. Phys. Lett., **77** (2000) 2219

Sheng, J., Zhen, Y. L.,
J. Appl. Phys., **92** (2002) 5281

Sheng, P., Abeles, B., Arie, Y.,
Phys. Rev. Lett., **31** (1973) 44

Simakin, A. V., Voronov, V. V., Shafeev, G. A., Brayner, R., Bozon-Verduraz, F.,
Chemical Physics Letters, **348** (2001) 182-186

Slonczewski, J. C.,
Phys. Rev. B, **39** (1989) 6995

Smausz, T., Hopp, B., Kresz, N.,
J. Phys. D: Appl. Phys., **35** (2002) 1859-1863

Smith, H. M., Turner, A. F.,
Appl. Opt., **4** (1965) 147-148

Soeno, T., Inokuchi, K., Shiratori, S.,
Appl. Surf. Sci., **237** (2004) 543-547

Soulen, Jr. R. J., Byers, J. M., Osofsky, M. S., Nadgorny, B., Ambrose, T.,
Cheng, S. F., Broussard, P. R., Tanaka, C. T., Nowak, J., Moodera, J. S.,
Barry, A., Coey, J. M. D.,
Science, **282** (1998) 85

Sousa, R. C., Sun, J. J., Soares, V., Freitas, P. P., Kling, A., da Silva, M. F., Soares, J. C.,
Appl. Phys. Lett., **73** (1998) 3288

Stearns, M. B.,
J. Magn. Magn. Mater., **5** (1977) 167-171

Sun, Z., Liu, L., Jia, D. Z., Pan, W.,
Sensors and Actuators B, **125** (2007) 144-148

Tang, H., Li, Y., Zheng, C., Ye, J., Hou, X., Lv, Y.,
Talanta, **72** (2007) 1593-1597

Tang, Y., Xu, X., Fang, J., Liang, Y., Ji, H. F.,
IEEE Transactions on Nanotechnology, **5** (2006) 415

Tedrow, P. M., Meservey, R.,
Phys. Rev. B, **7** (1973) 318

Toyota, K., Tanaka, T., Nishiwaki, S., Nakashima, S., Okada, T.,
Journal of Photochemistry and Photobiology A: Chemistry, **141** (2001) 9-16

Tsuji, T., Hamagami, T., Kawamura, T., Yamaki, J., Tsuji, M.,
Appl. Surf. Sci., **243** (2005) 214-219

Tsymbal, E. Y., Burlakov, V. M., Oleinik, I. I.,
Phys. Rev. B, **66** (2002) 073201

Tsymbal, E. Y., Oleinik, I. I., Pettifor, D. G.,
J. Appl. Phys., **87** (2000) 5230

Tsymbal, E. Y., Pettifor, D. G.,
J. Magn. Magn. Mater., **198-199** (1999) 146-148

Tsymbal, E. Y., Sokolov, A., Sabirianov, I. F., Doudin, B.,
Phys. Rev. Lett., **90** (2003) 186602

Ueno, Y., Fujii, T., Kannari, F.,
Appl. Phys. Lett., **65** (1994) 1370-1372

Vaseashta, A., Malinovska, D. D.,
Science and Technology of Advanced Materials, **6** (2005) 312-318

Vedyayev, A., Bagrets, D., Bagrets, A., Dieny, B.,
Phys. Rev. B, **63** (2001) 064429

Vrejoiu, I., Pedarnig, J. D., Bauerle, D.,
Appl. Phys. Lett., **83** (2003) 2130

Wang, D., Nordman, C., Daughton, J. M., Qian, Z., Fink, J.,
IEEE Trans. Magn., **40** (2004) 2269

Wang, J., Freitas, P. P., Snoeck, E.,
Appl. Phys. Lett., **79** (2001) 4553

Wang, J., Freitas, P. P., Wei, P., Barradas, N. P., Soares, J. C.,
J. Appl. Phys., **89** (2001) 6868

Wenzel, R. N.,
Industrial & Engineering Chemistry, **28** (1936) 988-994

Wilcoxon, J. P., Martin, J. E., Parsapour, F., Wiedenman, B., Kelley, D. F.,
Journal of chemical physics, **108** (1998) 9137

Womack, M., Vendan, M., Molian, P.,
Appl. Surf. Sci., **221** (2004) 99-109

Wu, Y., Saito, N., Nae, F. A., Inoue, Y., Takai, O.,
Surface Science, **600** (2006) 3710-3714

Wunnicke, O., Papanikolaou, N., Zeller, R., Dederichs, P. H., Drchal, V., Kudrnovsky, J.,
Phys. Rev. B, **65** (2002) 064425

Yakushiji, K., Matsuura, M., Mitani, S., Takanashi, K., Fujimori, H.,
J. Magn. Magn. Mater., **303** (2006) e355-e358

Yang, G. W.,
Progress in Materials Science, **52** (2007) 648-698

Yang, G. W., Wang, J. B., Liu, Q. X.,
J. Phys.: Condens. Matter., **10** (1998) 7923

Yang, L. X., Zhu, Y. J., Li, L., Zhang, L., Tong, H., Wang, W. W., Cheng, G. F., Zhu, J. F.,
Eur. J. Inorg. Chem., (2006) 4787-4792

Yoshimitsu, Z., Nakajima, A., Watanabe, T., Hashimoto, K.,
Langmuir, **18** (2002) 5818-5822

Zhang, L., Dutta, A. K., Jarero, G., Stroeve, P.,
Langmuir, **16** (2000) 7095-7100

Zhang, Y. D., Budnick, J. I., Hines, W. A., Chien, C. L., Xiao, J. Q.,
Appl. Phys. Lett., **72** (1998) 2053

Zhu, T., Wang, Y. J.,
Phys. Rev. B, **60** (1999) 11918

Zhu, Y., Li, H., Koltypin, Y., Gedanken, A.,
J. Mater. Chem., **12** (2002) 729-733